UNIVERSITY
OF TRENTO - Italy
Department of Materials Engineering
and Industrial Technologies

Doctoral School in Materials Engineering – XXII cycle

Modification of Anode Microstructure to Improve Redox Stability of Solid Oxide Fuel Cells (SOFCs)

Anna Rita Contino

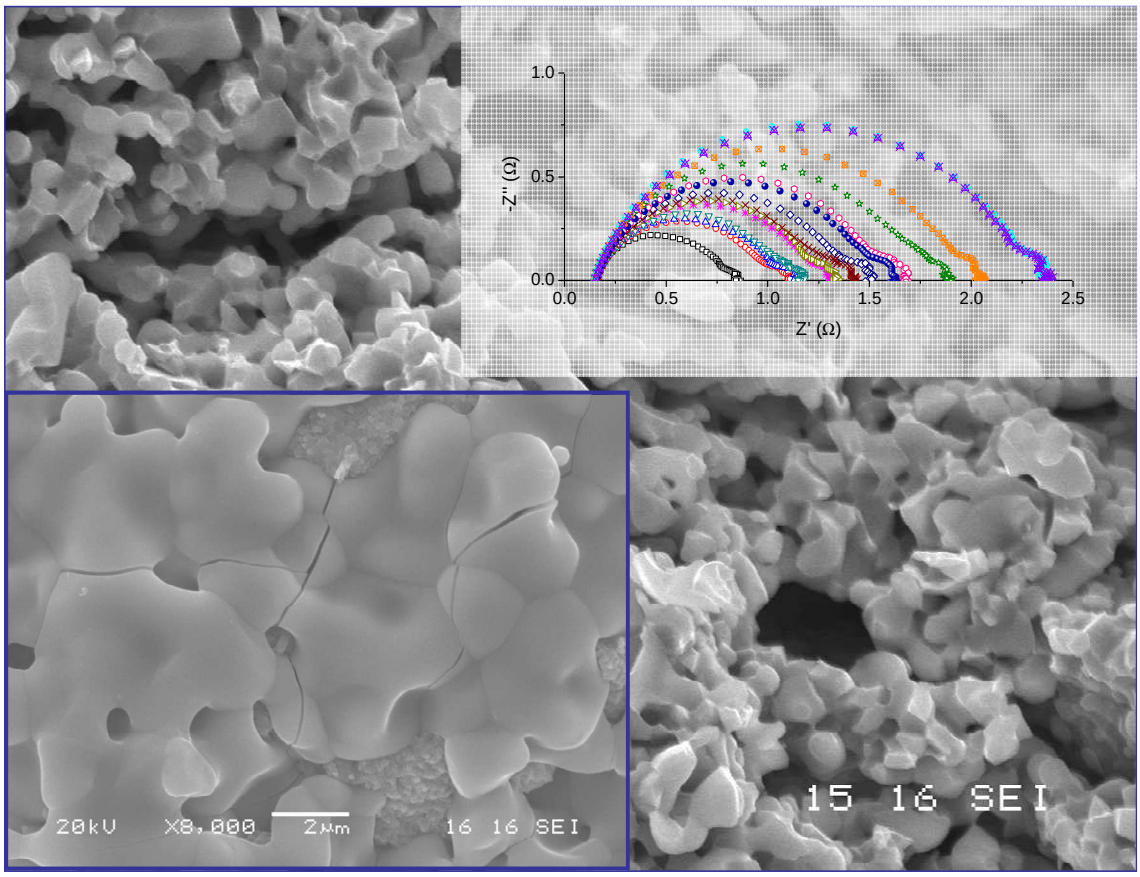

April 2010

Modification of Anode Microstructure to Improve Redox Stability of Solid Oxide Fuel Cells (SOFCs)

by

Anna Rita Contino

Tutor:
Prof. Ing. Vincenzo M. Sglavo

Doctoral committee:
Prof. Emmanuel Garnier, Université de Poitiers
Prof. Gernot Kostorz, Eidgenössische Technische Hochschule Zürich
Prof. Paolo Scardi, Università degli Studi di Trento

Date of dissertation: 30th April 2010

Ai miei genitori e a mio fratello

Acknowledgements

I would like to thank Professor Vincenzo M. Sglavo for the opportunity to come to Trento and to collaborate with him. The possibility to work on this thesis allowed me to enhance my professional competences. I would also greatly thank him for the support and for trusting me during these years.

The research work presented in this thesis was performed in collaboration with SOFCpower Srl Company: it is a pleasure for me to thank Dr. Massimo Bertoldi and Dr. Stefano Modena for their useful suggestions and interesting discussions and for the opportunity to perform some experimental tests and to use the company's facilities.

It is a pleasure for me to thanks all the people, professors, technicians, colleagues and friends I met and I worked with during these years. I would like to mention some of them: Aylin, Amaia, Francesca, Lorenzo, Palloma, Valeria, Vincenzo, Gabriele, Sergio, Marzio, Andrè, Tati, Aravind, Emanuela, Pradeep, Claudia, Ketner, Michele, Ricardo and Ernesto for their support and for the agreeable atmosphere during the long working days.
A particular thank to Professor Roberto Dal Maschio for his suggestions and support. I am grateful to Dario and Marco who shared their knowledge on SOFC and spent long time working together.

I would like to expresses my gratitude to Professor Riccardo Ceccato for the useful hints in BET analyses, Dr. Cinzia Menapace for the help during thermogravimetric analyses performed in the lab of Metallurgia in Trento and M.Sc. Antonin Faes for quantitative images analysis on *Alfa* cells performed at CIME-EPFL.

TABLE OF THE CONTENTS

INTRODUCTION

In the last decade the increase in energy demand, the awareness of limited availability of fossil fuels and the need to reduce green house gases emission impelled governments and research institutions to focus on the study of renewable energy sources such as solar, wind and biomass derived energy and on the increase in the energy production devices efficiency.

Within such scenario a relevant contribution is given by fuel cells technologies as advanced power generation system. Fuel cells are high efficiency devices and comply with the request of environmental friendly source of energy. They convert directly fuel energy into power and heat by electrochemical reactions without the need for combustion as intermediate step. The possibility to use Hydrogen makes fuel cells virtually zero-emission devices being water the only reaction product; nevertheless, also the use of hydrocarbons as fuel reduces considerable CO_2 emissions.

Among the different systems, solid oxide fuel cells (SOFCs) operate at high temperatures (650-1000°C) and allow to achieve the highest electrical efficiency, from 45 to 60% for common fuels, values not attainable by traditional electrical power generation methods, and up to 70% in combination with a gas turbine for Hybrid Power System generation, with an overall electrical and thermal efficiency higher than 90%.

Moreover, such technology presents many advantages such as the possibility to be fed with different fuels, the absence of moving parts, modularity and limited emissions. These characteristics make SOFC suitable for application in the distributed generation market.

Despite all the mentioned advantages, SOFCs show problems that make these devices not suitable for the production on industrial scale yet. In particular they present low reliability and are not competitive with traditional powers sources.

SOFCs are constituted by single cells (consisting of an anode and a cathode separated by a solid electrolyte) that are collected together in a stack by interconnects in order to obtain the required power. This means that a stack is a multilayer assembly of materials with different thermal, mechanical and chemical properties that need to fulfil many prerequisites for their own function. Moreover, some of these properties must match for other connected

components; for instance they have to show similar thermal expansion coefficients, to be stable at high temperatures and during thermal transients.

Due to the high working temperature, stack components are necessarily subjected to degradation phenomena, which reduce their long term reliability. Among them, poisoning of cathode by Chromium evaporation from metallic interconnects, chemical interactions between glass–ceramic sealants and ferritic steel interconnects, anode poisoning caused by carbon or sulphur deposition, reduction of electrical conductivity are worthy of mention. Furthermore, various cycling conditions such as thermal cycle, redox cycle, and load cycle affect stability of SOFCs. All these degradation phenomena must be minimized in order to increase SOFC reliability. All these issues are object of intense research.

The research work of the present thesis has been focused on the increase of redox stability of anode supported cells, which is considered one of the key point to improve stack reliability.

The state of the art materials for the anode is Ni/YSZ cermet due to its high performance. Nevertheless, this cermet is prone to severe degradation upon redox cycling.

Due to the high operating temperatures, Nickel particles tend to coalesce and coarsen. Fuel supply interruptions, over-potentials and leakages can cause the re-oxidation of Ni to NiO with a consequent volumetric expansion that can generate internal stresses and lead to cracks formation within the YSZ network and the electrolyte resulting in cell failure. Different approaches can be taken in account in order to minimize redox instability.

In order to study redox phenomena and produce redox stable cells many aspects related to the modification of anodic microstructure were analyzed. Among these, one of the most promising method is to modify the anode microstructure by increasing its porosity.

The present thesis is divided in two parts. In the first section the theoretical background of fuel cells, specifically SOFCs, is reported. A particular attention is dedicated to describe redox phenomenon and the state of the art of the research in this field.

The second experimental part concerns with the production of anodes with improved microstructure. The modification of microstructure was realized by using different powders

and by adding different pore formers and doping elements. A detailed study of the effects on redox stability of the microstructure modifications induced by the addition of each of the aforesaid substances is described.

Part of the experiments of this work, in particular electrochemical characterizations, have been carried out at SOFCpower Srl laboratories in Mezzolombardo (TN), an Italian leading company manufacturing cells and systems based on a proprietary SOFC technology (www.sofcpower.com).

SECTION 1

CHAPTER 1

STATE OF THE ART

1.1 FUEL CELLS

Fuel cells are electrochemical devices that directly convert chemical energy into electrical energy and heat at high efficiency. As for the working principle, fuel cells can be assimilated to a battery; while the latter needs to stop for recharge, fuel cells operate continuously since a fuel and an oxidant are constantly fed.

This technology is well known, thanks to the initial contributions of many scientists such as Grove and Nernst in the first half of nineteenth century [1, 2]. The lack of adequate materials and investigation techniques along with high costs limited the use of fuel cells as power generation devices. Only in the last decades, the increase in the energy demand and of the costs of the traditional fuels, the need of alternative and renewable energy sources and the developments in material science have brought a new impulse to the research into the fuel cells field.

The most valuable feature of fuel cells is the possibility to work with high conversion efficiencies. Indeed, in a traditional power cycle, i.e. steam power plants and internal combustion engines, electrical energy is obtained by transforming chemical energy into heat which is subsequently converted into power. The irreversibility of this multistep process limits the electrical efficiency as for the Carnot's principle. Moreover, the presence of mechanical rotating components further decreases the efficiency of traditional systems and increases maintenance costs.

Fuel cells are not subjected to such limitations because electricity is produced in a single step through an electrochemical reaction [1].

Electrical efficiency of fuel cells ranges from 40 to 60% and is independent from plant size while only large power plants can achieve similar values. This makes fuel cells suitable also for micro-generation plants and distributed systems. Another advantage of fuel cells is their combined heat production, which raise the overall efficiency at about 90%. Moreover, the electrochemical production of energy reduces the amount of the undesired

and polluting by-products of fuels combustion such as fine particulates and nitrogen oxides, making fuel cells a viable environmental friendly technology [3].

The fuel cells power systems contain different components that, in the order, are [4]:

1. Unit cells where the electrochemical reaction take place. A unit cell is constituted by two electrodes: anode and cathode separated by the electrolyte.
2. Stacks, where unit cells are modularly combined by electrical connections in order to achieve the voltage and power output level necessary for the applications.
3. Balance of plant (BOP) that are auxiliary components including a fuel processor, if needed, thermal management, and electric power conditioning among other additional and interface functions (pumps, blowers, control valves, pressure regulators, cooling system, are some example).

Different types of fuel cells have been developed so far [5-7], each presenting specific advantages and drawbacks for different applications.

Fuel cells can be classified considering the type of used electrolyte (that determines the kind of chemical reactions that occur within the cell, the operative temperature, the kind of catalyst, the necessary fuel, and other attributes), or considering the fuel that they can process or in term of the working temperature range. For all of them the oxidant is air or pure oxygen.

A summary of fuel cells types, including the main reactions and the typical operating temperatures, is reported in figure 1.1.

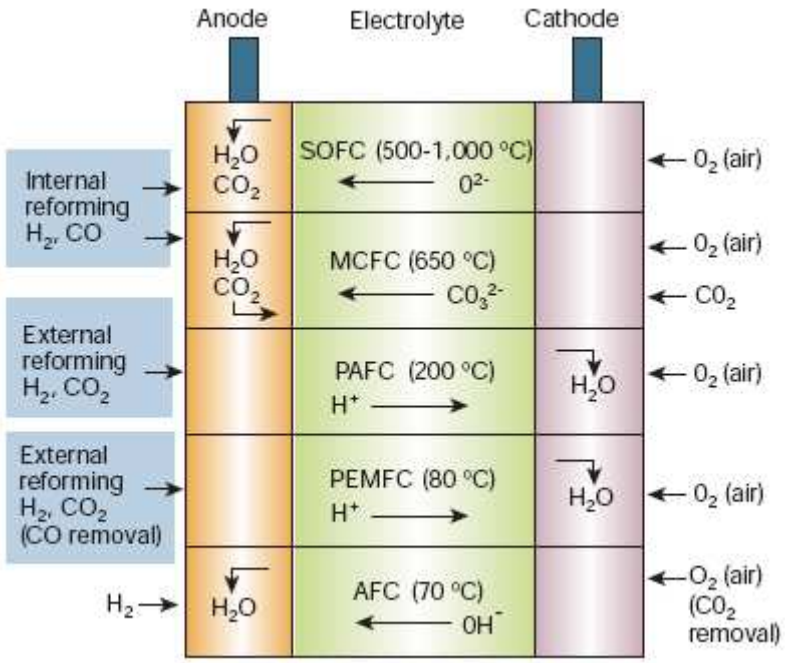

Fig. 1.1: Summary of fuel cells types [6].

Low temperature fuel cells use only H_2 and are generally classified as:

- ✓ Alkaline fuel cells (AFC): the electrolyte is a solution of potassium hydroxide in water. They can use a variety of non-precious metals such as catalyst at the anode and cathode. High-temperature AFCs work at temperatures between 100°C and 250°C. Nevertheless, newer AFC designs operate at lower temperatures of roughly 23°C to 70°C. They have an efficiency of 50-60%.
- ✓ Proton Exchange Membrane Fuel Cells (PEMFC or PEFC): the electrolyte is a solid polymer where protons are the mobile ions, and a Platinum catalyst is contained in porous carbon electrodes. The range of operative temperature is 80-100°C and the efficiency is 40-45%. Among the PEFCs, Direct Methanol Fuel Cells (DMFC) operate at the same temperature but they use MeOH as fuel and possess an efficiency of 25-

30%. A third class of PEFC that works at high temperatures is HT-PEFC which can use H_2 or CO as fuels at 120-180°C and reach an efficiency up to 40-50%.

- ✓ Phosphoric Acid Fuel Cells (PAFC): this kind of fuel cell uses liquid phosphoric acid for the electrolyte; the acid is contained in a Teflon-bonded silicon carbide matrix, and the electrodes are made of porous carbon containing a Platinum catalyst. The operative temperature is about 200°C with an efficiency of 40-45%.

The high temperature fuel cells can operate with different fuels other than H_2 such as CO, natural gas, and hydrocarbon fuels:

- ✓ Solid Oxide Fuel Cells (SOFC): the electrolyte is a dense solid ceramic material usually yttria stabilized zirconia (YSZ); typically, the anode is a Ni-ZrO_2 cermet and the cathode is Sr-doped $LaMnO_3$. The operating temperature ranges between 700 and 1000°C, whereas the low temperature LT-SOFCs work at 500-650°C. SOFCs have an efficiency of 50-60%.
- ✓ Molten Carbonate Fuel Cells (MCFC): the electrolyte is usually a combination of alkali carbonates (lithium, sodium and potassium carbonate), which is retained in a chemically inert porous ceramic matrix of $LiAlO_2$. At the operating temperatures (600-700°C) highly conductive molten salt is formed by alkali carbonates and the ionic conduction is supplied by carbonate ions (CO_3^{2-}). Ni and nickel oxide are used as anode and cathode electrodes, respectively. The efficiency of the MCFCs is around 50-55% [8, 9].

By a comparison of the different kind of fuel cells, from the high to the low temperature fuel cells, one can observe a decrease of the efficiency, higher sensitivity to contaminant elements and increased complexity of fuel processing [6].

High efficiency and the possibility to use different fuels are some of the advantages offered by SOFC that make them more interesting than other types of FC. The solid electrolyte is not corrosive (such as MCFC) and avoids electrolyte movement or flooding through the electrodes. Moreover, it can be considered that due to the high operating temperature, the kinetics of the cell are relatively fast and no precious metals (such as Platinum used in low temperature fuel cells) are needed to accelerate chemical reactions.

Therefore, carbon monoxide does not represent a harmful substance for the anode, and it can be directly fed as fuel. The materials used in SOFCs are not too expensive. Thin-electrolyte planar SOFC unit cells have been demonstrated to be capable of power densities close to those achieved by PEFC. Moreover, high-temperature MCFCs and SOFCs are ideal candidates for fuel cell/gas turbine hybrid systems thanks to the possibility to use the discarded thermal energy and the energy from the combustion of residual fuel to drive gas turbine (GT).

Currently, it is possible to observe a rapidly growing trend in the application of fuel cells in different industrial fields. The applications of fuel cells can generally be divided into portable, transport and stationary purposes, including combined heat and power systems (CHP). However, the viable application varies according to the type of used fuel cells:

- AFCs were the first type of FCs widely used in U.S. space program to produce electrical energy and water on-board spacecrafts, e.g. Apollo or Shuttle;
- PEMFC are found in vehicles and portable applications, and for power CHP systems;
- DMFC are suitable for low power portable electronic systems;
- PAFC are used for a large number of 200 kW CHP systems;
- MCFC are suitable for medium to large scale CHP systems, up to MW capacity; they are used in industrial and military applications;
- SOFC are appropriate for all size of CHP systems, 2 kW to multi MW, automotive industries, and portable devices; they can be used for hybrid/GT cycles.

Apart from the previously mentioned high efficiency, fuel cells provide many other advantages over traditional energy conversion systems: modularity, fuel adaptability, and very low levels of NO_x and SO_x emissions. Quiet, vibration free operation of FC also eliminates noise usually associated with conventional power generation systems.

Despite the attractive system efficiency and environmental benefits related to fuel cell technology, some difficulties have been encountered to develop the laboratory prototypes into commercial products. These issues have often been associated with the

requirement of appropriate materials or manufacturing routes that would permit the cost of electricity per kWh to compete with the existing technology.

It is possible to make a few general consideration about the material requirement for fuel cells. The combined area specific resistivity (ASR) of the cell components (electrolyte, anode and cathode) should be below 0.5 Ωcm^2 (ideally approaching 0.1 Ωcm^2) to ensure high power densities, with targets of 1 $kWdm^{-3}$ and 1 $kWkg^{-1}$, often mentioned for transport applications [6]. Moreover, if the fuel cells have high power density, the amount of material per kW is minimized and, as a consequence, there is a reduction of the costs. Other limitations related to material choice arise from reliability and durability issues. In the case of stationary applications a degradation rate must extend over a period of at least 40,000 h (5 years).

1.2 SOLID OXIDE FUEL CELL (SOFC)

The topic of the present thesis is the study of instability to the redox cycles for anode supported solid oxide fuel cells; therefore, in this section SOFC devices will be described in detail.

SOFCs operate at temperatures ranging from 550°C to 1000°C allowing to reach high electrical efficiencies (up to 60%); moreover, the possibility to feed them with different fuels, as Hydrogen, carbon monoxide and hydrocarbons, and their ease of production are some advantages that explain the high interest of researchers and industries on this technology with respect to the other types of fuel cells. On the other hand, it has to be mentioned that, the high operating temperatures are critical for the long time reliability of SOFCs, as materials degradation rate increases.

There are different types of SOFC design, basically tubular and planar, which differ in the single cells design and arrangement, interconnect materials and gas flow. Each of these two designs has a number of interesting variants: for example, planar SOFC may be in the form of circular disc fed with fuel from the central axis, or it may be in the form of square plate fed from the sides.

Tubular cells can be distinguished in two broad categories: cells with a large diameter, >15 mm, and cells with a diameter lower than 5 mm, usually named microtubular cells [10].

The first tubular cells were produced by Siemens Westinghouse Power Corporation.

In the most common configuration, tubular cell electrodes and electrolyte are deposited as thin layer around the external surface of a porous cylindrical tube having the function of support and of air distributor for the cathode [11].

In the first cell the tube was made of calcia-stabilized zirconia with the walls as thin as possible considering its support function.

In the most recent production the porous supported tube has been replaced by a doped $LaMnO_3$ tube having the function of cathode (air-electrode supported cell) onto which the other cell components are deposited.

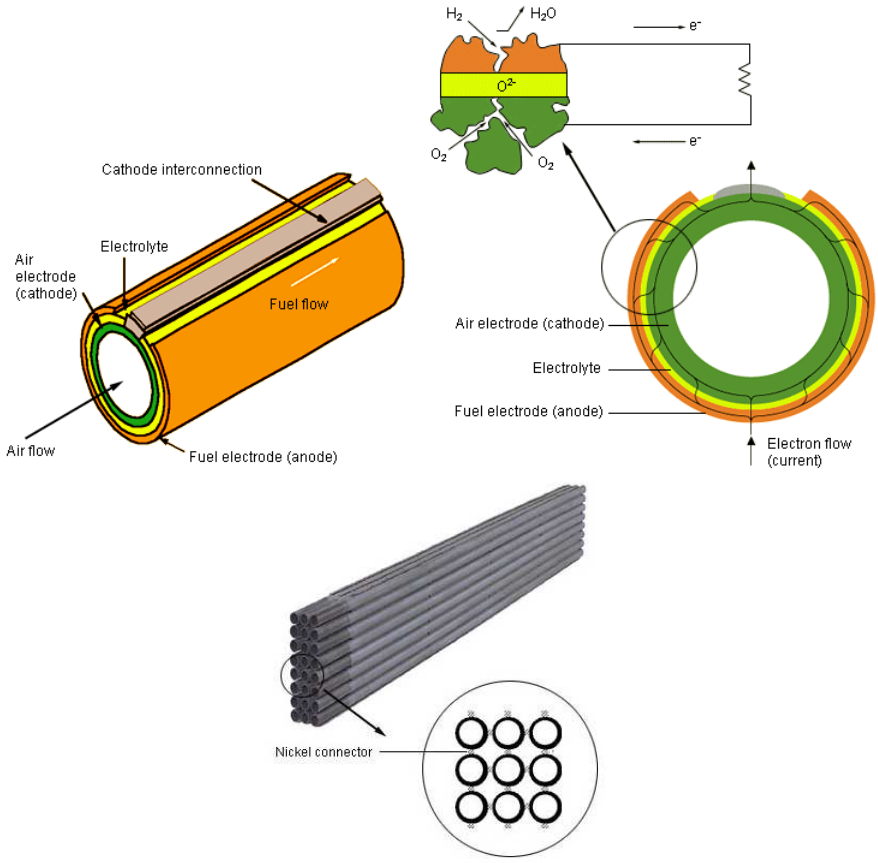

Fig. 1.2: Tubular design SOFC by Siemens Westinghouse Power Corporation [12].

The result of this substitution was a decrease of the inherent impedance to air flow toward the cathode. Siemens Westinghouse Power Corporation tubular SOFC design is reported in figure 1.2; the cells are nominally 2.2 cm in diameter and 150 cm in active length with one closed end. Air is supplied to the cell interior using an air delivery tube and fuel is delivered to the cell exterior [12, 13].

Power produced is proportional to the active surface area of the cells. Their operating temperature is about 1000°C; at such temperature and under atmospheric pressure, single tubular SOFC generates power of up to 210 W DC (direct current).
Each cell attains (at open circuit) a potential of about 1 V; therefore, in order to reach a voltage suitable for applications, cells are connected in series. The materials commonly used for the components are YSZ for the electrolyte and Nickel/zirconia cermet, bonded to the electrolyte, for the anode. The cathode, fabricated as an extruded porous tube, is made of Lanthanum manganite, and the cathode interconnection consists of thin strip of Lanthanum chromite.

The tubular cell design offers different advantages with respect to planar ones; for instance, sealing problem is eliminated by inserting an air feeder tube down the cell tube. Tubular cells are more stable against mechanical and thermal stresses than planar cells. Nevertheless, modern technologies (tape casting, screen printing, vapour deposition. plasma spraying, wet spraying and others) allow lower costs for the fabrication of planar cells.

Microtubular cells have been developed since early 1990s when YSZ tubes with diameter ranging from 0.1 to 5 mm with thin (150 μm) and dense wall were produced. YSZ tube represents the electrolyte and the support for the electrodes that are deposited with a thickness of about 50 μm. Due to their narrow diameter and to the support thickness microtubular cells allow higher power density in comparison to traditional tubular cells but requires a more complex gas distribution system [14]. In the last years research in this field has brought to the development of new fabrication techniques [15]. For instance, anode

supported microtubular cells are produced allowing to increase the power output of these systems [16, 17].

Planar cells can be produced with different configurations: electrolyte supported (ESC), cathode supported (CSC), anode supported (ASC) and metal supported (MSC) cells [18-20].

For cells with thin YSZ electrolytes (5-20 μm) as for anode supported cells (ASC), the operative temperature can be reduced (< 800°C). Operating at this temperature condition allows a wider choice of materials (especially low-cost metallic materials for the interconnect), longer lifetime, reduced thermal stresses, improved reliability, and potentially reduced cell cost [21]. The main disadvantages are potential slow electrode reaction kinetics (and therefore high polarisations) and the reduced thermal energy that can be extracted from the hot exhaust stream by a turbine or a heat exchanger. ASC configuration is preferred to the other ones due to the low ohmic losses associated to the thin electrolyte.

In the following section it will be referred to the ASC with planar geometry being it the configuration considered in the present research work.

The voltage produced by a single cell is usually less than 1 V. As a consequence, for most practical fuel cells applications, unit cells must be assembly into a stack to achieve the voltage and power output level required for the application. Different stacking arrangements have been developed where electrically conductive materials are used as interconnects; these are often fabricated into complex shapes to respond also to other functions such as air and fuel channelling and sealing. Fuel and oxidant flow can be arranged to be cross-flow, co-flow, or counter-flow.

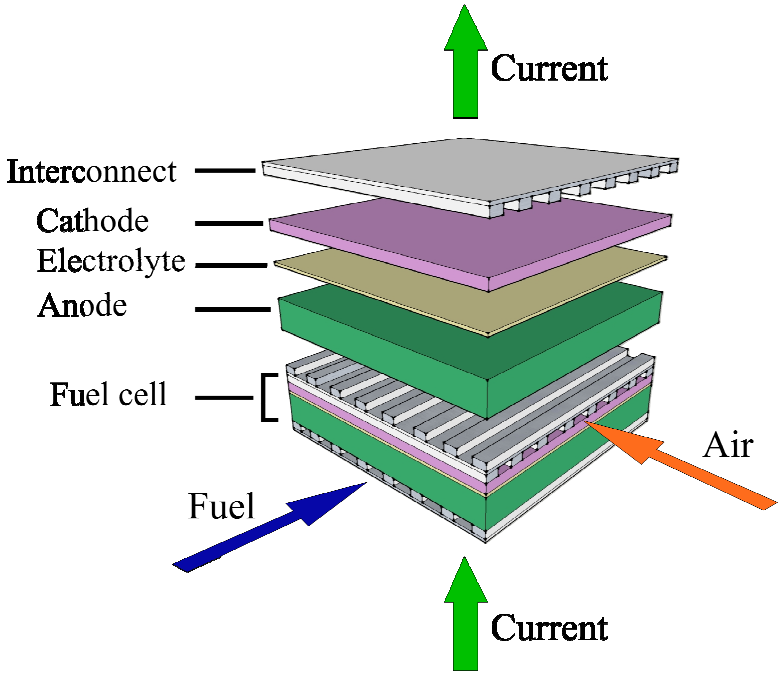

Fig. 1.3: Stack cells design for a planar anode supported SOFC.

A functional stack is constituted by different elements with specific properties. A sketch of anode supported SOFC in planar configuration is reported in figure 1.3. The cell is composed by two porous electrodes, anode and cathode, separated by a dense Oxygen ion-conducting electrolyte. Every cell is connected in series with another cell by an interconnect. A large number of units can be repeated in order to produce the desired power. Then a sealing system of anode and cathode compartment is needed in order to avoid the mixing and combustion of fuel and air.

In order to meet operating requirements of specified power generation applications the design of cell configuration, specifically planar SOFC, needs to fulfil different requirement [10]:

- In the stack ohmic losses need to be minimized in order to show good electrical performance. This can be obtained by considering the current path in the components to be as short as possible; there must be good electrical contact and sufficient contact area between the components. The current collector must also be designed to facilitate current distribution and flow in the stack.
- The design must provide for minimal polarisation losses so that high electrochemical performance is obtained. Therefore, any gas or cross-leakage and electrical short circuit must be avoided. Fuel and oxidant must be distributed uniformly not only across the area of each cell but also to each cell of the stack. Moreover, in order to decrease mass transport limitations, the gases must be able to rapidly reach the reaction sites.
- Stacks need to possess thermal compliance. In other words, the design must permit the highest possible temperature gradient across the stack and, in addition, must provide for stack cooling and uniform temperature distribution during operation.
- Stacks require mechanical and structural integrity. Planar SOFC stack must be designed in order to have adequate mechanical strength for assembly and handling. Therefore, mechanical and thermal stresses must be kept to minimum to prevent cracking, delamination or detachment of the components under variable operating conditions (for instance, normal operating temperature gradients, off-design temperature gradients, thermal shock conditions such as sudden power change and cold start-up, and mechanical loading expected during installation).

Cell-to-cell characteristics within the stack must be as uniform as possible. If a single cell in a stack exhibits higher resistance than the others, stack failure often initiates at such cell. The cell then exhibits lower voltage and even a negative voltage. If a cell exhibits negative voltage, the Oxygen chemical potential within the electrolyte can exceed that in the oxidant at the cathodic side and can drop below that in the fuel at the anodic side. This can lead to high internal Oxygen partial pressure resulting in electrode cracking and/or delamination, and very low Oxygen partial pressure leading to local electrolyte decomposition, respectively. Both situations can lead to cell and stack degradation [22].

Ageing and degradation remain fundamental problems to be solved before industrial scale production can start. In order to solve the disadvantages of this device it is necessary to know the characteristics, the materials and the operating conditions in detail. Many companies and research groups are involved in the study of such device carrying out accurate analyses in order to allow scale up and industrial commercialization of SOFCs. In the next section a brief description on the principles and materials used for the production of SOFCs is reported.

1.3 SOFC OPERATION PRINCIPLE

1.3.1 THERMODYNAMIC CONSIDERATIONS

Different fuels such as Hydrogen, carbon monoxide, natural gas and other hydrocarbons can be used in SOFCs.

The overall electrochemical reaction when Hydrogen is used is the oxidation of Hydrogen by Oxygen into water.

The Oxygen is adsorbed within the cathode and it is reduced producing Oxygen anion:

$$\frac{1}{2}O_2 + 2e^- \rightarrow O^{2-} \tag{1.1}$$

The Oxygen anions are transported through the electrolyte into the anode where they react with the adsorbed Hydrogen:

$$H_2 + O^{2-} \rightarrow H_2O + 2e^- \tag{1.2}$$

The overall reaction in the cell is the addition of the two previous semi-reactions:

$$H_{2(g)} + \frac{1}{2}O_{2(g)} = H_2O_{(g)} \tag{1.3}$$

The maximum electrical work (W_{el}) obtainable in a fuel cell operating at constant temperature and pressure is given by the change in Gibbs free energy (ΔG) of the electrochemical reaction:

$$W_{el} = \Delta G = -nFE_{eq} \tag{1.4}$$

where E_{eq} is the Nernst potential or theoretical open circuit voltage (OCV) that can be measured when there is no current in the circuit; *n* is the number of electrons exchanged in the overall reaction and F is the Faraday constant (96487 C/mol_{el}).
If the reactants and products of the cell reaction are in their standard states at the temperature of the transformation, the Gibbs free energy change is given by the standard value (ΔG^0) and by the reaction equilibrium constant (K_{eq}),

$$\Delta G = \Delta G^0 + RT\ln\left(K_{eq}\right) = \Delta G^0 + RT\ln\left(\frac{P_{H_2O}}{P_{H_2}P_{O_2}^{1/2}}\right) \tag{1.5}$$

The equilibrium constant for SOFCs typical operation conditions can be written as the ratio between partial pressure of products and reactants, instead of using the related fugacities, since in the usual operative conditions of SOFCs the gases behave as ideal.
Since:

$$\Delta G^0 = -nFE_{eq}^0 \tag{1.6}$$

by substituting Eqs (1.4) and (1.6) in Eq. (1.5), the equilibrium voltage of the overall equation (1.1) is given by Nernst equation:

$$E_{eq} = E_{eq}^{0} + \frac{RT}{nF}\ln\left(\frac{P_{H_2} P_{O_2}^{1/2}}{P_{H_2O}}\right) \quad (1.7)$$

Nernst equation provides a relationship between the ideal standard potential (E_{eq}^{0}) for the cell reaction and the ideal equilibrium potential (E_{eq}) at the partial pressures of reactants and products. It can be observed that the cell potential increases with an increase in the partial pressure (concentration) of reactants and a decrease in the partial pressure of products.

The standard Gibbs free energy for the reaction (Eq. 1.3) is ΔG_0=-228.59 kJ/mol [10], to whom corresponds E_{eq}^{0}=1.18 V.

The ideal standard potential depends on the fuel used in the cells. For instance, if SOFCs are fed with CO or methane the overall reactions are:

$$CO_{(g)} + \frac{1}{2}O_{2(g)} = CO_{2(g)} \quad (1.8)$$

$$CH_{4(g)} + 2O_{2(g)} = CO_{2(g)} + 2H_2O_{(g)} \quad (1.9)$$

and the corresponding ideal standard potential are E_{eq}^{0}=1.33 V and E_{eq}^{0}=1.04 V, respectively.

In real operation conditions, the fuel cell potential is lower than the theoretical one due to irreversibility losses associated with the current production.

A typical trend of the voltage (V) versus current density (i) for a generic fuel cell is shown in figure 1.4.

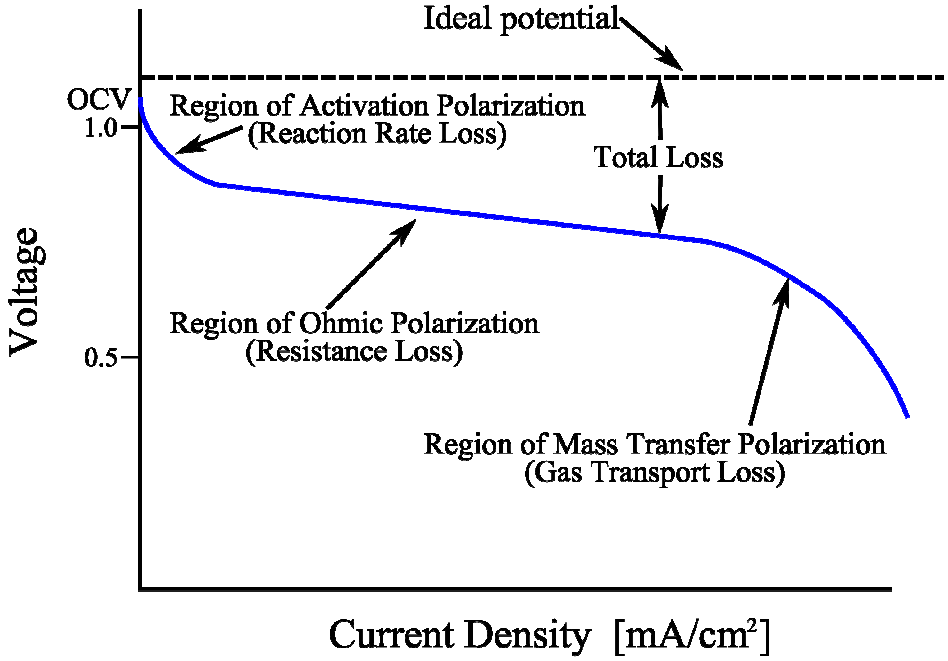

Fig. 1.4: Ideal Current – Voltage plot characteristic for fuel cell.

In such plot it is possible to see that the measured OCV is lower than the theoretical one.

At low current densities a rapid fall of potential is observed, then as the current density increases the voltage decreases slowly with a quite linear trend. In the last part of the curve, at very high current densities, a sharp voltage reduction occurs. This behaviour can be explained considering that there are different types of polarization losses which are dominant in different range of current density:

- ✓ Fuel crossover and internal currents
- ✓ Activation polarization (η_{act})
- ✓ Ohmic polarization (η_{ohm})
- ✓ Mass transfer losses or concentration polarization (η_{conc})

The operating voltage of the cell is:

$$V = E_{eq} - \eta_{act} - \eta_{ohm} - \eta_{conc} \quad (1.10)$$

Fuel crossover and internal currents

As mentioned in the previous paragraphs the ideal electrolyte should be exclusively ionic conductor and impervious to gases. In a real cell some fuel diffusion across the electrolyte and electron conduction can occur. The passage of the fuel from the anodic to the cathodic compartment results in its combustion without contributing to the electrical power generation. This small amount of wasted fuel is termed fuel crossover. On the other hand, a finite electrical resistance of the electrolyte causes an internal current from the anode to the cathode without passing through the external circuit. These two phenomena occur also at open circuit and explain the lower actual OCV in comparison to the ideal one. This kind of losses is more critical in fuel cells working at low temperatures (PEM), while are less important at high temperatures where the real OCV is approaching Nernst potential.

Activation polarization (η_{act})

An electrochemical reaction involves charge transfer at the electrodes interface which results in a current density. The latter is proportional to the reaction rate and determines a loss in cell voltage called activation polarization or overpotential.

In other words the activation polarization is the energetic barrier that is necessary to overcome in order to realise the reaction and it is correlated to the reaction rate. More in detail the activation polarization is correlated to the slower stage of the reaction that is realized at the anode/cathode compartment.

In a complex reaction as electrocatalytic oxidation in fuel cells, the rate determining step can be attributed to a different elementary step, such as the adsorption of the reactant into the electrodes surfaces, the electron transfer to the double layer, desorption of the products

from the surfaces and each of them are thermal activated; so η_{act} is correlated with many parameters (i.e. material properties, microstructure, atmosphere, and temperature).
Butler-Volmer equation correlates the current density with the overpotential:

$$i = i_0 \left\{ \exp\left[\frac{\beta n F \eta_{act}}{RT} \right] - \exp\left[-\frac{(1-\beta) n F \eta_{act}}{RT} \right] \right\} \tag{1.11}$$

where β is the transfer coefficient, ranging from 0 to1 and depending on the electrode material and reaction involved; i_0 is the exchange current density which represents the electron exchange across the electrode/electrolyte interface when the current density i is zero.
The contribution of activation polarization in the cell voltage loss is more evident at low current density.
In order to decrease this contributes it is possible to increase the reaction rate in both the electrodes, which is influenced by many factors (temperature, active area and activity of the electrodes); in fact it is possible to decrease the polarization losses by increasing the operative temperature, and/or the active area of the electrodes; moreover, by using an appropriate catalyst, it is possible to enhance the activity of the electrodes.

Ohmic polarization (η_{ohm})

Ohmic polarization is the result of losses due to the intrinsic electrical resistance of the electrodes and electrolyte materials. There is a linear relation between this polarization and the current density:

$$\eta_{ohm} = (\rho_e l_e + \rho_c l_c + \rho_a l_a + R_{contact}) i \tag{1.12}$$

where ρ_e, ρ_c, and ρ_a are respectively electrolyte, cathode, and anode resistivities and l_e, l_c, and l_a are respectively electrolyte, cathode, and anode thicknesses, and $R_{contact}$ is any possible contact resistance. The ohmic polarization contribution to total cell losses is important in the intermediate current densities range as shown in figure 1.4.

In most SOFCs, the main contribution to η_{ohm} is from the electrolyte; for instance, the ionic resistivity of the electrolyte state of the art material (YSZ) at 800°C is about 50 Ωcm. This can explain the superior performances behaviour of the ASCs, where the electrolyte is thin (less than 20μm), compared with the ESCs.

The ohmic resistance normalized by the active cell area is the Area Specific Resistance (ASR). The ASR is a function of cell design, material choice, manufacturing technique, and, operating conditions because material properties change with temperature. The ASR is a key performance parameter, especially in high-temperature fuel cells, where the ohmic losses often dominate the overall polarization of the cell.

Mass transfer losses or concentration polarization (η_{conc})

At high current densities the concentration polarization becomes more relevant. Indeed in this current range the reaction control passes from the chemical stage to the mass transfer stage. In other words, the limiting step of the overall reaction is the diffusion of the reactants from the bulk of the gases to the electrodes interface and/or the counter diffusion of the products.

The concentration polarization increases with the current density with a non linear behaviour, and is also function of parameters such as diffusivity and partial pressure of the gases and the electrodes microstructure.

1.4 SOFC COMPONENTS AND MATERIALS

The core of a SOFC stack is the cell. As mentioned a cell is constituted by different components: two electrodes (cathode and anode) and one electrolyte. Considering the planar ASC, each cell is electrically connected to the others through metallic interconnects. Due to the high operating temperature, and to the all-solid state nature of the components, the coefficient of thermal expansion of each material composing the stack must be as close as possible, in order to avoid mechanical fracture and material delamination due to thermal stresses that develop during thermal cycling of the cells. Moreover, they require to be stable at high temperatures (they operate at 800-1000°C) and to be produced with cost-effective materials.
The characteristic and the properties that the stack elements must possess are briefly described in the following, focusing on the planar anode supported cells configuration, being the kind of cells investigated in the present work.

The schematic representation of a planar SOFC is reported in figure 1.5. The two porous electrodes, anode and cathode, are separated by the dense ionic conductor electrolyte. The cathodic compartment is fed with a comburent, typically air, where the molecular Oxygen is reduced into Oxygen anions O^{2-} by the external electrons provided through an electrical circuit. Due to the difference in Oxygen chemical potential between cathode and anode the Oxygen anions go towards the anode through the electrolyte. In the anode the Oxide anions oxidize the fuel, usually Hydrogen, to give water, heat, and electron as product.

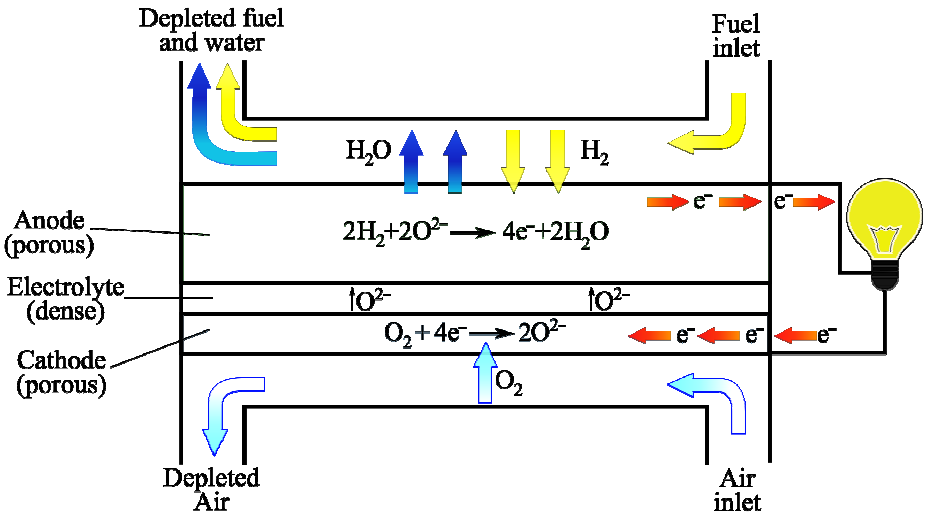

Fig. 1.5: Schematic picture showing the operating principle of SOFC.

1.4.1 *CATHODE*

The cathode is kept in oxidising atmosphere during operation. The molecular Oxygen diffuses through the cathode and reduces at the interface with the electrolyte into Oxygen anions. For this reason the cathode materials need to be stable in this environment, have a high ionic and electronic conductivity and catalyze the dissociation of Oxygen. They must have a high porosity in order to let the Oxygen to reach easily the electrolyte surface where there are the active reaction sites, known as triple phase boundary (TBP). The active sites concentration should be high in order to ensure good cathode performance. Other important requirements that a cathode should fulfil are a good adhesion with the electrolyte interface and chemical compatibility with adjacent cell components [23, 24].

In anode supported cells the cathode is a thin layer to avoid mass transfer losses, but at the same time has to provide sufficient in plane conductivity.

Usually the cathode is produced by using ceramic materials, typically Lanthanum manganites. They have a perovskite-structure oxide that exhibits p-type electronic conductivity. In order to increase their electronic conductivity they can be doped with lower-valence cations, such as Strontium, Calcium, Barium, Nickel or Magnesium, or by other alkaline- or rare-earth cations [25, 26]. The state of art for cathode materials when YSZ is used as electrolyte are Strontium doped $LaMnO_3$ (LSM) and Strontium doped Lanthanum cobaltites (LSC) for their high electrical conductivity as well as for thermal expansion and chemical properties compatible with other SOFC component materials [27].
LSM applications are limited to temperatures higher than 800°C; instead at lower temperatures LSC are the preferred cathode materials due to their good electrical conductivity in this range of temperatures [28, 29]. Many alternative and promising materials based on rare earths perovskites are currently under development [30].

1.4.2 *ELECTROLYTE*

The selection of the electrolyte material into the solid oxide fuel cells determines the operative temperature of the cells. Indeed electrolyte needs to show different properties to be selected, first of all an elevated Oxygen ionic conductivity which strongly depends on temperature. This is because Oxygen anions are the mobile species migrating through the electrolyte from the cathode to the anode. Other features that an electrolyte necessitates to satisfy and are not less important than the previous one are: it must show a minimal electronic conductivity to avoid short circuit into the cell, have a high density in order to inhibit the fuel crossover with consequent fuel combustion. In addition it needs to be chemically stable into the reducing and the oxidising atmospheres, being in contact with both the two electrodes. To minimize ohmic losses this layer must be produced as thin as possible (for ASC). Finally the electrolyte must exhibit good mechanical resistance in order

to avoid cracks or pores formation either during manufacture or in the course of long-term operation.

Fluorite-structured oxide materials such as yttria stabilized zirconia (YSZ), rare earths doped ceria, and rare earths doped Bismuth oxide have been widely investigated as electrolyte materials for solid oxide fuel cells [23, 31]. Among these materials YSZ has been successfully employed, and currently is the state of art as electrolyte material. It can be used either as 3YSZ, i.e. ZrO_2 doped with 3 mol% Y_2O_3 (TZP) or 8YSZ, i.e. ZrO_2 doped with 8 mol% Y_2O_3 (CSZ). Although the oxide ion conductivity of 3YSZ is significantly lower than that of 8YSZ, this material is advantageous because of its outstanding mechanical stability.

Yttrium oxide (Y_2O_3) is introduced as dopant into the zirconia for two reasons:

✓ It stabilizes the high temperature cubic phase that posses the highest ionic conductivity between the different crystal phases. In fact the pure zirconia exists in three crystal phases at different temperatures. At very high temperatures (>2370°C) the material has a cubic structure (c). At intermediate temperatures (1170 to 2370°C) it has a tetragonal phase (t). At low temperatures (below 1170°C) the material transforms to the monoclinic structure (m). In nature these transformations are martensitic and the transformation from tetragonal to monoclinic is rapid (by cooling) and is accompanied by volume increase that causes extensive cracking in the sintered material. This behaviour leads to dramatic failure of fabricated components during cooling and makes pure zirconia useless for any structural or mechanical application. Instead the use of Y_2O_3 or other oxides such as CaO, MgO, Sc_2O_3 and rare earth oxides as dopant can stabilise the monoclinic structure in the cubic or tetragonal form.

✓ It increases the oxide ionic conductivity introducing Oxygen vacancies. For instance one mole of Oxygen vacancy is created for each mole of Y_2O_3 dopant, as can be observed by the defect reaction written in the Kroger–Vink notation:

$$Y_2O_3 \xrightarrow{ZrO_2} 2Y'_{Zr} + 3O_O^x + V_O^{\bullet\bullet}$$

where $Y_{Zr}^{'}$ is the lower valence cation, O_O^x is the oxygen ion on normal sites and $V_O^{\bullet\bullet}$ is the Oxygen vacancy [32].

Moreover zirconia has good thermal and mechanical shock resistance when doped with yttria (Y_2O_3), scandia (Sc_2O_3), samaria (Sm_2O_3) and magnesia (MgO).

The Oxygen ionic conductivity behaviour of electrolyte materials against the temperature can be observed by the graphic reported in figure 1.6, where it is possible to see that different materials such as $Ce_{0.9}Gd_{0.1}O_{1.95}$ and $Bi_2V_{0.9}Cu_{0.1}O_{5.35}$ posses at lower temperature higher conductivity than $(ZrO_2)_{0.9}(Y_2O_3)_{0.1}$. But this condition is not sufficient to choose them instead the doped zirconia as electrolyte material; in fact, for instance, $Bi_2V_{0.9}Cu_{0.1}O_{5.35}$ is not stable in the reducing environment of the anodic compartment of a fuel cell. It has to be also stressed that, among the candidate materials, yittria stabilized zirconia is a relatively cheap base material.

In addition it is sufficient to produce YSZ electrolytes with a thickness lower than 15 μm to have a specific ionic conductivity greater than 10^{-2} Scm^{-1} at 700°C that allows to obtain an ASR of 0.15 Ωcm^2 and ensure that the total internal resistance of a fuel cell is sufficiently small [6].

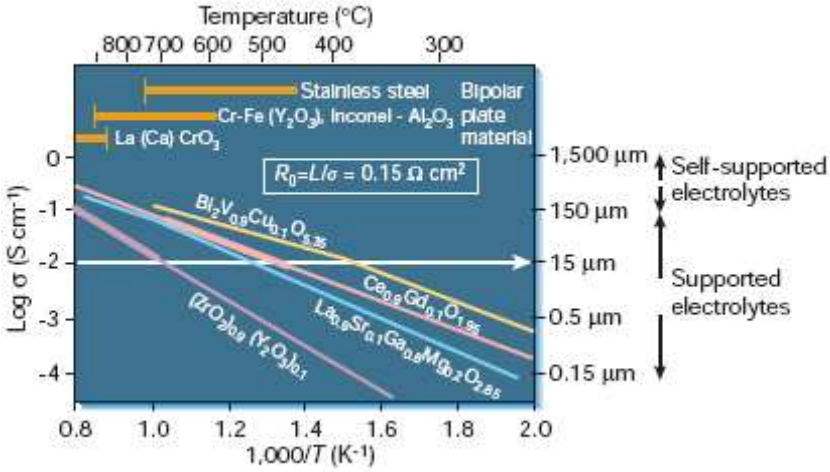

Fig 1.6: Oxygen ion conductivity vs. reciprocal temperature for different doped oxides for SOFC electrolyte [6].

Even if YSZ based electrolytes represent the state of the art materials, ceria based materials seem to be promising candidates for electrolyte production and are object of an intense research [33].

Pure ceria has a fluorite-type structure over wide ranges of temperature and Oxygen partial pressure. The electronic defects concentration and conductivity are directly related to the degree of non-stoichiometry that increases with the temperature and decreases with Oxygen partial pressure. Doping of ceria with a number of oxides such as CaO, Sm_2O_3, Gd_2O_3, Yb_2O_3, Y_2O_3, La_2O_3, increases the concentration of Oxygen-ion vacancies and the material exhibits high ionic conductivity.

On the other hand, for instance, Gd doped CeO_2 (GCO) become mixed conductor in reducing atmosphere, so the fuel can pass through the electrolyte into the cathode compartment resulting in an internal short circuit of the cell. Consequently, a decreased open circuit voltage (OCV) and an additional fuel utilization even under OCV-conditions takes place, thus lowering the system efficiency [30].

Other alternative materials are the oxide having ABO_3 perovskite structure; this structure is extremely amenable to tailoring via doping on both the A and B cation sites. A large variety and concentration of dopants can be accommodated in a wide range of host compounds. Introduction of divalent dopant ions, in general Strontium and Magnesium, into the Lanthanum and Gallium sites (LSGM: $(La,Sr)(Ga,Mg)O_3$), respectively, of Lanthanum gallate $LaGaO_3$ produces a material with a high concentration of mobile Oxygen vacancies and thus high Oxygen ion conductivity. On the other hand, they do not show long term stability due to Ga evaporation in a reducing atmosphere. Moreover, Lanthanum gallate undergoes deterioration for its reactivity with Nickel, the typical SOFC anode electrocatalyst [30-35]. In addition, the use of LSGM as electrolyte shows problems due to the low mechanical stability and the high costs of Gallium.

So far zirconia based oxides remain the best and more cost effective electrolyte materials. Sc-doped ZrO_2 electrolytes are the most promising alternative as this dopant material allows to increase the ionic conductivity significantly for reduced operating temperatures so far. On the other hand the low quality of ScSZ-powders available, and the high cost of Scandium restricted its use.

A further consideration is that the electrolyte needs to show a high strength and toughness especially in planar configuration. Several fuel cell developers add a small quantity of alumina to YSZ based electrolytes to enhance the mechanical strength [31, 36-39].

1.4.3 *ANODE*

The electrochemical oxidation of the fuel is realized into the anodic compartment. If Hydrogen is used as fuel the oxidation products are water vapour and electron as evidenced in Eq. 1.13:

$$2H_{2(g)} + 2O^{2-} \rightarrow 2H_2O_{(v)} + 4e^- \qquad (1.13)$$

The porous anode in SOFCs offers the sites for the fuel gas to react with the Oxygen ions delivered by the electrolyte, within a structure which also facilitates the necessary charge neutralisation by its electronic conductivity.

In order to have a SOFC with high performance also the anode material must exhibit different properties [23].

The anode has to be chemically stable in reducing atmosphere, show high electrochemical/catalytic activity, necessary for the kinetic of the reaction, be sufficiently porous to permit efficient transport of the fuel to the active sites and to remove products such as water. For the anode supported cells (ASC), it needs to be thick enough and show a good mechanical strength; for the latter a compromise with the porosity is necessary. Moreover, the anode must be chemically compatible with the electrolyte and with the interconnect materials without interdiffusion between adjacent layers; high wettability with respect to the electrolyte substrate is extremely important in order to have a good adhesion between the layers and avoid delamination during operations. Anode necessitates to match the shrinkage during sintering and the thermal expansion coefficient with the neighbouring components in order to minimise stresses caused by temperature variations during operation, start-up and shut-down.

In addition, it must present corrosion resistance to the fuel and the impurities therein; specifically, it needs to avoid coke deposition and to be tolerant to Sulphur present in the fuel. Preferably, anode should show catalytic activity toward the hydrocarbons reforming. It needs to be stable over a wide range of temperatures, from the sintering temperature during fabrication to normal operating conditions and then, frequently, to cyclic shut-downs to ambient temperature. The anode, as before mentioned, works in a reducing atmosphere, with a very low Oxygen partial pressure, but the latter can increase, and to lodge fault conditions, so the anode needs to be chemically stable in oxidizing conditions, even after short and/or repeated exposures to air at high temperatures showing then stability to redox cycles (alternative change of atmosphere: reducing-oxidising).

The performances of a SOFC depend strongly from the anode microstructure and it is very important to understand the phenomena involved in the anode during operation.

The electrochemical reaction takes place only in a particular zone namely three-phase boundary (TPB). In this zone, Oxygen ions accessible from the electrolyte reacting with the fuel can discharge electrons to the conducting anode. This requires a gas phase for the fuel access, an electrolyte phase for oxide ion entry and a metal phase for electrons output. The anodic microstructure must provide an active volumetric reaction region in three dimensions homogeneously distributed through the anode in order to have good efficiency and low losses at operation conditions. The absence of one of this phase due to the breakdown in connectivity has as consequence that the reaction cannot occur being not catalyzed. In addition, a site will not contribute to the performance of the cell if the gas cannot reach the site or the electrons cannot be removed from the site.

Consequently, anodes materials selection and production techniques are very important in determining a structure with high TPB concentration and stable during cell operation life.

Considering the polarisation losses in the anodic compartment it can be observed that:

- ✓ Activation polarization is related to the charge transfer processes, as before explained, and depends on the electrocatalytic activity of the anode and then on the extent of the triple-phase boundaries zone (electrode, electrolyte, and fuel).
- ✓ Ohmic resistance that includes: *(i)* the internal resistance, related to the resistance to the transport of electrons within the anode and therefore to the electronic resistivity and thickness of anode; *(ii)* the contact resistance due to low adhesion between anode and electrolyte layer.
- ✓ Concentration polarization depends on the transport of gaseous species through the porous anode and, thus, on the anode microstructure, or, in other words, on the volume percent porosity, the pore size, and the tortuosity factor.

In the research of an anode material that could accomplish the most of the peculiarity exposed, at the beginning of SOFCs development the attention focused to single phase materials counting graphite, Platinum, Iron, Cobalt, Nickel and other transition metals. But it was stated that each of them presented physical and chemical instability and cannot be

used. For instance, graphite is electrochemically corroded so it cannot be used; Platinum during operative work spalls off probably for the water vapour development at the metal - oxide interface; corrosion of Iron is observed when the partial pressure of oxidation products in the anode compartment exceeds a critical value [9, 40].

The use of the Nickel evidenced significant thermal expansion mismatch with YSZ electrolyte; the metal aggregates by grain growth at high temperatures, with consequent decreasing of anode porosity and three-phase boundaries required for cell operation [9, 41].

The anode material that fulfils great part, but not all, of the previous requirements is, until now, a mixture of ceramic and metallic materials, the porous Ni/YSZ cermet.

Use NiO and YSZ powders as starter materials for anode production present different advantages instead of use pure Nickel. No reaction occurs between the anode and electrolyte being Nickel and YSZ not miscible even at high temperatures. Electronic conductivity and catalytic activity are provided by Ni in the cermet anode; instead, the rigid ceramic YSZ structure constitutes the network where the Nickel is dispersed, and gives mechanical resistance to the anode, especially for the ASC; moreover, YSZ lowers the activation polarization since it serves as a pathway for Oxygen ions migration and therefore extends the triple phase boundary region inside the anode (being usually limited to the interface between the electrolyte and other anode materials); in addition YSZ adjusts the coefficient of thermal expansion (CTE) close to that of YSZ electrolyte.

A particular and important issue in the Nickel based anode is related to the fact that, during operation at high temperature, and under electric load Ni tends to sinter, coarsen and agglomerate. These in tumble give: (i) a decrease of anodic porosity and of the active sites available for oxidation (having a negative effect on the gas transport and reaction kinetics) that determines an overall efficiency decrease of the fuel cell by increasing the polarization losses; (ii) an increase in the redox instability.

The addition of YSZ to form a Ni/YSZ composite reduces, but do not remove, the sinterability, and the Ni agglomeration kinetic during SOFC operation and the related consequences [42].

It is worth noting that the NiO and YSZ powders are relatively cheap in comparison with other anodic raw materials.

In the ASC configuration the sintered anode is constituted by a thick YSZ network where NiO is distributed. At the start up of the cell Nickel oxide is reduced with H_2 in order to have the activation of the catalysis sites for the H_2 oxidation. The reduction of NiO into Ni metallic (Eq. 1.14) is accompanied by a 40.9% Nickel phase volume reduction based on dense NiO [43] with consequent increase of the anode porosity.

A porosity of 30–40 vol% is necessary to supply the gas for the reaction and to remove the reaction products [44]:

$$NiO + H_{2(g)} = Ni + H_2O_{(v)} \tag{1.14}$$

The amount of Nickel contained in the cermet influences the electrical conductivity of the anode. The percentage of Ni in the cermet is determined in order to assure the percolation threshold, this is the adequate amount of Nickel for continuity of the electron conduction. The S-shaped curve correlates the conductivity of the cermet as a function of Nickel content as reported in figure 1.7.

The quantity of Nickel in the anode has to be at least 30 vol% into the cermet, in order to ensure sufficient electronic conductivity. This concentration is the threshold value at which the conduction mechanism switches from ionic to electronic. Usually Nickel is found in concentrations of 40-60% in the anode cermet with a porosity of 20-40%, the latter to facilitate the mass transport of reactant and product gases [23].

From the comparison of the cermets sintered at different temperatures (Fig. 1.7) it can be observed that an increase in the sintering temperature results in a lower percolation threshold, which might be attributed to a decreased porosity as well as a narrowed pore size distribution [41].

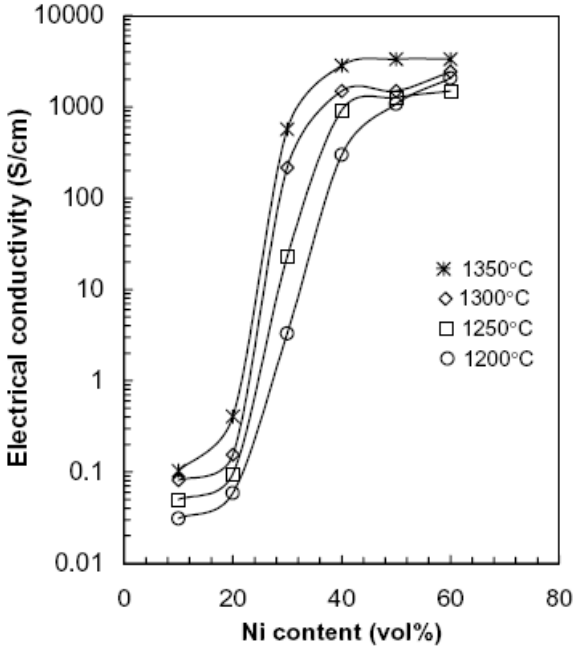

Fig. 1.7: Variation of electrical conductivity measured at 1000°C as a function of Nickel concentration of Ni/YSZ cermet fired at different temperatures [45].

As reported by Zhu and Deevi [41], porosity, pore size, size distribution, and size of raw powders as well as contiguity of each component influences the percolation threshold and, as consequence, also the Ni/YSZ cermet electrical behaviour; for instance, particle sizes of YSZ and of Nickel affect the electrical conductivity, that increases with an increase of the ratio of their size (dYSZ/dNi), for a fixed Ni amount and porosity. In order to have an anode showing high electrical conductivity, stable microstructure, as well as sufficient porosity, it is necessary an optimization of all processing variables since from the mixing of the selected raw materials, preparation, sintering temperature [46, 47]; moreover, the fuel composition and gas flow rates influence the FC overpotential [41].

In some anode supported cells, in order to enhance cell performance, a dense Ni rich anode functional layer is introduced between the anode and the electrolyte. For the functional

anode the goal is a fine microstructure with as large a TBP as possible and connectivity in both Ni and YSZ phases. The activity depth of the functional anode is of the order of 5 to 10 μm and usually layers of 20 to 30 μm are used [48]. On the other hand this thin layer, due to its density, is more sensible to redox degradation.

As before mentioned, the Ni/YSZ cermet do not accomplish all the ideal anode properties; indeed it presents different disadvantages during the fuel cell operation such as:

(a) poor redox stability;
(b) Nickel agglomeration after prolonged operation;
(c) low tolerance to Sulphur;
(d) carbon deposition when using hydrocarbons as fuel.

The last two issue are related to the use of the fuel. The degradation of cells due to redox instability is explained in depth in the following.

As mentioned before, the operating temperature of a SOFC is controlled by different thermal activated processes like the Oxygen ion conductivity of the solid electrolyte and different chemical and electrochemical reaction steps in the electrodes or at the electrode/electrolyte interfaces. A decrease in the operating temperature generally results in increased losses of the cells and a decreased power density at a constant efficiency. On the other hand, the long term stability of the system is improved and the system costs can be reduced by using cheaper metal alloys for interconnects and for external components.

Moreover, if the device is used under pressure as SOFC/gas-turbine hybrid system the temperature is restrained.

Therefore the development of cost effective alternative materials and components for SOFC-systems working at about 800°C is necessary [30]. Although alternative materials can be considered in order to overcome these disadvantages [49-51] they do not posses similar high performance and low cost as the Ni/YSZ cermet. All this areas are under development in order to decrease their degradation phenomena.

1.4.4 *INTERCONNECT*

A single cell produces a potential lower than 1V. In order to increase the voltage output for practical applications it is necessary to pile-up different cells in a stack. In the case of planar cells, these are superimposed and the anode of one cell is separated from the cathode of another by an interconnect. The latter has two functions:

- Ensure the electrical connection between adjacent cells;
- Separate anodic and cathodic compartments of neighbouring cells.

Interconnects must comply with many requirements: high temperature oxidation and reduction resistance; stability under multiple chemical gas streams; high electrical conductivity and high density with closed porosity; in addition they necessitate a good thermal conductivity, phase stability over wide temperature range, need to be resistant to Sulphur poisoning, oxidation and carburization and moreover, for planar configurations, show strong and high creep resistances.

The most common interconnect material, for high temperature SOFCs, is alkali doped $LaCrO_3$ (Lanthanum chromite), with the specific dopant (typically, Sr, Ca or Mg) and concentration being selected to best match the thermal expansion of the other fuel cell components in the geometry of interest. The problem with the Lanthanum chromite is its difficult to process because of chromia evaporation at high temperatures, which leads to poor densification [35].

With the development of SOFCs working at temperatures ranging from 600 to 800°C cheaper materials, such as metallic alloys, can be used as interconnects. Metallic interconnects if compared to ceramic materials, result stronger, easier to form, have higher thermal and electrical conductivities and negligible ionic conductivities, but a thermal expansion coefficient that tends to be higher than most of the other cell components.

Nevertheless, ceramic materials can be considered superior at high temperatures because the oxidation of the metallic interconnects on the cathode side occurs with formation of an oxide layer. This oxide layer, usually made of chromia, has a poor conductivity and can be

detrimental during long-term operation, and is prone to cracking and spalling [23]. Moreover, Chromium evaporation occurs at operation temperatures causing irreversible poisoning of cathode active sites [52].

Among the metallic interconnects the most used materials are ferritic steels because they are cheaper and easier to process then the other candidate alloys. Different efforts were undertaken to develop more suitable compositions, which led to the development of several special alloys. Currently Crofer22 APU (Krupp) is widely used.

To reduce the degradation of metallic interconnects, a protective coating is applied on their surfaces.

Usually the materials used for the coating are perovskites as Lanthanum Strontium manganite (LSM), or Lanthanum Strontium cobaltite (LSC). It was observed that the presence of Manganese leads to the formation of a Mn-Cr spinel having good conductivity, and the reduction of Chromium evaporation, thus improving the long term performances of the cells. In the last years Mn based spinels as Cobalt manganite (Co_2MnO_4) were successfully applied as coating showing an important improvement in the cathode protection assuring a high conductivity to the interconnect [53, 54].

1.4.5 *SEALING*

In planar SOFCs, sealants attach the cell to the interconnect and/or metal frames as well as seal all possible leakage points. The choice of sealing materials has to be done according to many requirements: they need to be cheap, electrically insulating, their thermal expansion coefficient must be compatible with other cell components. In addition, they must be chemically and physically stable at high temperatures in both reducing and oxidizing environment and gastight; moreover, they need to be chemically compatible with other components and provide high mechanical bonding strength.

Three type of sealing can be considered: rigid bonded seals, compressive seals, and compliant-bonded seals. Specifically, rigid-bonded seals are the most common and are usually made from glass or glass-ceramic materials [23]. This type of seal is attractive considering that their viscous/wetting behaviour facilitates hermetic sealing; they are cheap and easy to manufacture and apply and fulfil many of the key properties required for a sealing material; in addition, glass-ceramics can be designed to avoid viscous flow and uncontrolled progressive crystallization during operation.

On the other hand they have different inconveniences due to their fragility, leading to seal and even cell failures during cool-down, and tendency to interact with adjacent cell components, especially with the interconnects [55-57]; in addition some of the constituents of glass volatilize during operation including Silicon, Boron, and alkali metals [4]. These constituents will likely foul or poison the electrode catalyst or interact in an undesirable manner with other cell components. Many studies are carried out to overcome these problems.

1.5 SOFC ISSUES

This section deals with one of the problems related to an easy commercialization of SOFC. In fact, in spite of the great potentiality of solid oxide fuel cells (SOFCs) there are still several problems that need technological solution and make these devices still not available for a large scale use.
In this paragraph the redox instability of the planar anode supported SOFC is discussed in detail being one of the most relevant obstacles for the production of reliable SOFC systems. Considering that the aim of this work was to increase the tolerance to redox cycle a detailed description of the redox phenomenon is necessary.

1.5.1 *REDOX INSTABILITY*

Among SOFCs the anode supported configuration shows the best electrochemical performances due to the thick anode (range 100-1000 μm) constituted usually by a Ni/YSZ cermet and a thin electrolyte (YSZ) (ranging between 6-20 μm) that minimizes the ohmic losses in comparison with the other cell configurations.
Indeed, Nickel is a good electronic conductor and an excellent electro-catalyst for the electrochemical Hydrogen oxidation; moreover the YSZ framework constitutes a good Oxygen ions conductor. In addition Ni/YSZ cermet has a high chemical stability in reducing atmosphere and has a good matching of thermal expansion coefficient (CTE) with YSZ electrolyte [13, 30, 41].

One issue still present on Ni/YSZ based anode supported cells is the instability to redox cycles. As reported by Wood et al., out of 10 references found in the technical

literature using anode-supported cell architecture, none report multiple redox cycles with no degradation due to microstructural modification of a Ni-YSZ anode [43].

During fuel cell operation the anode is in a reduced state, but for different reasons the anode can re-oxidize: for instance, discontinuous fuel supply, emergency stop, system shutdown without fuel, overpotentials or insufficient fuel permeation through the anode can determine undesired oxidation of the metal phase within the cermet, this being responsible for the phenomenon usually defined as redox instability.

A model of the microstructure evolution during reduction and subsequent oxidation was developed by T. Klemensø et al. [58]. The model is reported in figure 1.8 to better explain the microstructural modifications due to the redox phenomenon.

As sintered, the anodic microstructure appears with low porosity and NiO is uniformly distributed into the YSZ network, in order to guarantee the percolation (Fig. 1.8a).

During the first operation, NiO is reduced into metallic Ni. This process is associated with a volumetric shrinkage, an increase in porosity, and a restructuring of the Ni network (Fig. 1.8b). Due to the high operating temperatures (600 to 800°C), Nickel particles tend to coalesce and coarsen (Fig. 1.8c). Fuel supply interruptions, overpotentials and leakages can cause the re-oxidation of Ni to NiO, with a consequent volumetric expansion. After the re-oxidation the microstructure is different with respect to the as sintered state, due to the modification realised during the operative condition (reduced state). In fact, the NiO particles grow, and their final volume can be higher than the initial one: in such a case, anode bulk expansion occurs and anode internal stresses develop, with consequent crack formation into the YSZ network and into the electrolyte which can results in a loss of electrochemical performances and, worst, lead to the failure of the cell (Fig. 1.8d) [43, 48, 59, 60].

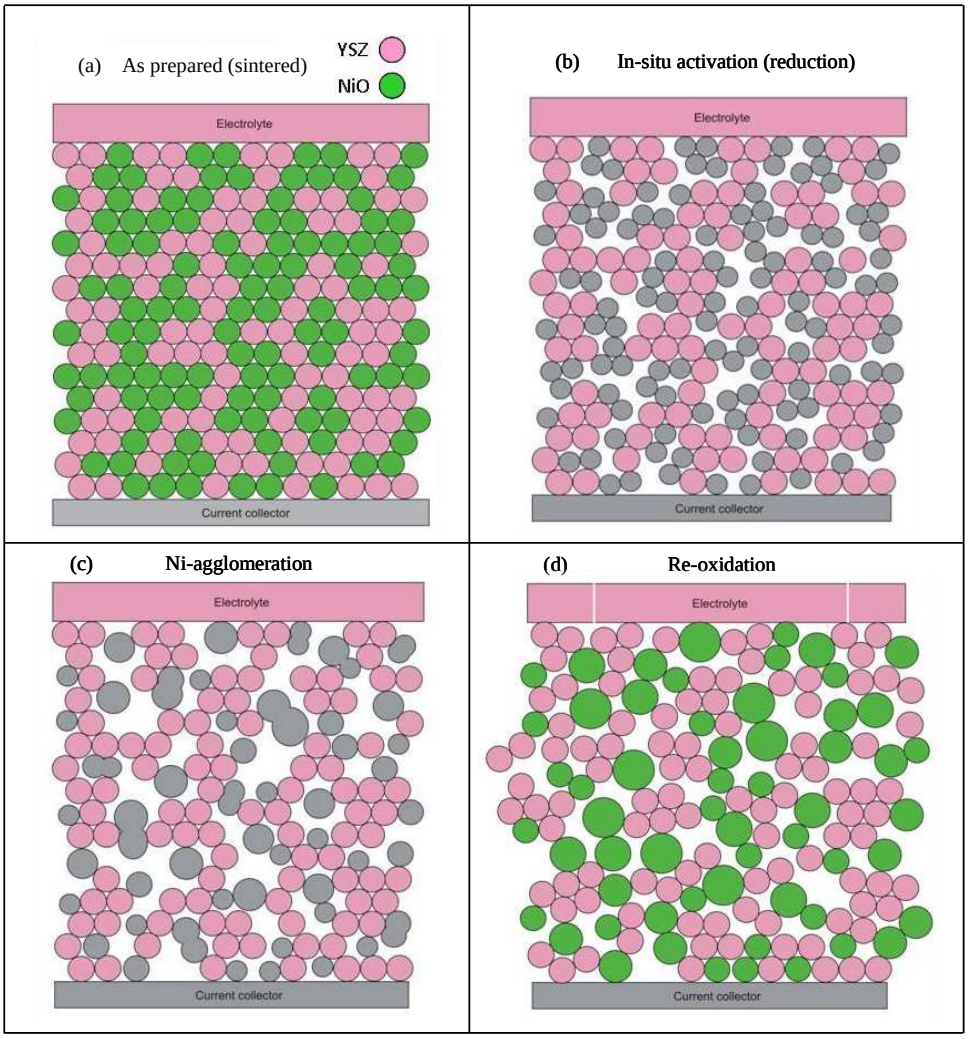

Fig. 1.8: Illustration of anodic microstructure change due to redox cycle [58].

In the last years many investigation were developed by different research groups on the mechanism and characterization of the redox behaviour, but it is still far to solve the problem [61].

Klemensø and Mogensen improved later the proposed model of the process occurring during more redox cycles from the results obtained by direct current (DC) conductivity measurements and by thermo-gravimetric study of redox kinetics. They observed that the anode electrical properties depend on samples porosity; the decrease in the electronic conductivity reflects Ni coarsening and agglomeration. Oxide growth mode causes damages to the YSZ network but may also promote improved percolation of the Ni/NiO network until a critical porosity [62].

Different approaches were used to examine the redox phenomenon, in order to understand the kind of modifications necessary to overcome this issue. Ni-based anode specimens with apposite composition and having different shape such as discs, bars or powder were tested in order to investigate the effect of redox cycling.

For instance, D. Sarantaridis et al. [63] investigated the redox behaviour in order to determine the critical degree of oxidation for ASCs that leads to irreversible mechanical damage. To obtain these data they oxidised two different configuration cells: free-standing cells were oxidized in air and cells that were sealed at their periphery to the fuel plate were oxidized electrochemically. They observed that free-standing cells resulted in failure at a critical degree of oxidation of about 50%, instead the constrained cells were fully disrupted with a critical degree of oxidation of about 5%. Moreover, they gave an interpretation of mechanical failure and noticed that a non-uniform oxidation process have more catastrophic effects than an uniform one. They considered that peripheral tensile stresses can be generated if the oxidation is non-uniform and concentrated in the central part of the cell. This leads to a central zone of expansion that creates a radial compressive stress in the surrounding material and a tensile hoop (tangential) stress.

In order to improve the redox tolerance of anode supported fuel cells, several solution have been proposed [64-68].

Wood and al. [43] in their paper reported a categorization of the possible solutions; they considered system solutions (such as purge gas or cell reversal, high temperature check valves and so on) and unit cell or material solutions. The former are expensive and need a deep evaluation on a number of criteria including effectiveness of solution, efficiency, amount of additional system equipment, safety and technical risk. The latter are less expensive since do not require special system power or control. Inside this category are considered: materials alternative to Ni/YSZ cermet anodes, microstructure modifications, changes in kinetic of reactions, improved sealing and lower stack operating temperatures.

Use of alternative materials

One possible solution to solve redox instability is the utilization of alternative anode materials to Ni/YSZ cermet and the choice of substances that are not as susceptible to oxidation, or better that do not posses relevant dimensional variation due to change of oxidative state.

The continuous search for alternative anode materials is primarily centered on perovskite-related structures, but also other materials are investigated such as fluorite, pyrochlore and Tungsten bronze. Many researches are currently focused on this topic [40, 64, 68-71].

A possible approach could be to choose a ceramic based anode such as Lanthanum chromite or doped Strontium titanates. The key problems with these materials up to now are the low electrochemical activity, low electrical conductivity, and high cost in comparison with Ni/YSZ cermet [43].

However, at the time being there are few anode materials alternative to Ni/YSZ cermet.

Tietz et al. analysed the conductivity and the dimensional variations during redox tests of different alternative anode materials, i.e. n-type conductors as Yttrium or Lanthanum doped Strontium titanates and p-type conductors as $Sr_{1-x}La_xB_{1-y}Mn_yO_{3-\delta}$ (B=Al, Ti). They carried out that most of the ceramics with n-type conductivity or substitutions with manganese leading to p-type conductors do not realize the requirements of a redox stable anode substrate material. Either they showed a too high chemical expansion or a too

low electrical conductivity and insufficient chemical stability. They detected that only the series $Sr_{1-x}Y_xTiO_{3-\delta}$ or $Sr_{1-3x/2}Y_xTiO_{3-\delta}$ ($0<x<0.08$) shown promising properties [72].
Thus, if the anode material remains unchanged and system redox solutions are considered too expensive, the only remaining solution to improve SOFC redox tolerance is to modify the microstructure of the anode.

Modification of microstructure

In order to minimize the degradation of the cell, and consequently of the device, due to the volume changes associated with redox cycles, modification of anode microstructure can be considered a possible solution. At the same time it is in necessary that the modifications introduced into the microstructure do not decrease the electrochemical performance of Ni/YSZ cermets.

Malzbender et al. tested redox tolerance of anode supported cells constituted by a thin electrolyte and anode with a porous current collector and a dense functional layer. They observed that upon re-oxidation the resulting NiO particles show an increase in volume in comparison with the as sintered state due to their spongy structure.
The expansion of NiO led to a compressive stress into the anode and to tensile strain and stress in the electrolyte that determined the formation of fractures into the electrolyte. This means that the stresses induced by NiO expansion overcome both the modulus of rupture and the compressive residual stresses of the electrolyte. They suggested, then, that a possible solution to decrease the redox instability effects is to increase the anode porosity in order to minimize the stress developed by NiO expansion [73].

Viable methods for anode porosity increase in order to improve the cells performance were studied by many research groups that did not characterize the redox stability of the produced anodes [74-78].

For instance, Morales et al. [79] discussed the use of fugitive materials to introduce a tailored porosity into the SOFC electrodes. The authors mixed PMMA beads with sub-micrometric size into anodic and cathodic slurries producing electrodes with a homogenous

porosity. They observed that a cell with electrodes having increased porosity (PMMA addition) shows an improvement in electrochemical performances in comparison with a cell produced by conventional route.

Clemmer and Corbin [80] produced anodes with mixtures of YSZ, Ni and graphite particles or YSZ and Nickel coated graphite particles. They also stated that the use of fugitive materials may increase the cell performances by achieving an improved Ni particle distribution and as consequence allows to decrease the percolation threshold.

Instead Rainer et al. studied the feasibility of porous anodes prepared by adding polyurethane (PU) foam precursors into the anodic slurry [81]. By changing the ratio between powder and PU foam, different percentage of porosity can be obtained. In particular, the authors observed that a good compromise between mechanical stability and network homogeneity can be achieved with 20 vol% ceramic load.

The modification of the microstructure can be also achieved by changing or grading the Ni/YSZ ratio, or by adding an oxidation barrier onto the anode side in contact with the fuel in order to avoid Oxygen diffusion into anode matrix [43].

For instance, Waldbillig et al. produced cells starting from an anode substrate where a graded double anode functional layer (AFL), electrolyte and cathode were screen printed. The AFL next to the anode substrate had 57 wt% of NiO in order to provide good electronic conductivity and thermal expansion match, while the AFL adjacent to the electrolyte had a lower NiO percentage in order to decrease the amount of oxidation induced volume expansion. Moreover, they produced cells with an oxidation barrier having high NiO content on the fuel side of the anode substrate, so that upon re-oxidation the NiO expansion reduces the barrier porosity and as consequence lowers the Oxygen diffusion rate into the anode, and increases the amount of time needed to reach a certain redox depth. Both these modifications increased redox tolerance as demonstrated by the reduction of cell voltage degradation after repeated redox cycles [66].

When the microstructure of the anode is modified by increasing the porosity, a decrease on mechanical strength occurs. In fact, Radovic and Lara-Curzio studied the mechanical properties of unreduced (NiO-YSZ) and reduced (Ni-YSZ) anodes as function

of porosity. They found that Young's and shear moduli and fracture toughness of both, unreduced and reduced anode materials decrease with porosity. This decrease after reduction can be mostly related to the increase in porosity of the samples. Moreover, the authors also observed that fracture toughness of the anode samples increases after reduction in Hydrogen, despite the significant increase in porosity upon reduction ascribing this behaviour to the formation of a ductile Ni-metal phase during hydrogen reduction [82, 83].

Modification of kinetic of reaction

Tietz et al. performed a study on the influence of some extrinsic parameters such as temperature, incident gas flow rate and direction and time of oxidation, on the re-oxidation behaviour of a cell without changing the properties of the cell (porosity, microstructure, thickness of the anode, NiO/YSZ ratio, particle size distribution, specimen shape). They demonstrated that the re-oxidation behaviour strongly depends on degree of oxidation (DoO: defined as the ratio between the amount of Oxygen absorbed by the substrate and the maximum amount of Oxygen the substrate would have been able to absorb upon complete oxidation) and homogeneity of oxidation. These two factors are controlled by several extrinsic parameters. The redox stability of cells is therefore strongly influenced and determined by the mentioned extrinsic parameters. Thus, selection of appropriate configurations in system operation can help to significantly improve the redox stability of the cells [72].

As previously explained, in the anode the reducing atmosphere reduces NiO to Ni and keeps the Ni in the metallic state. An undesired switch to an oxidizing atmosphere allows the Nickel re-oxidation:

$$Ni + \frac{1}{2}O_2 \rightarrow NiO \tag{1.15}$$

Gas diffusion kinetic into anodic matrix and the rate of Ni re-oxidation are important parameters of this reaction. The study of the redox reaction mechanism and the identification of the rate determining step make the control of the oxidation kinetic a promising strategy to increase cells redox tolerance, in order to prevent sudden Ni oxidation.

Tikekar and collaborators studied the kinetic of reduction and oxidation of dense Ni/YSZ cermets with or without oxides additives (CaO, MgO, TiO_2). They observed that reduction kinetic is linear with respect to the time (interface controlled) and increases with the temperature. On the other hand oxidation kinetic is essentially independent of temperature and controlled by diffusion. The use of additives starts from the consideration that small oxide inclusions in metals suppress diffusion phenomena. Thus it is expected that these additives may enhance the Ni stability by suppressing its diffusion kinetic through the YSZ network. Indeed the authors obtained that the dense anode doped with 4 mol% of one of the additives showed a decrease in both reduction and oxidation rate with respect to the undoped anode. All these metal oxides decrease the oxidation kinetic and the Ni mobility so that the coarsening of Ni is inhibited. Thus the use of specific oxide as dopant appears a possible strategy to increase the redox tolerance of Ni-based anodes [84].

The analysis of redox kinetics of Ni/YSZ anodes studied by several researchers via thermogravimetric analysis (TGA) and/or by dilatometry on bulk samples is an effective method to correlate redox degradation to microstructure modifications [85-87].

Fouquet et al. studied the kinetic of oxidation and reduction of NiO powders and of Ni/YSZ bulk ceramics. They observed that the reduction kinetics of bulk ceramics show an inhibited transport process due to the presence of YSZ and therefore their reduction rate is lower than that of NiO powders. On the other hand, the oxidation of bulk ceramics is completed in a shorter period of time in comparison to the Ni powder samples [85].

Waldbillig et al. confirmed that the reduction of NiO/YSZ cermets follows a linear kinetic with an activation energy of 78 kJ/mol and that the re-oxidation follows a parabolic kinetic at low temperatures and for limited mass change. On the other side, they observed that the re-oxidation kinetic deviates from parabolic model at higher temperatures (700-

850°C). Waldbillig et al. underlined that many different oxidation activation energy values can be found in literature due to the high sensitivity of NiO oxidation kinetic to preparation procedures, powder size and impurity levels.

They performed their redox study on two types of specimens: coarse and fine microstructure respectively, the latter being similar to the AFL. The two samples showed a different behaviour upon re-oxidation, since the one having fine microstructure showed many cracks due to the small pores which cannot allocate the NiO expansion. They confirmed that, in a cell, anode with a dense microstructure typical of AFL may lead to electrolyte delamination or cracks formation upon re-oxidation [88].

Moreover, different research groups stated that the properties of fuel cells, such as mechanical and electrochemical performances, long term stability, sintering behaviour and final microstructure, can be effectively modified by the tailored use of selected doping elements that can be added in small quantities to the anode and/or the electrolyte [36, 38, 39, 89, 90]. Dopants such as Cr_2O_3, MgO, CeO_2 were also added to the anode in an attempt to increase the resistance to redox cycles [86, 91].

Undoped and doped samples made by NiO with Al_2O_3, MgO or CeO_2 were studied by Pihlatie et al. by dilatometry and thermogravimetry. They confirmed that porosity is a major microstructural parameter related to the dimensional and structural stability during redox cycling. They measured the cumulative redox strain (CRS), that is the samples elongation during repeated redox cycles with respect to its as sintered length, observing that after three isothermal redox cycles at 850°C it increases by a factor of more than 20 when the as-sintered porosity of the composites decreases from 34 to 9%. They also observed that the dopants affect the as-sintered porosity of the anode and concluded that the use of dopants is a potential way of tailoring cermets microstructure and improving the redox stability [86].

1.6 PRODUCTION OF ANODE SUPPORTED SOFC BY TAPE CASTING

In the present research work the samples were prepared by using water based tape casting, so a brief general introduction on this production method will follow.

Tape casting is the most significant process to produce large area, thin and flat ceramic or metal substrates and multilayer electronic devices [92]. This technique is easy and cheap. The thin ceramic sheets are essentially two dimension structures since the thickness (from 5-1000 μm) is smaller than the other two dimensions.

Tape casting is usually based upon non-aqueous solvents but in recent years there have been a successful increase in the use of aqueous based tape casting process [93]. Water has the advantage to be a cheap and environmental friendly solvent.

The process appears very simple: homogeneous slurry is introduced into the reservoir of the doctor blade apparatus (Fig. 1.9) and cast onto a rigid substrate and then let dry.

The movement between the doctor blade and the substrate can be obtained by moving either the carrier film (stationary blade) or the reservoir itself (moving blade). The doctor blade gap, i.e. the distance of the blades from the substrate, fixes the height of the cast slurry (and consequently of the dry tape) and can be adjusted by acting on the micrometers. The green obtained tape is flexible and deformable and can therefore be cut, punched or wrapped very easily.

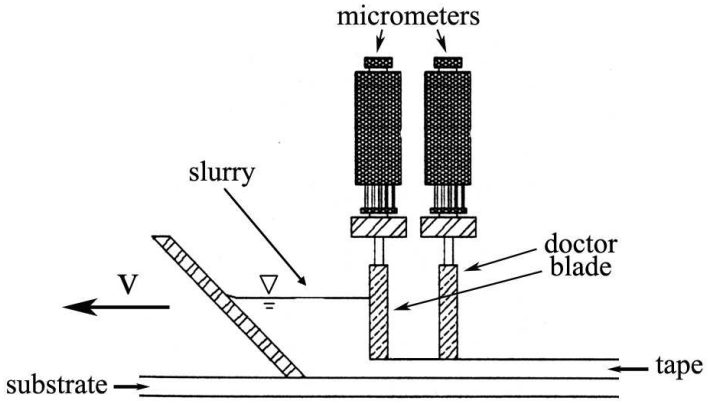

Fig. 1.9: The basic principle of the tape casting process.

In order to obtain a homogenous and free of defect green tape it is important to prepare a well-dispersed slurry. The slurry is a suspension obtained by thoroughly mixing ceramic powders, solvent, dispersants and binders.

Dispersants are low molecular weight polymers stable to the milling attrition added to stabilize the suspension by separating the particles, in order to obtain a homogenous suspension.

Depending on the molecular structure, dispersants are adsorbed onto the particles surface and avoid their agglomeration by steric hindrance and/or ionic repulsion (Fig. 1.10).

The optimal amount of dispersant depends on the particles specific surface area and can be determined when the suspension shows the minimum viscosity or maximum packing ability in sedimentation tests. Typical dispersants are Sodium silicate, menhaden fish oil, stearic acid, salts of polyacrylic or methacrylic acid, polyethylene glycol and pH adjustment.

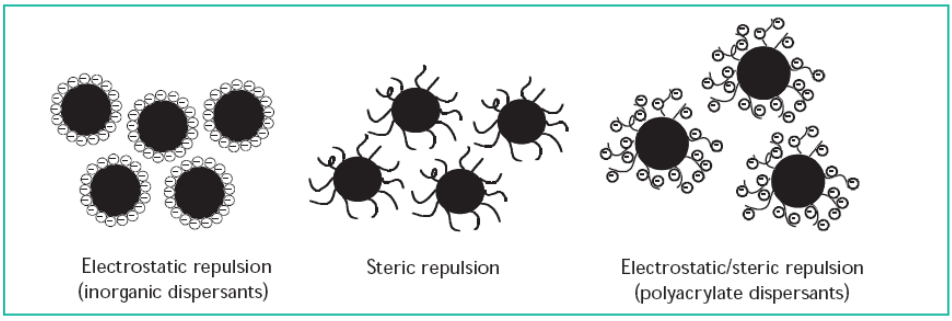

Fig. 1.10: Different type of repulsion realized by dispersants.

Binders are high molecular weight polymers that determine the green tape mechanical properties such as strength, flexibility, plasticity and smoothness. They constitute a solid network in which the ceramic powder is entrapped. Binders commonly used are vinyl (PVA, PVB), acrylic (PEMA, PMMA), polyolefin and cellulose based.

Many parameters determine the tape height and homogeneity: temperature, blade gaps and carrier speed, slurry height in the reservoir, and slurry viscosity. The relation between these parameters and the final tape height is very complex and up to now the proposed mathematical models are not completely reliable.

Viscosity is very important to obtain a tape with constant thickness, so the slurry should show a pseudoplastic behaviour. In this case the high shear stress exerted on the slurry below the blade reduces its viscosity and favours the flow rate, while viscosity increases downstream from the doctor blade so that the cast tape is stable and do not spread laterally [94].

SECTION 2

GENERAL CONSIDERATIONS

Different approaches can be pursued in order to produce redox resistant cells.

Tailoring the cermet microstructure by increasing the porosity with the aim to facilitate free Ni expansion upon re-oxidation seems to be a promising route. To obtain such result it is possible to add within the anode microstructure different kind of fugitive materials. The addition of a pore former into the anode has different objectives such as provide a supplementary porosity and improve the access to the active three phase boundary regions of the anode increasing as consequence the conductivity and the performance of the cells. Nevertheless, it is necessary to take in account that ASCs must show sufficient mechanical strength, and a compromise between these two characteristics is foreseen. Many other strategies can be adopted to improve redox tolerance:

- Acting on redox kinetic, i.e. control the oxidation kinetic in order to reduce the Ni reaction rate with Oxygen.
- Increase the wettability between Ni and YSZ network with the purpose of avoid the Ni particles migration and coarsening in reducing environment.
- Increasing the mechanical resistance of YSZ network, and as consequence of the anode, in order to contrast the internal stresses produced during Ni re-oxidation.
- Adding appropriate dopant oxides could be considered a useful technique with the intention of achieve the previous objectives.

A further possible and interesting method to achieve redox tolerance is the tailoring of the microstructure by using combinations of anodic powders with different shape and granulometry. This method seems a promising and viable route to enhance both the porosity and mechanical strength of the cells.

During the present research work, all such approaches have been considered with the intention of realize redox tolerant cells. Different kinds of investigation have been taken in account in order to evaluate their redox tolerance. The obtained results, the specimens production procedure and their characterizations are presented in this section.

The experimental part is divided into four chapters. In the first chapter the attention is focused on a description of the general methods used for the production of the specimens; moreover, the apparatus used for the analysis and the characterization of the samples are reported. In addition, the test conditions used for each investigation developed are described.

In the second chapter, the modifications realized into the anodic microstructure by adding pyrolizable materials in order to increase the microstructure porosity and obtain redox tolerant cells are reported. This chapter is divided in different parts where the effects of different pore formers are analyzed. For each of them, the experimental procedures are described and the obtained results are reported.

In the third chapter, the modifications of the anode microstructure by using powders with different morphology are considered as a way to increase porosity and enhance mechanical resistance and redox tolerance. For this reason ceramic powders of customised size and aspect ratio (different from the NiO-YSZ powders) were added to the usual anodic powders. The redox behaviour of these specimens was investigated and related results reported.

The last chapter deals with the use of dopant elements added to the anodic composition in order to modify the redox behaviour. The addition of the dopant agents has the purpose to produce redox tolerant anodes, with high electrochemical and mechanical performance. This chapter is divided into different parts according to the kind of analyses realised to study the redox behaviour.

CHAPTER 2

EXPERIMENTAL PROCEDURE

MATERIALS, PRODUCTION AND INVESTIGATION METHODS

In this chapter a brief description of the general techniques used for the samples production and of the apparatus used for the analysis are reported. Moreover, the test conditions used for each investigation carried on are described.

2.1 TAPE CASTING TECHNOLOGY FOR ANODE AND ELECTROLYTE PRODUCTION

Thin and flat ceramic sheets were produced by water-based tape casting technology. Ceramics powders typically used in this work are:

- 8 mol% yttria stabilised zirconia (8YSZ, Tosoh, Japan) for the electrolyte;
- 58 wt% NiO powder (J. T. Baker, USA) mixed with 42 wt% 8YSZ for the anode.

Ceramic powders were dispersed in a plastic drum with a solution of deionised water and an organic dispersant, specifically an ammonium polyacrylate dispersant (Darvan 821A, R.T. Vanderbilt Inc., USA). Zirconia balls (Inframat Advanced Materials) were introduced into the plastic jar in order to disrupt powder aggregates.

The electrolyte slurry was, mixed for 3 h using a high efficiency mixer (Turbula T2F, Bachofen, Switzerland). The anodic slurries were mixed for 18-20 h in a conventional rotating jar mill.

Then, the slurries were filtered to 50 μm to eliminate the possible agglomerates and the zirconia spheres. The air bubbles present in the slurry were removed by de-gassing the suspension for 20 min by using a vacuum Venturi pump. Acrylic emulsions, B1000 (Duramax, Rohm and Haas, France) as binder, and B1014 (Duramax, Rohm and Haas, France) as plasticizer were added; the mixtures were slowly stirred for 2 h. The slips were delivered to the dual doctor blade reservoir (DDB-1-6, 6 in wide, R.E. Mistler, Inc., USA) and cast on a composite three–layer film, PET12/A17/LDPE60 (BP Europack, Italy), in

order to make the removal of the dried green tape simple. The casting speed was fixed at 1 m/min. For the electrolyte suspension, the gaps of front and rear blades were 30 and 50 µm respectively; these gaps were set to 700 and 800 µm for anodic slurries casting. It was possible to obtain half cells by casting sequentially the thick anode suspension on the top of the dry electrolyte tape. The relative humidity of the over-standing environment was controlled and set at about 80% during casting and drying phases, in order to avoid fast evaporation of the solvent and consequent possible cracking of the green layers due to shrinkage stresses. A schematic illustration of the process used for the preparation of the half cells is reported in figure 2.1. The green dry tape was punched or cut in different shapes and then sintered at 1450°C for 2 h.

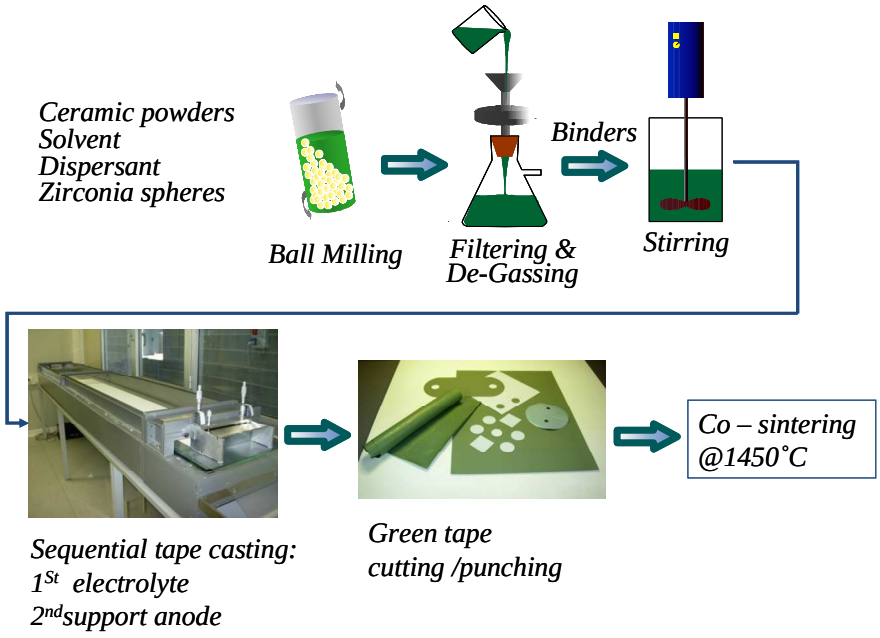

Fig. 2.1: Schematic process of samples production by tape casting technology.

2.2 SCREEN PRINTING TECHNOLOGY FOR CATHODE PRODUCTION

Screen printing is a coating technique that uses a woven mesh to support an ink-blocking stencil. Coated area shape and extension are tailored by using different stencils. The ink is typically a thick paste which is forced through the mesh by using a squeegee onto the surface to be coated. A sketch of the screen printing apparatus is reported in figure 2.2.

Many parameters control the process, such as: screen (e.g. mesh size, fabric material and filament diameter), squeegee (e.g. material hardness, speed and pressure), ink (e.g. composition and rheology) and substrate characteristics (planarity, roughness and materials). Inks are obtained by mixing powder with a high boiling point solvent and an organic binder; some time other substances are added such as lubricants or sintering aids. Mesh size and filament diameter are chosen by taking in account the paste rheology, the surface roughness and the desired coated layer thickness. Typical printed paste thickness ranges from 60 to 80 μm while after drying the resulting layer is 20-30 μm [95].

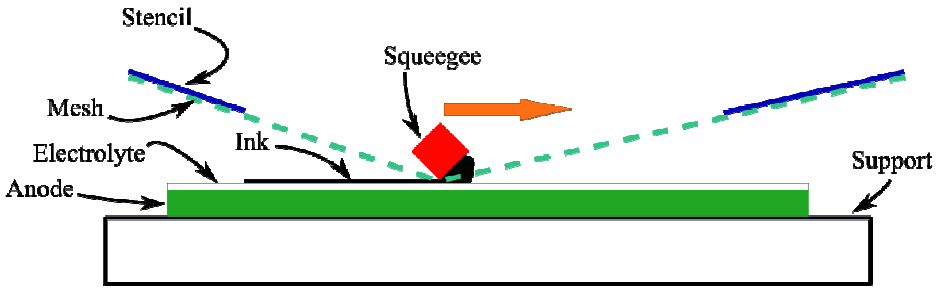

Fig. 2.2: Screen printing sketch for the application of the cathode upon the thin electrolyte.

Screen printing technology was used for the application of the cathode over the sintered electrolyte of the samples produced during the PhD work.
In detail, cathode interlayer was preliminarily deposited by using a mixture of LSM (Nextech, USA) and YSZ (Nextech, USA) powders suspension with 50/50 weight ratio; the LSM cathode contact layer was then screen printed over the interlayer. Both the pastes were prepared by dispersing the powders into a mixture of terpineol and ethylcellulose. Once the layers were dried the cells were sintered for 2 h at 1150°C.

2.3 THERMOGRAVIMETRIC ANALYSIS

Thermogravimetric analyses (DTA – STA 409 PC Luxx, Netzsch) were performed to investigate mass changes during oxidation and reduction cycles and the kinetic of redox cycling. Redox cycles were carried out under isothermal state at the temperature of 800°C in order to have condition similar to the real operation of the cells. The test consisted of the following steps:

- (a) heating to 800°C at a rate of 20°C/min in air (100 ml/min),
- (b) reduction for 3 h in 5 % H_2 and 95% Ar (100 ml/min),
- (c) oxidation for 3 h in air (100 ml/min),
- (d) repetition of step (b) and (c),
- (e) cooling to room temperature in air at a rate of 20°C/min.

2.4 REDOX TESTS

In order to study microstructure changes upon reduction and oxidation, anodes and half cells were used for redox cycling tests. These tests were carried out in a tubular furnace according to the following steps process:

1) heating to 800°C at 5°C/min under N_2
2) reduction in 10% H_2-N_2 atmosphere for 1 h;
3) reduction in pure H_2 for 2 h;
4) purge of the furnace chamber by using pure N_2 (100ml/min) for 15 min;
5) oxidation in air for 3 h
6) purge step and repetition from the 2nd to the 6th step;
7) cooling at room temperature.

After reduction and re-oxidation the samples microstructure was studied and the porosity was measured.

2.5 ELECTROCHEMICAL TESTS

Tests benches developed by SOFCpower Srl for single cells configuration were used for cells electrochemical characterization.

Cells were tested at 800°C in order to compare the electrochemical performances and redox cycling tolerance. Electrochemical performances of the cells before and after redox cycles were determined in order to evaluate open circuit voltage (OCV) recovery after each cycle and performance losses due to microstructure modifications.

The cells were mounted in the furnace as shown in figure 2.3. The cells were sealed, with a high temperature sealant, on the top of an alumina tube in correspondence of a 14 x

14 mm^2 window fixed over an alumina mask thus ensuring an active area of about 2 cm^2. The electrodes were fed through two narrow alumina tubes having a square alumina sponge on the side in contact with the electrodes. Current collection was assured by a Nickel mesh for the anodic compartment and by a Gold mesh for the cathodic compartment. The cells were heated up to 800°C with a rate of 1°C/min.

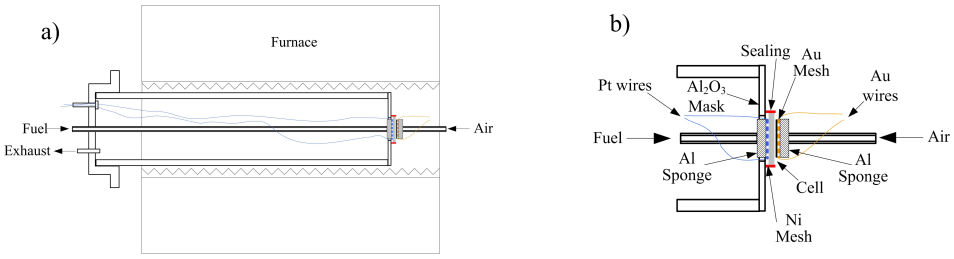

Fig. 2.3: Electrochemical test set-up. a) Furnace and piping; b) particular of electrical connections and gas feeding system.

The reduction of the anode occurred in an atmosphere H_2/N_2 with a ratio of 10/90 for 1 h, then the cells were fed with 150 ml/min of H_2 humidified at 3% at the anodic compartment and with 300 ml/min of air at the cathodic side; after 1 h I-V measurements were carried out. Afterwards, redox cycles were performed. At the anodic compartment different flows were fed:

(a) Purge step in N_2 (100 ml/min) for 15 min;

(b) Re-oxidation in air (100 ml/min) for 2 h;

(c) Purge step in N_2;

(d) Re-reduction in H_2/N_2 10/90 (1 h) and pure H_2 (1 h) atmosphere; repetition from the step (a);

(e) Cooling at room temperature.

Labview software was used to control the data acquisition process.

2.6 ELECTRICAL IMPEDANCE SPECTROSCOPY (EIS)

AC electrical impedance spectroscopy is a powerful method for performance evaluation and degradation diagnostic of fuel cells. This technique is based on the measurement of the complex impedance $Z(\omega) = Z_{re} + jZ_{im}$ in function of the frequency ω of a voltage or current signal. The frequency usually varies from low values, few mHz, to hundreds of kHz. The utility of this method consists in the possibility to monitor the different relaxation times and relaxation amplitudes of the various processes present in a dynamic system over a wide range of frequencies. Specifically in the SOFCs each electrical, electrochemical, chemical and mass transport process is characterised by a typical time constant; so the response of each process depends on the solicitation frequencies.

Considering that in a SOFC the different processes have a time constant that can differ of many orders of magnitude, it is possible to identify them by varying the frequency. Moreover, it is possible to associate to each single process an equivalent electrical circuit that is constituted in the simplest case by a resistor R and a capacitor C in parallel [96]. So a fuel cell can be modelled by a more complex series of these elements. The impedance can be plotted in different ways; the most used are the Nyquist diagram where the imaginary part of the impedance is plotted vs. the real part, and the Bode plot where $\log(Z_{re})$ or $\log(Z_{im})$ are plotted vs. $\log(\omega)$. For instance the impedance of a circuit constituted by a resistance and a capacitor in parallel is:

$$Z = \frac{R}{1 + J\omega RC} = \frac{R}{1 + \left(\omega^2 R^2 C^2\right)} - J\frac{\omega R^2 C}{1 + \left(\omega^2 R^2 C^2\right)} \qquad (2.1)$$

that in Nyquist diagram is represented by a semicircle having R as diameter (Fig. 2.4a). This circuit is characterized by a relaxation frequency ω_R that is the frequency at which the imaginary part of the impedance is maximum:

$$\omega_R = \frac{1}{RC} \tag{2.2}$$

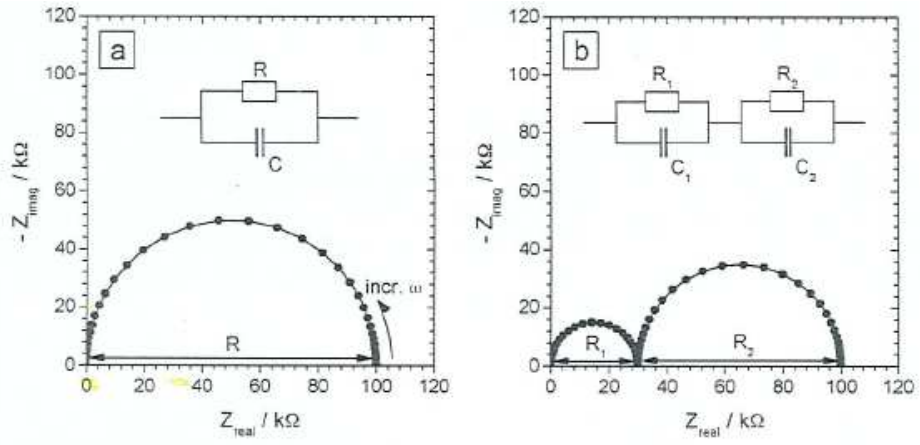

Fig. 2.4: Nyquist plot examples: RC circuit in parallel (a), and two RC circuit in series (b) [97].

In the case of two circuits in series having quite different relaxation frequencies, the representation in Nyquist diagram is constituted by two different semicircles as evidenced in figure 2.4(b) [97].

The degree of complexity in a real fuel cell is high due to the presence of processes with similar time constants. The correspondent Nyquist diagram is the sum of many semicircles partially or completely overlapped resulting in a single distorted arc. Despite of the difficulty on its interpretation, EIS is very useful for understanding the cell behaviour; indeed the response time for ohmic polarisation is essentially zero, while the time constant

for concentration polarisation is related to the relevant gas phase transport parameters such as diffusivity [10].

AC electrical impedance spectroscopy analysis was carried out for some specimens. The Autolab Potentiostat/Galvanostat module PGSTAT302N supported in GPES (General Purpose Electrochemical System) and FRA (Frequency Response Analyser) was used to control the data acquisition process.
The test were performed at 800°C in potentiostatic condition and EIS were measured at OCV and at 0.5 A/cm^2 with frequency ranging from 0.1 to 50000 Hz.

2.7 CURVATURE ANALYSIS UPON REDOX CYCLES

It is possible to study the redox behaviour of cells also by the analysis of the deformation of the unconstrained half cell during the oxidising and reducing atmospheres.
The curvature evolution upon redox cycles was analyzed in situ by a charge-coupled device (CCD) camera acquiring pictures at regular intervals (30 s) through a series of optical filters [98]. The length of the bi-layers and the curvature developed upon the redox cycle were measured from photographs with the freeware software ImageJ 1.38 J.

The sintered specimens were laser cut into 20 mm length and 3 mm width strips. A specific alumina sample holder was built to allocate the specimens. The samples were situated with the anode placed on the holder (electrolyte upside). A design of the apparatus and of the sample holder is reported in figure 2.5.

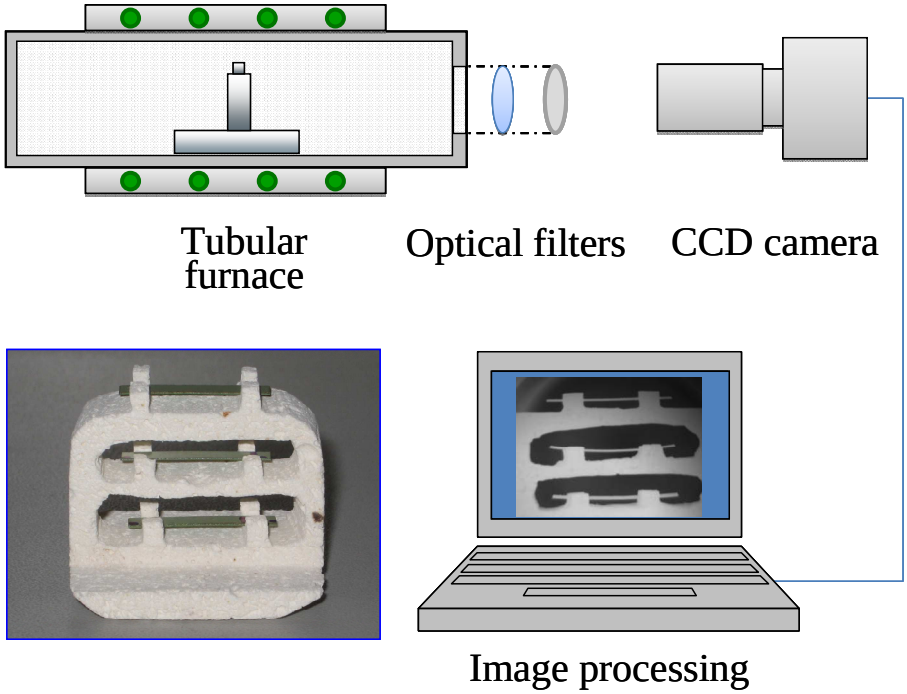

Fig. 2.5: Illustration of the set-up for curvature study during redox cycle and of sample holder.

The redox cycle was performed at 800°C in an alumina tubular furnace, under the following conditions:

(a) heating to 800°C at 5°C/min under N_2 (100 ml/min),

(b) reduction: 70 min in 3% humidified H_2 (100 ml/min),

(c) purge: 15 min in N_2 (100 ml/min),

(d) oxidation: 70 min in air (100 ml/min),

(e) cooling at room temperature.

2.8 BIAXIAL FLEXURE ANALYSIS

Fracture strength is one of the most important properties for characterization of ceramics mechanical properties, as it is a basis for the selection of the materials for a target application and to determine the reliability of a material during its lifetime. Many test configurations have been proposed in order to measure the material strength; most of them associate the fracture strength to the maximum strength at fracture. Thus, the stress distribution has to be known so that fracture strength can be determined for any particular load and specimen's geometry. As a matter of fact the strength of ceramic materials is quite sensitive to size, shape and surface finish; these parameters affect the high dispersion of the strength values for a given material. A viable test methodology must take in account the effect of these parameters in order to minimize their influence.

Uniaxial loading methods such as three and four point bending tests are very commonly applied to the ceramic strength investigation. However biaxial loading techniques result useful in testing real ceramic components because they apply to the specimen a more severe stress state than uniaxial methods. Moreover, by considering that in brittle materials fracture often originates at an edge or surface, specimens preparation can dramatically affect the strength measurements. Uniaxial tests are highly sensitive to the finishing of the specimen's surface. The biaxial tests are less sensitive to surface defects because they accounts for flaws regardless of direction and the stresses are almost zero along the sample's periphery. Therefore biaxial techniques have to be preferred if the intrinsic material strength is addressed [99].

As well as in all experimental techniques also biaxial flexure one is affected by errors. These errors depend by the test configuration but two of them are common to all the biaxial flexure techniques. A specimen subjected to biaxial flexure develops a steep stress gradient being compressed uniaxially and perpendicularly on one face centre, while the opposite face is subjected to equibiaxial tension. This gradient affects the polycrystalline

ceramic mechanism of fracture: it is transgranular for large grained materials and intergranular for finely grained materials. Moreover, the stress equations developed to calculate the fracture maximum stress are based on the hypotheses of isotropic and homogeneous materials and that the central deflection of the specimen is small. In order to decrease the stress gradient, disks with thickness smaller than the 20% of the support radius and with a central deflection lower than half of the thickness are used.

Ring on ring configuration consists in two concentric rings, one is the support where the disk is placed and the second is the load ring that is contact with the upper surface of the specimen and bears the load as shown in figure 2.6. This configuration presents some disadvantages: the absence of perfect contact between loading rings and sample can lead to substantial deviation from radial symmetry in the stress field and errors in the strength determination. This contact defects imply a stress concentration in limited areas of the disk; moreover, friction and wedging effects can affect the measurements reliability. From these considerations, a perfect parallelism between the two rings is required.

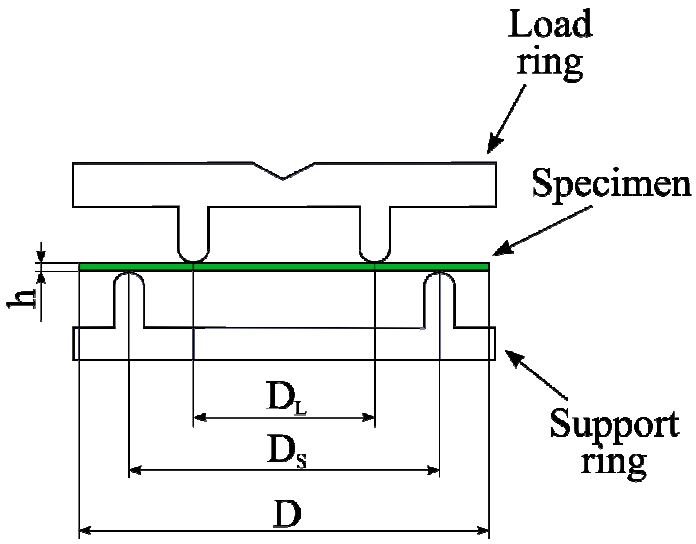

Fig. 2.6: Ring on ring fixture

In spite of these drawbacks the advantage of ring on ring in comparison with the other biaxial flexure fixtures resides in the fact that the stress is almost constant within the load ring area. This allows to determine the strength of the samples without uncertainties if the fracture starts inside the load ring.

Equibiaxial flexural strength (σ) via concentric ring on ring configuration under monotonic uniaxial loading can be estimated as:

$$\sigma = \frac{3F}{2\pi h^2}\left[(1-\nu)\frac{D_S^2 - D_L^2}{2D^2} + (1+\nu)\ln\left(\frac{D_S}{D_L}\right)\right] \tag{2.3}$$

where:

F is the breaking load

h is the test specimen thickness

ν is the Poisson's ratio

D_S and D_L are the support and load ring diameters respectively

D is the test specimen diameter.

In order to evaluate the scattering of strength data for ceramic materials, Weibull distribution is the most used statistic method. The Weibull distribution calculates the failure probability assuming that the failure is determined by the most critical defect according to the weakest link theory. The failure probability P_f at a given stress level σ can be estimated by the following relation:

$$P_f = 1 - \exp\left[-\left(\frac{\sigma}{\sigma_0}\right)^m\right] \tag{2.4}$$

where:

σ_0 and m are the Weibull characteristic strength and modulus respectively. The latter parameter is particularly useful because give a straight estimation of strength variability: the higher is the modulus the smaller is the strength variability.

In Weibull analysis the experimental results, i.e. fracture strengths, are ranked in ascending order and a failure probability is assigned:

$$P_f(\sigma_i) = \frac{i - 0.5}{N} \tag{2.5}$$

where:

N = number of test specimens

i = i-th datum.

Weibull distribution is commonly represented by plotting the experimental data (probability of failure) in a graph with $ln\{ln[1/(1-P_f)]\}$ vs. $ln(\sigma)$.

The Weibull parameters are then calculated by a linear regression.

Ring on ring tests were performed to determine the mechanical strength of the half cells produced during this work according to the ASTM standard C 1499-09 [100].

The fixture used (Fig. 2.6) had a support diameter of 23 mm and a load ring of 10 mm. The tests were performed at room temperature using a displacement rate control of 3 mm/min.

30 circular specimens were tested for the estimation of Weibull parameters. The test was performed on half cell specimens were the electrolyte was in compressive surface, so that the anode surface is located in contact with the support fixture. A Poisson's ratio of 0.25 for all the samples it was assumed.

The ring on ring tests were performed on two kinds of samples: *Alfa* and standard half cells. The previous were produced adding to the usual anode slurry a ceramic powder with

different size and aspect ratio provided by SOFCpower S.r.l. The latter samples were also provided by the company.

2.9 OTHER ANALYSES

In order to gain a deeper insight into the samples modifications upon redox cycling further analyses were performed.

Morphology of the doped powders, microstructure of anodes, of half cells and of the cells produced were analyzed by scanning electron microscope (SEM, JSM 5500, JEOL, Japan).

Anodes porosity was measured by using the Archimede's method.

Specific surface area (SSA) of the doped powders was determined by Nitrogen Adsorption BET method (ASAP 2010, Micromeritics, USA).

RESULTS AND DISCUSSION

CHAPTER 3

ANODES WITH FUGITIVE MATERIALS

3.1 INTRODUCTION

A possible way to enhance redox tolerance is to increase the anode porosity in order to allow the large volume increase of Nickel during re-oxidation, decreasing at the contempt the internal stresses generation and consequent crack formation. An improvement in cells performance can be also expected, considering for instance a decrease in the concentration polarization due to the transport of gaseous species. Different experimental tests were performed at the beginning of this work with the intention to select the fugitive material to add to the anodic slurry.

Pyrolyzable organic particles were chosen as fugitives material considering that no residue has to remain within the anodic microstructure, in order to avoid anode poisoning. From this preliminary screening the following pore formers were selected: polyurethane (PU) foam, Poly(methylmethacrylate) (PMMA) beads, (PEM-co-MMA) poly(ethyl methacrylate-co-methylmethacrylate) beads and graphite flocks. The mean size of the used pore formers decreases from PMMA to PEM-co-MMA to graphite, as it is possible to observe in the micrograph of figure 3.1. Different shapes and dimensions were chosen in order to understand if and how these factors can affect the redox behaviour.

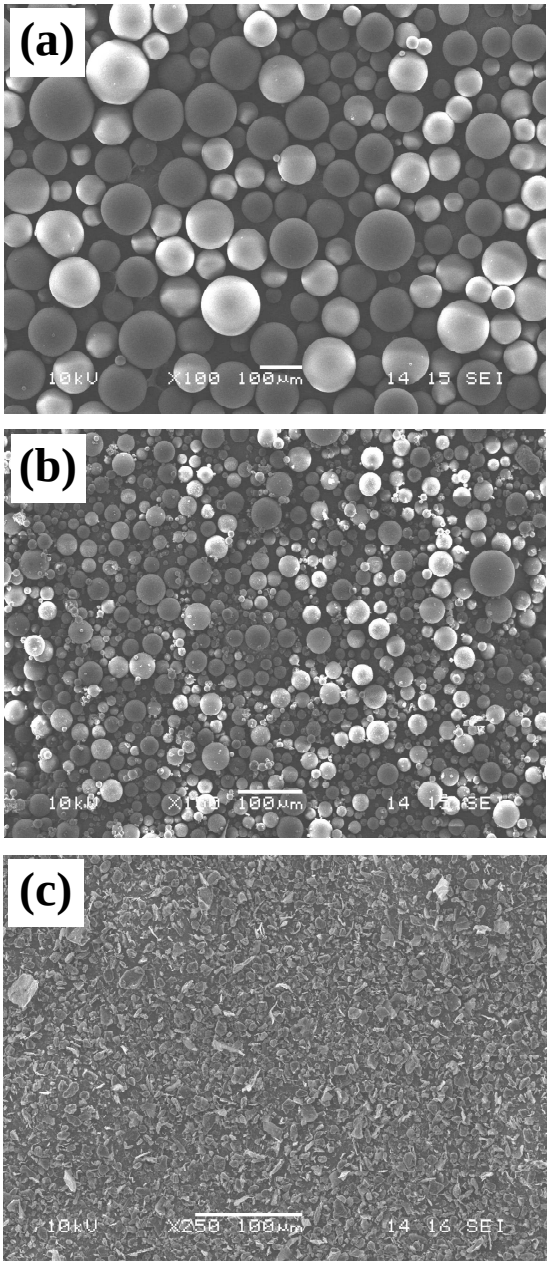

Fig. 3.1: Micrographs of fugitive materials: PMMA (a) and PEM-co-MMA (b) beads and graphite flakes(c).

3.2 PU-FOAM

The first pore former tested was a PU foam. The samples were produced by spraying the foam within the anodic slurry in order to obtain a spongy structure with large open porosity. 9 wt% of PU-foam with respect to 8YSZ/NiO powder was added to the slurry. The starting anodic slurry was produced by the usual procedure explained in the Materials and method chapter; the PU foam was added to the suspension after mechanical stirring of the binders and was mixed manually. The slip was cast with a blade height of 3 mm.

After sintering the microstructure of the anode shows a high open porosity as it is evidenced in the micrographs of figure 3.2. Even if the samples demonstrated elevated open porosity, their brittleness made them not suitable for further analyses and for production of fuel cells.

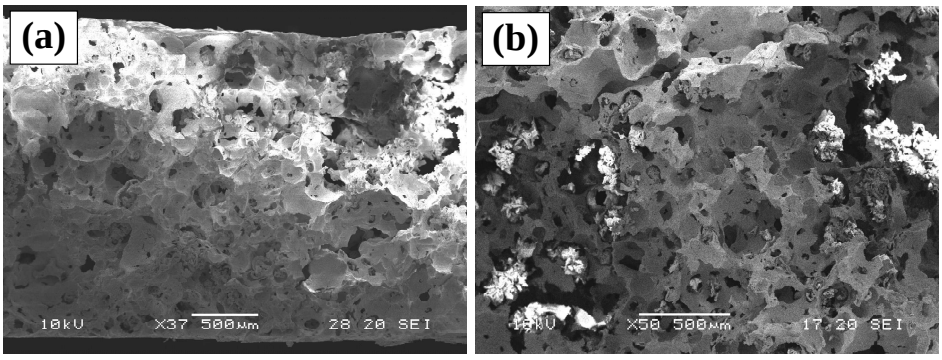

Fig. 3.2: Cross section of anode prepared with addition of PU foam (a) and its magnification (b).

3.3 ANODE AND HALF CELLS WITH PEMA-CO-MMA

3.3.1 INTRODUCTION

In the present paragraph the effect of anode microstructure modifications due to the addition of poly(ethyl methacrylate-co-methyl methacrylate) beads (PEMA-co-MMA) on the anode microstructure was investigated.

3.3.2 EXPERIMENTAL

Anode and electrolyte were prepared by water-based tape casting technology. The electrolyte was fabricated by using 8YSZ powder and the anode was based on 58 wt% NiO powder mixed with 42 wt% 8YSZ. The procedures used to produce the samples are reported in the paragraph of Materials and methods.

Standard (STD) dense anodes and half cells (anode and electrolyte) were obtained. Anodes and half cells with different pore morphology and distribution were also prepared by adding (4 vol%) poly(ethyl methacrylate-co-methyl methacrylate) beads (PEMA-co-MMA) (Scientific Polymer Product inc., USA) as pore former to the NiO/8YSZ slurry. Slurries composition and casting parameters are reported in Table 3.1. After drying, STD and pore former containing anodes (PF) and corresponding half cells were sintered at 1450°C for 2 h.

In order to study microstructure changes upon reduction and oxidation, NiO/YSZ laminates and anode/electrolyte half cells were used for redox cycling tests. Microstructure of the samples after sintering and after redox cycles was analyzed; porosity and specific surface area (SSA) were measured.

Cathode interlayer and contact layer were sequentially screen printed on some half cells to obtain the fuel cells suitable for electrochemical tests.

Table 3.1: Composition of electrolyte and anode slurry (vol%)* and casting parameters.

	Electrolyte	Standard anode (STD)	Anode with pore former (PF)
Powder	28	21	21
Dispersant (Darvan 821A)	2	3	3
Solvent (Water)	58	53	53
Pore former (PEM-co-MMA)	-	-	4
Binder (B1014)	6	18	12
Plasticizer (B1000)	6	5	7
Casting speed (m/min)	1	1	1
Rear blade height (µm)	50	800	800
Front blade height (µm)	40	700	700

*Binder and dispersant contents are reported on dry basis.

Cells with STD and PF anodes were electrochemically tested at 800°C in order to compare the electrochemical performances and redox cycling tolerance.

3.3.3 RESULTS AND DISCUSSION

The diameter of half cells was measured before and after sintering by a micrometer: the calculated shrinkage resulted about 23-24%. The thickness after sintering was 380±20 µm and 13±3 µm for the anodes and the electrolyte, respectively. After sintering the thicknesses of the cathode interlayer and contact layer were observed to be about 15 µm and 60 µm, respectively.

The microstructure of STD and PF anodes are shown in figures 3.3 and 3.4 respectively. Whereas a uniform and interconnected microporosity was obtained in STD

sample, a discontinuous distribution of macropores was observed in the PF anode. Such structure is characterized by isolated and not interconnected spherical or elliptical pores.

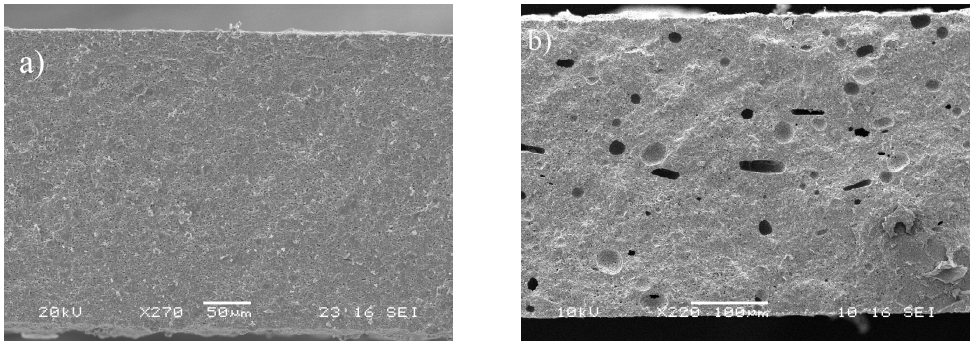

Fig. 3.3: Fracture surface of STD (a) and PF (b) anode after sintering.

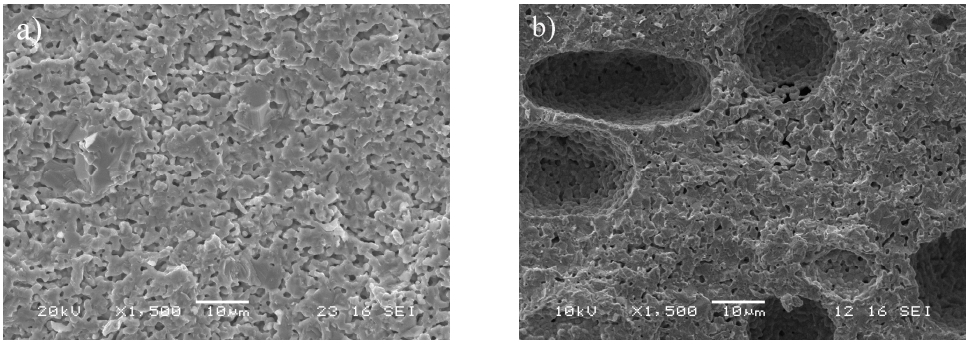

Fig. 3.4: Magnification of STD (a) and PF (b) anode after sintering.

I-V plots of STD and PF cells obtained by electrochemical tests are shown in figure 3.5. The performances appear quite similar and both cells failed after one redox cycle thus exhibiting very low redox resistance.

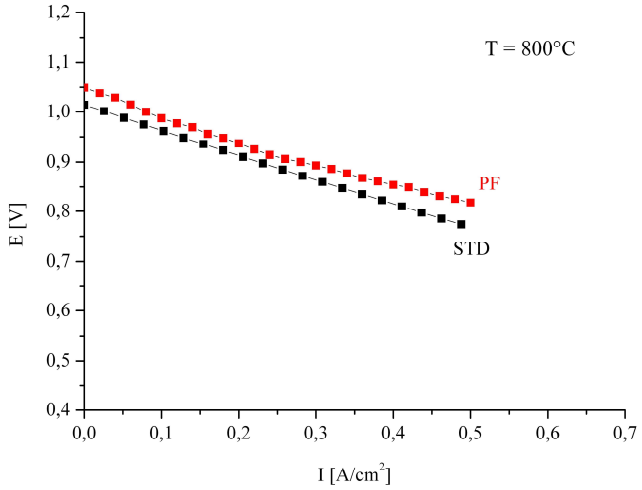

Fig. 3.5: I-V plots of the STD and the with PF cells (one redox cycle).

The amount of organic constituents (B1000, B1014, Darvan and PEMA-co-MMA) in STD and PF slurries is about 26 vol% with respect to the total slurry volume; this explains the same porosity measured for the two sintered anodes (Tab. 3.2). In the reduced state the porosity of PF anode becomes higher than in STD anode as it is possible to observe in Table 3.2.

Table 3.2: Evolution of anode porosity upon redox cycling.

	STD Anode	PF Anode
As Sintered	14	14
After Reduction	25	33
After re-oxidation	13	12

It has to be noticed that the composition of the polymer emulsions used in the slurries for STD and PF anodes was different; indeed, the percentage of pore former, having a larger size than that of the other polymer added to the slurries, was about 15 vol% with respect to the total amount of organic matter responsible for macropores formation (Fig. 3.4b).

In Table 3.3 it is possible to observe that the surface area increases after reduction due to the increase of porosity of the cermet in the reduced state and decreases after successive oxidation.

Pore formers introduction seems to affect microporosity in an unexpected way. It is worth of note that as-sintered STD anodes show higher SSA and more homogenously distributed porosity than PF anodes. This behaviour is probably due to an overall rearrangement of the structure by pore formers introduction that leads to a denser and compact skeleton around big pores. Conversely, the limited fine porosity was maintained in PF samples also after reduction and oxidation steps.

Table 3.3: Specific Surface Area (m^2/g) of the anodes.

Condition	STD anode	PF anode
As sintered	0,25 ± 0,01	0,20 ± 0,01
After 1st reduction	0,45 ± 0,01	0,31 ± 0,01
After 1st oxidation	0,36 ± 0,01	0,27 ± 0,01
After 2nd oxidation	0,35 ± 0,01	0.15 ± 0.01

The microstructure of the anodes after reduction (Fig. 3.6) is noticeably porous when compared with the as sintered anodes. On the other hand, the porosity is strongly reduced by Ni volume increase after re-oxidation.

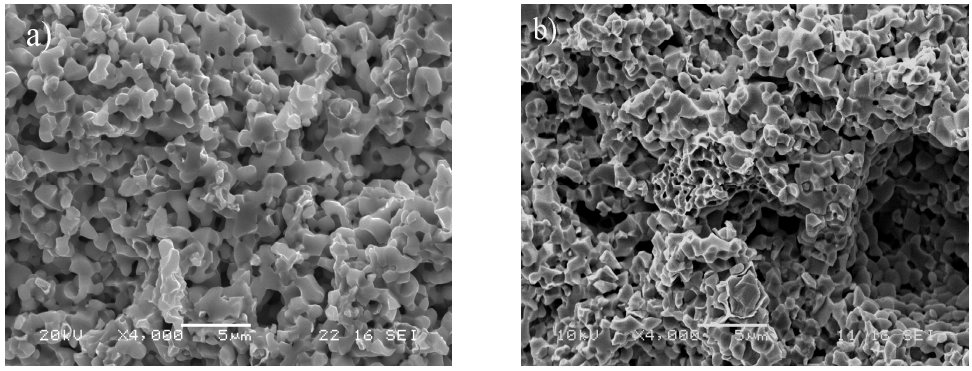

Fig. 3.6: Fracture surface of (a) STD and (b) PF anode after reduction.

Figure 3.7 shows the re-oxidised anode surface microstructure and it is possible to observe the presence of cracks generated by internal stresses and the formation of coarse NiO particles. Therefore it was observed that modifications of the anode microstructure obtained by the addition of low amount of PEMA-co-MMA pore former do not improve redox tolerance. This behaviour can be explained considering that the presence of pore former in the anode may affect NiO distribution. Indeed, the lower SSA of PF anode may leads to a higher NiO concentration per unit of surface that produces locally concentrated internal stresses detrimental for anode integrity.

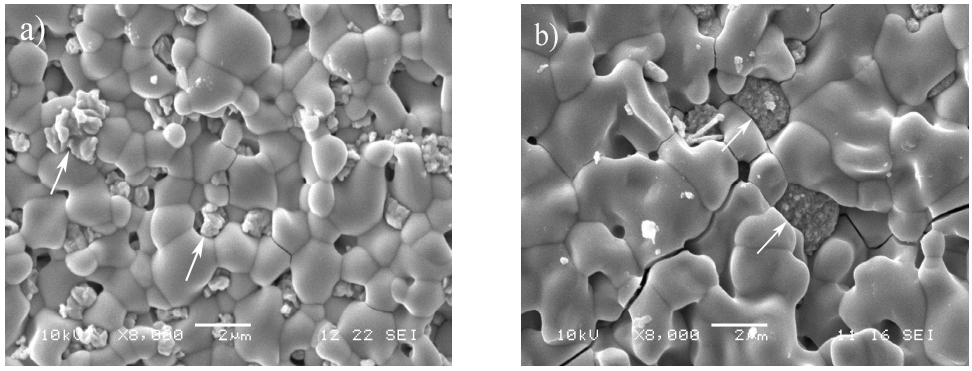

Fig 3.7: STD (a) and PF (b) anode surface after 1st oxidation. NiO particles are indicated by arrows.

The cross section of the standard (STD) and PF anode is reported after one redox test in figures 3.8 and 3.9. In both micrographs it is possible to see the cell failure due to cracks of the electrolyte. In the STD cell it is possible observe a crack trough the electrolyte and the cathode (Fig. 3.8a); figure 3.8b shows a magnification of the STD anode where an intergranular path of crack can be observed, as pointed out by the arrow.

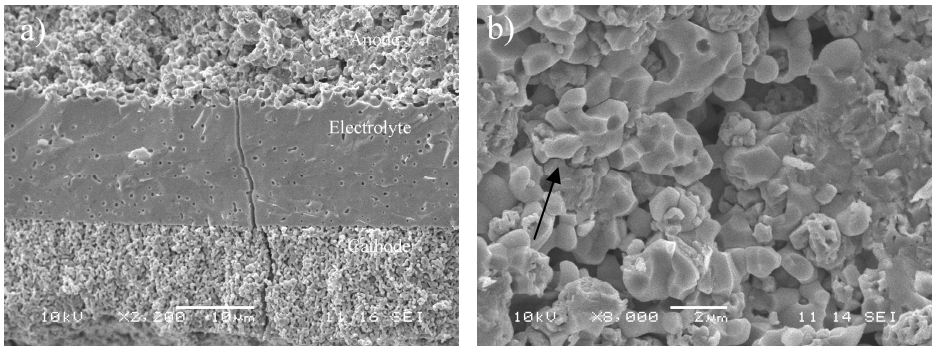

Fig. 3.8: STD cell cross section (a) and anode microstructure magnification (b) after one redox cycle.

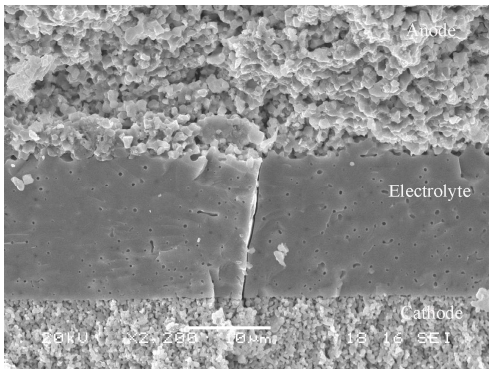

Fig. 3.9: PF cell after one redox cycle.

3.3.4 CONCLUSIONS

Polymeric beads can be added to the slurry for the production of SOFCs anodes with modified microstructure. Nevertheless, standard and pore-former-containing cells are observed to display similar behaviour upon redox cycling if the amount of organic component is the same. It was observed that changes associated to different pore morphology are not sufficient to improve the redox tolerance unless also the porosity is increased. Moreover, the open porosity within the microstructure needs to be well distributed.

3.4 ANODE WITH ADDITION OF PMMA

By considering the result obtained by adding PEM-co-MMA to the anode, the effect of the addition of PMMA pore former with larger particle size on the anode porosity was investigated.

3.4.1 EXPERIMENTAL

Different amounts of pore former were added to the slurry composition ranging from 10 vol% to 40 vol% of PMMA with respect to the powder. Green tapes obtained from the slurries with the higher concentration of fugitive materials showed many cracks. The observed defects could be ascribed to many factors such as the high amount of added pore former and/or the insufficient amount of binder. For instance, considering the anode prepared with 30 vol% PMMA (with respect to the powder) cracks are present in the microstructure of the as sintered tape. Figure 3.10 shows the cross section micrograph of the 30% PMMA sample where it is possible to see an evident crack, highlighted by the arrow. Thus, an optimization of the anodic composition was required and this was achieved by reducing the pore former amount.

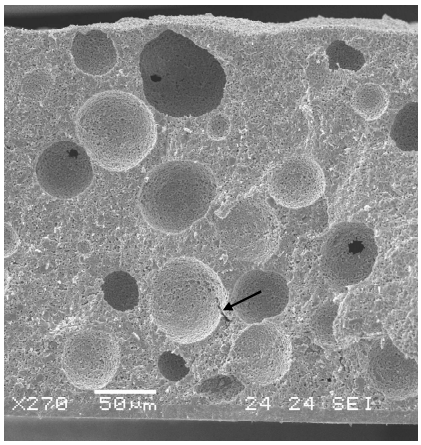

Fig. 3.10: Cross section of anode with 30%vol of PMMA as sintered.

The optimized slurry composition of PMMA containing anode was constituted by 21 vol % of powder, 4 vol% of PMMA, 52 vol% solvent and the total amount of the binders and dispersant (reported on dry basis) was 23 vol%. The resulting sintered anode was crack free and tested to verify the redox cycling resistance.

3.4.2 RESULTS AND DISCUSSION

The samples porosity increases from 20% in the sintered state to 32% in the reduced one as was expected considering that Ni reduction is accompanied by volume decrease. These microstructure changes can be observed in figure 3.11. After one re-oxidation the measured porosity was 15 vol%. Changes in the anodic microstructure due to Ni particles agglomeration and growth during reduction and re-oxidation can explain the different porosity between as sintered and re-oxidated samples. In comparison to PEMA-co-MMA (par. 3.3), the introduction of PMMA within the anodic slurry did not produce any benefit as confirmed by the analysis of the anodic surface after one redox cycle. In fact many inter-

and trans-granular cracks can be observed within the YSZ network (Fig. 3.12) and sponge-like NiO. It is also possible to observe the growth of the Ni particles after re-oxidation caused by the coarsening process.

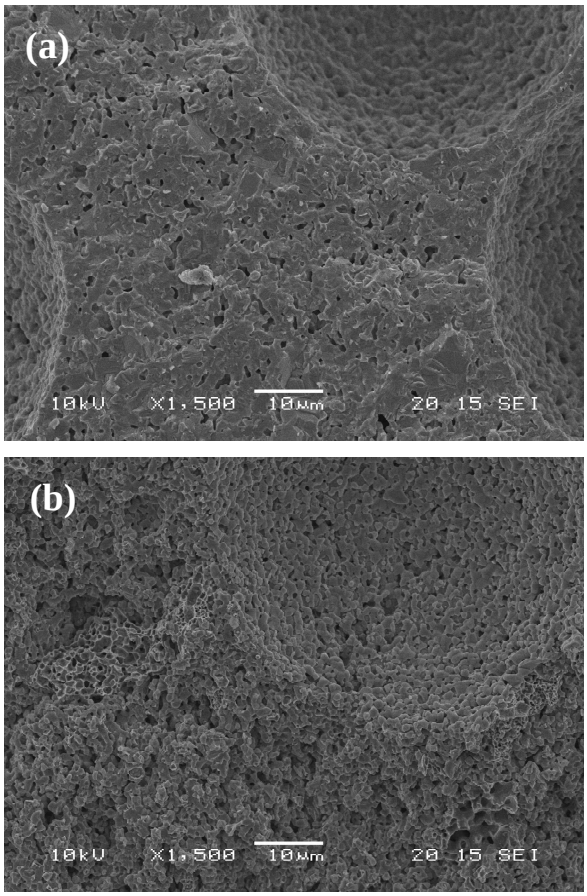

Fig. 3.11: Anodic cross section of as sintered (a) and after reduction (b) anode with PMMA. It is evident the higher porosity in the reduced anode.

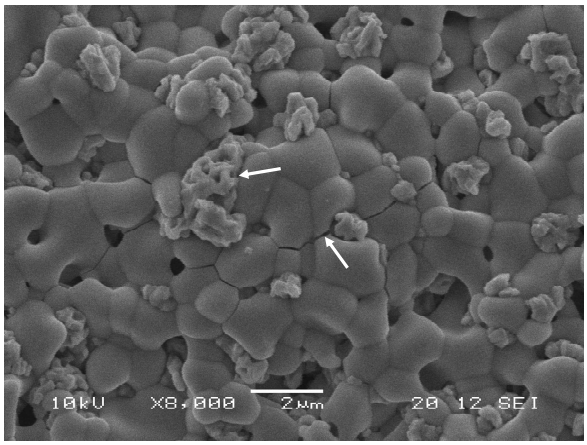

Fig. 3.12: Anodic surface after one redox cycle, cracks and NiO coarsening are underlined by the arrows.

3.4.3 CONCLUSIONS

The results achieved when PMMA beads are introduced within anode slurry confirm the conclusion pointed out from the use of the PEMA-co-MMA as pore former. The amount of pore former within the anodic slurry needs to be higher and must present finer size in order to obtain well distributed porosity. The two tested pore formers present similar morphology and the result obtained are worst even if the anode presents an initial higher porosity.

3.5 ANODE WITH ADDITION OF GRAPHITE

In the present paragraph the addition of graphite flakes (Alfa Aesar) to the anodic slurry as fugitive material is discussed. The choice of this material derives from the results of the previous attempts of anodes production with a tailored porosity. Therefore, in order to obtain an anode with fine, uniform and homogenously distributed porosity, graphite flakes seem to be a suitable pore former.

3.5.1 EXPERIMENTAL

The anodic slurry was prepared by using the procedure reported at the beginning of the chapter. The composition of the anode is reported in Table 3.4. It is worth noting that the amount of fugitive material in terms of powder volume is 1.7 vol%, higher than the amount added within the anode with PEMA-co-MMA.
The total fugitive material is about 57 vol% with respect to the powder and graphite is 8 vol% of the fugitive materials.

Table 3.4: Composition anode slurry (vol%)*.

components	Anode with graphite
powder	20
solvent	54.0
graphite	3.6
dispersant	1.8
B1014	12.6
B1000	8.0

*Binders and dispersant contents are reported on dry basis.

3.5.2 RESULTS AND DISCUSSION

The anode porosity is 21%, 36% and 17% for the samples as-sintered, after reduction and after first re-oxidation, respectively. The porosity of the samples measured after the second re-oxidation is around 16%, and similar values are measured after the first re-oxidation. If compared with the standard and PEMA-co-MMA anodes (Tab. 3.2), it is possible to observe that the porosity of the samples with graphite is always higher.

The fracture surface of as sintered and after reduction anode are reported in figure 3.13. The as sintered anode shows an open and well distributed porosity that increases after reduction (figure 3.13b).

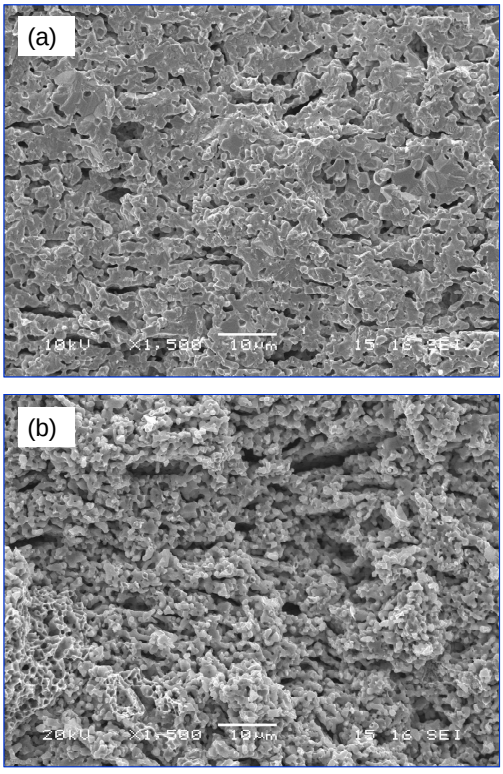

Fig. 3.13: SEM images of the fracture surface of the anode as sintered (a) and after first reduction (b).

The cross section and the surface of the anode after re-oxidation are reported in figure 3.14. After one redox cycle it is possible to identify the anode microstructure modifications (Fig. 3.14a): NiO is not uniformly distributed within the YSZ network as in the as-sintered state; it appears coarse and similar to a sponge, as it is underlined by the ellipse in figure 3.14a and by the arrow in figure 3.14b; its expansion fills more thoroughly the porosity, as confirmed by the lower value obtained by Archimede's measurements. Also the distribution of the porosity appears different with respect to the as sintered state. Indeed, denser areas are clearly visible within the anodic matrix (figure 3.14a). If the porosity is not sufficient to allocate coarse NiO, internal stresses produced by this constrain generate cracks in the YSZ network as indicated by the pointer in figure 3.14b.

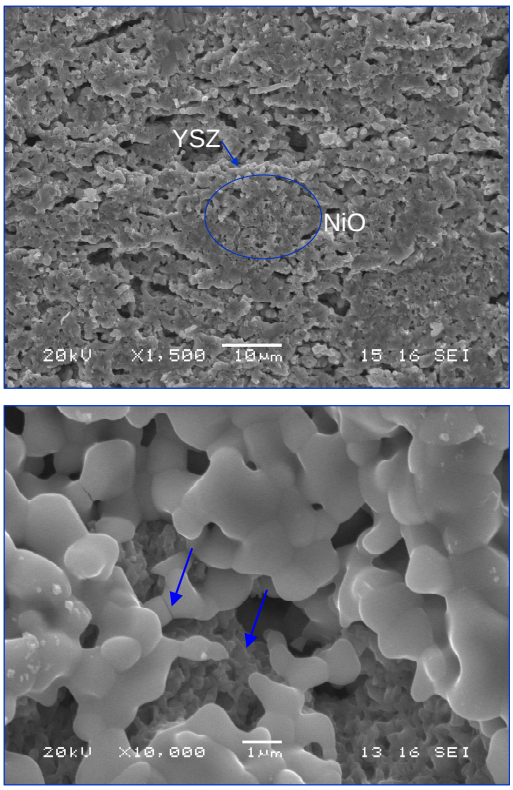

Fig. 3.14: Cross section (a) and surface (b) of the anode after one redox cycle.

Electrochemical measurements were performed on cells with LSM/YSZ cathode and the results are reported in figure 3.15. It was possible to perform six redox cycles before failure. It is evident for each cycle a degradation of the cell. The decrease of OCV is due to the formation of micro-cracks within the electrolyte. Anyway, the trend shows that there is incomplete failure of the cell. From the J-V curve it can be observed that the performance of the cell after each cycle is higher with respect to the cell that did not undergo any re-oxidation, in particular at high current densities; this behaviour can be explained considering that the re-oxidation, if not destructive, can improve, at the beginning, the performance by conditioning the Ni network and enhancing the conductivity, as was stated by Sarantaridis et al. [63].

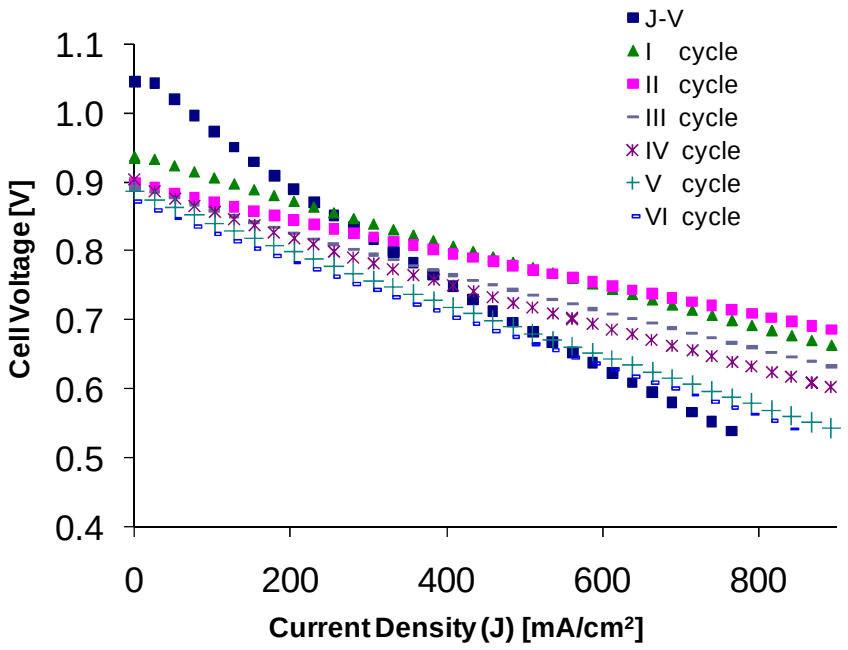

Fig. 3.15: J-V plot for cell produced with addition of graphite into the anode.

J-V curve shows the worst performance but the higher open circuit voltage (OCV) that is 1046 mV while the current density at 0.7 V is 485 mA/cm^2, as shown in Table 3.5.

Table 3.5: OCV and current density at 0.7 V for each cycle.

cycles	OCV (mV)	J (mA/cm^2) @ 0.7 V
I-V	1046	485
I	934	766
II	899	842
III	894	664
IV	903	587
V	887	460
VI	871	434

The OCV values decrease at each cycle confirms the formation of cracks within the electrolyte. At 0.7 V the activation polarization contribution to the total losses is very low and the decreasing in the current density can be ascribed to the ohmic polarization. This means that the cell microstructure changes upon each cycle, and the resistance to the electrons flow through the electrode is increased.

3.5.3 CONCLUSIONS

The addition of finer pore former such as graphite flakes within the anodic microstructure leads to improvements of the redox cycle tolerance even if after the first cycle cracks formation are evidenced by the OCV drop. This means that porosity, despite the homogeneous distribution obtained with graphite flakes, needs to be further increased.
Although different authors introduced similar pore formers in order to increase the performance of cells [74-80], they did not characterize the obtained cells in order to study

the redox behaviour. Consequently, it is not possible to compare the obtained result with available literature data. Nevertheless, these results confirm the hypothesis that tailoring anodic microstructure and increasing the porosity are necessary to produce redox tolerant cells.

CHAPTER 4

ANODE AND HALF CELLS PRODUCED BY ADDING CUSTOMISED CERAMIC PARTICLES

4.1 INTRODUCTION

In order to obtain anodes with higher open porosity and high strength it was considered the idea to add within the anodic microstructure a ceramic powder with different dimensions in comparison with 8YSZ.

A ceramic powder of larger aspect ratio in order to reduce the particle packaging and increase the porosity accordingly, named *Alfa* powder (provided by SOFCpowder Srl), was added within anodic slurry. Because of the promising results obtained during this study the procedure and some microstructure images will not be reported considering that the work is going to be submitted for a patent application.

4.2 EXPERIMENTAL

The half cells were produced by tape casting technology. The anode was produced by using a mixture of 58 wt% of NiO, 8.4-16.8 wt% of 8YSZ and *Alfa* powder to balance.

The anodes were characterized by porosity measurements. In order to understand the influence of *Alfa* powder on the mechanical performances of the half cells, ring-on ring tests with Weibull analysis were carried out. The tolerance to redox cycling was measured by electrochemical and microstructural analyses as described in chapter 2.

4.3 RESULTS AND DISCUSSION

Electrochemical tests

The results of the electrochemical tests performed on the *Alfa* cells are reported in figure 4.1. The behaviour of a commercial cell is plotted as reference in figure 4.2. It is evident that the commercial cell is not redox tolerant. Indeed it failed after the first redox cycle. The *Alfa* cell resisted up to 5 redox cycles.

The trend shows a decrease of the performances after each cycle, even if the first and second have a similar behaviour. A more evident fall of the performance is observed during the 3rd cycle; this behaviour can be addresses to experimental set-up problems, for example a not optimal contact between conducting mesh and cathode, with an increase of cell resistance. With the 4th cycle a sharp OCV decrease is observed while the ohmic polarization is lower in comparison with the previous cycles, confirming the set-up inconvenience. This behaviour can be also ascribed to some little cracks into the electrolyte that can put in contact the anodic and cathodic compartments resulting in fuel combustion and local increase of the temperature with consequent improvement of the performances. The presence of little cracks can explain the OCV loss.

The unexpected performances improvement during the 4th cycle can be alternatively explained by considering that upon a redox cycle, the cermet conductivity may increase as a consequence of the partial disintegration of the YSZ network and of the redistribution of Nickel particles that may divide in smaller ones upon a fast oxidation; this anode microstructure reorganization is believed to account for the improved Ni network percolation [62]. Of course this is true until a critical damage of the structure occurs as observed during the 5th cycle where OCV is low and ohmic polarization is high.

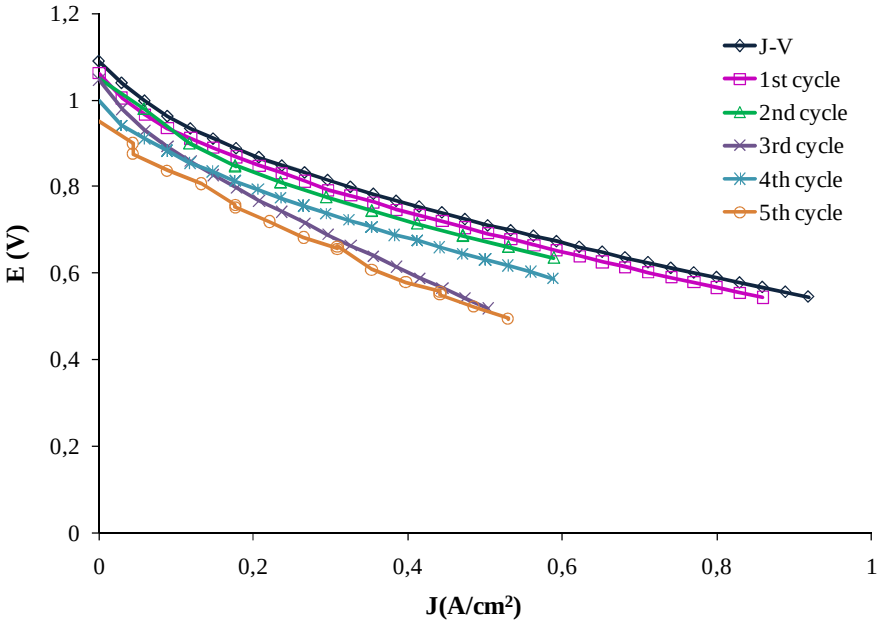

Fig. 4.1: J-V plot of the *Alfa* cell (5 redox cycles).

The OCV of standard and *Alfa* cells are listed in Table 4.1. It is possible to observe that the starting OCV is almost the same for both the cells, while their redox behaviour is totally different.

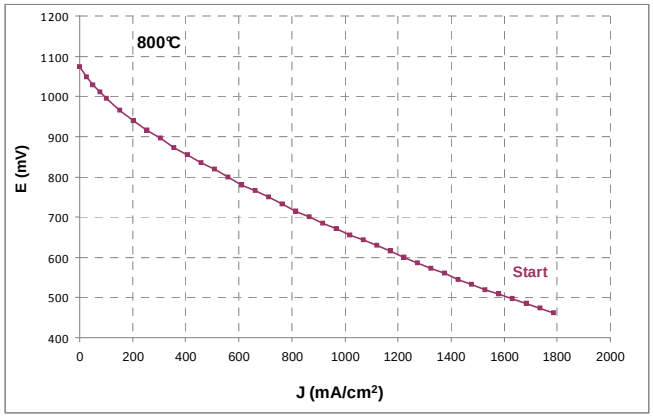

Fig. 4.2: I-V plot of a standard cell, does not show redox tolerance.

Table 4.1: Comparison of OCV (mV) value after redox cycles.

Redox cycles	**STD**	***Alfa* cell**
Start	1070	1089
1st	Broken cell	1061
2nd	Broken cell	1050
3rd	Broken cell	1048
4th	Broken cell	1000
5th	Broken cell	950

The pictures of standard cell after one redox cycle and the so-called *Alfa* cell after 5 cycles, are reported in figure 4.3. From the comparison of the two images the dramatic failure of the traditional cell can be observed. In fact, only when the *Alfa* cell was removed by the test set-up the cell was broken, but as can be observed the active area for the test do not present any crack.

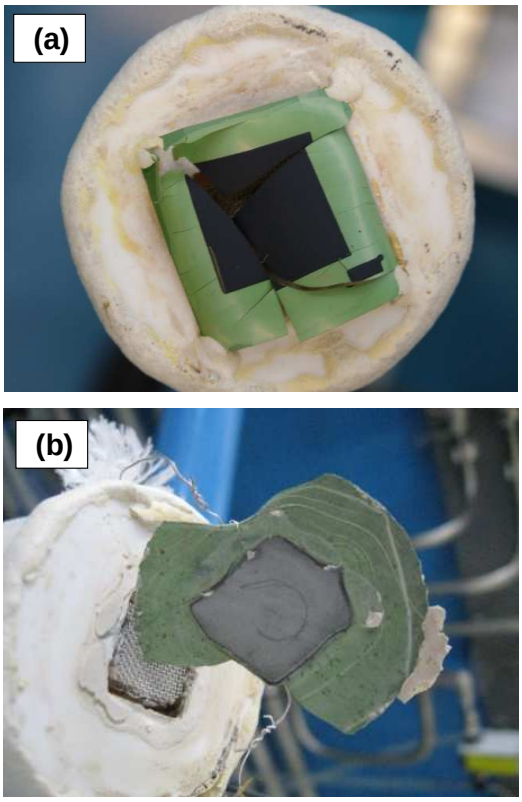

Fig. 4.3: Standard (a) and *Alfa* (b) cells imagines after redox test.

High quality *Alfa* cells were obtained by improving the production process.

For such cells the redox tolerance showed an evident increase up to 15 cycles. The J-V trends after each redox cycle are reported in figure 4.4. The cell shows the same behaviour during the first two cycles, then a continuous decrease in the performances can be observed. The cell was still working after the fifteenth cycle but the test was stopped because of the low power output measured. The open circuit voltage (OCV) is almost the same for all the cycles; this suggesting that no crack has originated or propagated in the electrolyte.

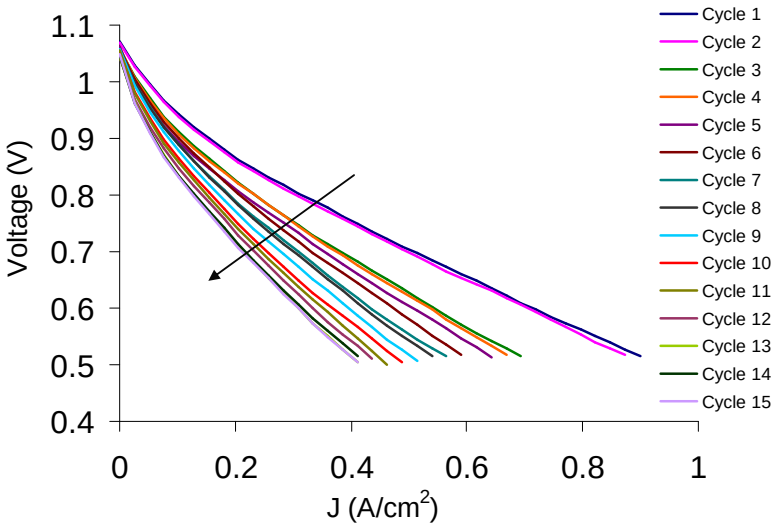

Fig. 4.4: J-V plot of the *Alfa* cell (15 cycles).

Figure 4.5 shows the values of OCV and of current density when the potential is 0.7 V for the *Alfa* cell after each redox cycle. For comparison the corresponding values for a standard cell are also reported. For standard cell, no data are available after the 1st redox cycle. It is worth noting that the commercial cell shows better performances but it cannot stand redox cycling.

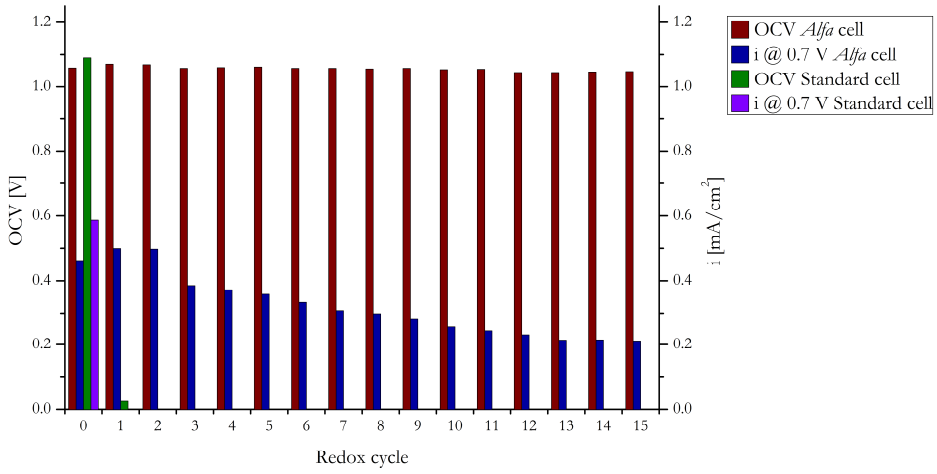

Fig. 4.5: Evolution of OCV and current density @ 0.7 V for standard cell and *Alfa* cell during redox cycling test.

EIS measurements were performed at OCV (Fig. 4.6) and at 0.5 A (Fig. 4.7).

At OCV the contribution of activation polarizations are prevalent with respect to other losses.

As it is possible to observe by the impedance plot reported for each cycle, at high frequencies the real part of the impedance is almost constant for all the cycles; instead at low frequencies it is evident that the activation polarization shows an increasing trend with the redox cycles. This means that cycle by cycle a reduction of three-phase boundary density occurs, due to changes in Nickel distribution. Moreover, the relaxation frequency, i.e. the frequency at which the imaginary part of the impedance reaches its maximum, is measured at decreasing frequencies with the progress of the redox cycles. For instance the relaxation frequency is 1880 Hz at the first cycle, 976 Hz at eighth cycle and 400 Hz at the last cycle (Fig. 4.6).

The decrease of the number of TPB during redox cycles was confirmed by the study of TPB[1] performed on *Alfa* cells as sintered and after 15 redox cycles. It was determined that after the redox cycles the TPB density decrease by 15.6 %.

The loss of the current density observed with the electrochemical tests is higher in comparison with the percentage of TPB losses; this means that many other phenomena of degradation occur in the cells during the redox test, as confirmed by EIS analyses.

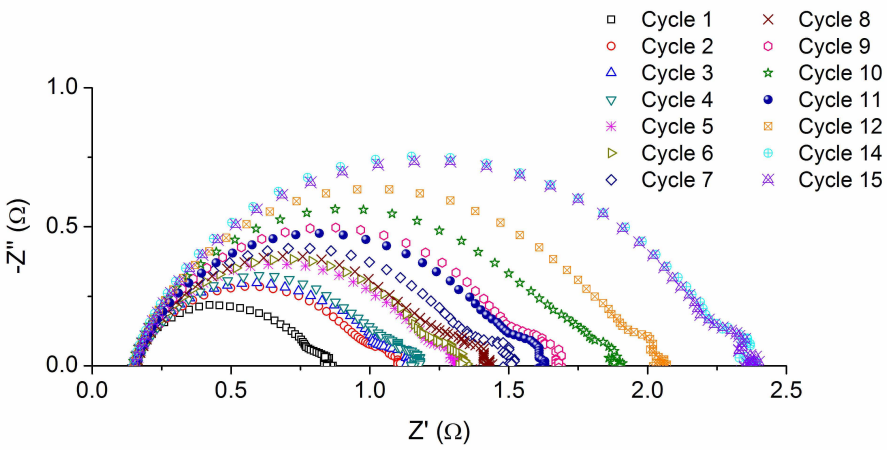

Fig. 4.6: *Alfa* cell impedance measured at OCV for each cycle, active area 1.96 cm^2.

Considering the analyses of impedance at 0.5 A reported in Nyquist diagram (Fig. 4.7), it can be observed that the losses increase after every cycle confirming the trend at OCV. The Nyquist plot shows the overlapping of the two circles relative to the anode and cathode losses. With the increasing of the redox cycles it is possible to distinguish the

[1] The TBP analyses were performed in CIME-EPFL laboratories.

circles. Though the two circles are more evident with respect to the OCV measurement, it is difficult to differentiate the two contributions.

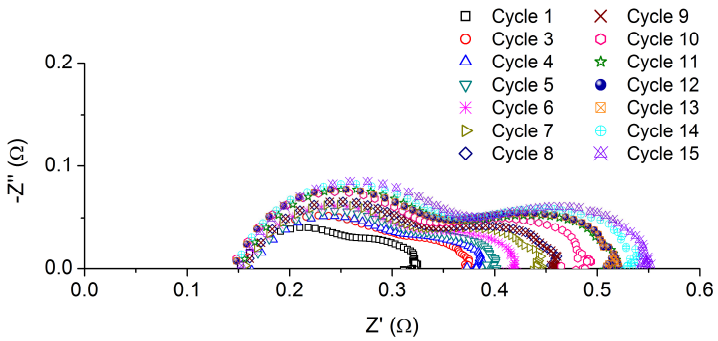

Fig. 4.7: *Alfa* cell EIS curves at 0.5 A and 800°C, active area 1.96 cm^2.

Microstructural analysis

The porosity of these cells was measured after sintering and after the first reduction and the first re-oxidation resulting 38%, 46% and 34% respectively.

A comparison between the porosity of standard anode (without addition of pore former) and of anodes prepared by adding PEMA-co-MMA (PF), or graphite or *Alfa* powder is reported in Table 4.2.

By SEM observation of the *Alfa* cells cross section microstructure, anode shows an outstanding porosity homogeneously distributed; it is also possible to observe the good adhesion between anode and electrolyte in the as sintered cell.

The higher value of the initial porosity of the *Alfa* cells in comparison with the other cells produced can explain their enhanced redox behaviour.

Table 4.2: Anode porosity (%) comparison between different cells.

State of the anode	**STD**	**PF**	**graphite**	***Alfa***
As Sintered	14	14	21	38
After one Reduction	25	33	36	46
After one re-oxidation	13	12	17	34

Changes in the microstructure of the *Alfa* cell after the 15th redox cycle were observed in figure 4.8: growth and coarsening of spongy nickel oxide particles are visible and some cracks are observed within YSZ network, as it is underlined by the arrows. Moreover a different distribution of the porosity is detected, specifically larger voids are present between anode and electrolyte interface. These observations can contribute to explain the increase in polarization losses measured by electrochemical test.

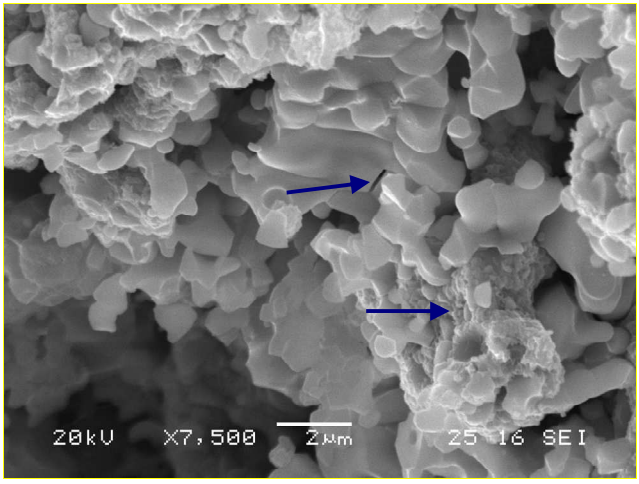

Fig. 4.8: *Alfa* cell anode cross section after 15 redox cycles.

Mechanical testing

The mechanical characterization was performed on the *Alfa* and standard half cells provided by SOFCpower. The mechanical strength was determined by biaxial flexural test using a ring on ring fixture. 30 samples were tested for each kind of cell.

The average dimensions for standard half cells are:

diameter: 25.2±0.1 mm

thickness: 260±20 μm

Instead the average dimensions for *Alfa* half cells are:

diameter: 25.6±0.3mm

thickness: 230±30 μm

The collected data were analyzed in order to estimate Weibull distribution parameters (Tab. 4.3).

Table 4.3: Weibull parameters.

Half cell	σ_0 (MPa)	m
Alfa	148	6.1
standard	540	8.2

The linear regression of the experimental data (Fig. 4.9) show the lower value of the Weibull characteristic strength and module of the *Alfa* cells. This is an expected consequence of the increase in the porosity achieved by the addition of *Alfa* powder to the anodic slurry.

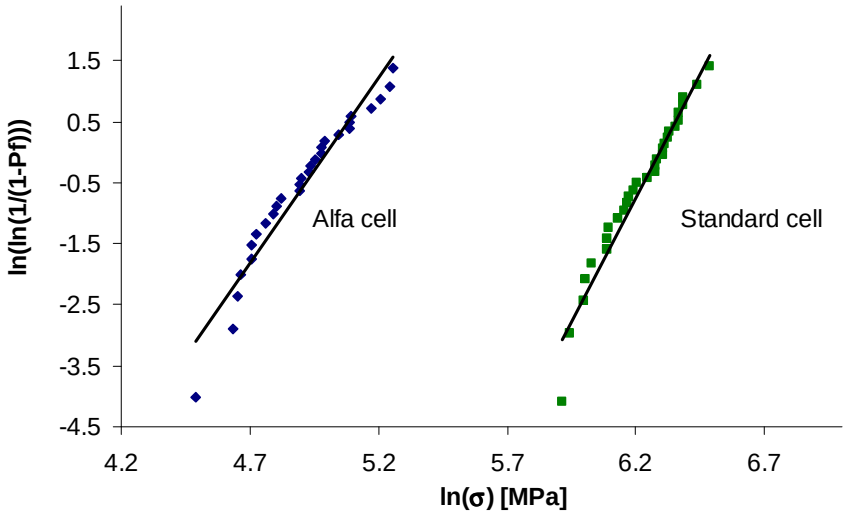

Fig. 4.9: Weibull plot for *Alfa* and standard half cells.

4.4 CONCLUSIONS

Alfa cells were produced by substituting a certain amount of 8YSZ powder with a ceramic powder of larger aspect ratio to increase porosity of the anode.

Redox tolerant cells were obtained: after 15 redox cycles the cells did not show cracks within the electrolyte. Thanks to the modifications within the anodic microstructure obtained by using this powder, it was possible to create a structure with homogeneous high porosity and high compliance which allows Ni volume expansion upon re-oxidation without generating detrimental stresses.

By electrochemical tests, losses in polarization and consequent performances decrease were observed due to changes into the anodic microstructure, such as growth and coarsening of the Ni particles. Nevertheless, the OCV constant value over every cycle demonstrated that the electrolyte did not present significant cracks that can lead to cells failure, as it was confirmed by microstructure analysis.

On the other hand the anode high porosity limit the mechanical strength and a higher probability of failure is expected with *Alfa* than with standard cells. It is necessary then to improve cell mechanical reliability and at the same time obtain an increase in electrochemical performances.

CHAPTER 5

ANODIC POWDERS AND HALF CELLS WITH DOPANT ELEMENTS

The addition of selected doping elements in the anode or the electrolyte is known to improve cells mechanical properties, electrochemical performances and long-term stability [38, 89]. For instance, Al_2O_3 was reported to act as a sintering aid for cubic YSZ [37, 38], and to enhance hardness, fracture toughness and Young's modulus [36, 39]. Moreover, the addition of Al_2O_3 into the anode increases its sintering rate in order to match the electrolyte sintering rate, this allowing to obtain high quality and flat "as sintered" cells [90].

Dopants such as Cr_2O_3, MgO, CeO_2 were also added to the anode in an attempt to increase the resistance to redox cycles [86, 91]. For these reasons, Al_2O_3 and CeO_2 were selected as dopant elements.

In the first paragraph the effect of different amounts of Al_2O_3 and CeO_2 on reduction and oxidation kinetics of NiO/YSZ powders was investigated by thermogravimetric analysis at 800°C in H_2/Ar (reduction) or air (oxidation) atmosphere, associated with detailed microstructural investigation of the samples.
In the second paragraph the behaviour upon redox cycling of Ni/YSZ anodes doped with the selected elements is reported.

5.1 STUDIES OF THE REDOX KINETIC OF THE DOPED POWDERS

5.1.1 *EXPERIMENTAL*

Both Al- and Ce-doped NiO powders were produced by adding 1 to 10 mol% of $Al(NO_3)_3 \cdot 9H_2O$ (Riedel- De Haen, Germany) or $Ce(NO_3)_3 \cdot 6H_2O$ (Alfa Aesar, Germany) to NiO powders (J. T. Baker, USA) in a plastic jar containing ethanol and zirconia grinding media. The suspensions were milled for 24 h and then dried and calcined for 10 h at 900°C. Pure NiO powders were also calcined for 10 h at 900°C and used as reference material.

After calcination, the dopant elements were present as oxides. These samples were labelled considering the dopant element concentration: for example, NiO doped with 3 mol% Al-nitrate was named 3% Al while NiO indicates the calcined reference. Powders were screened through a 100 μm sieve and specific surface area (SSA) was determined. Doped and undoped NiO powders were mixed with 8 mol% yttria stabilised zirconia using a NiO/YSZ weight ratio equal to 58/42, dispersant and distilled water for 20 h in a rotating plastic drum containing zirconia balls. The powders were then dried and ground manually in a mortar. Loose powders were finally heat treated at 1450°C for 2 h for promoting sintering. The resulting samples were manually ground and the fraction passing through 100 μm sieve was used for redox tests.

In analogy with the names assigned to doped NiO powders, doped NiO/YSZ powders were indicated as X% M-YSZ where X is the molar fraction of dopant within the NiO powder and M = Al or Ce.

Mass changes during oxidation and reduction cycles were measured by thermogravimetric analysis; the test procedure is described in paragraph 2.3.
The powder morphology before and after redox cycles was characterized by scanning electron microscopy.

5.1.2 *RESULTS AND DISCUSSION*

Powder characterisation

The specific surface area of the as calcined powders is reported in Table 5.1. It can be observed that SSA is higher in all the doped samples than in the undoped NiO; in particular, in case of Al addition, the higher is the doping level, the higher is the final SSA. On the other hand, for powders doped with different amounts of Ce, their SSA seems to be rather independent from Ce concentration, ranging from 3.3 (1% Ce) to 4.0 m^2/g (3% Ce). Considering that as received NiO powder possesses a SSA of 3.3 m^2/g and the calcined one only 1.0 m^2/g, it is evident that the treatment at 900°C accounts for the coarsening of the

NiO grains. Therefore, the use of Al- or Ce-nitrate inhibits the coarsening of the NiO upon calcination. Such considerations can be supported by the observations of powder morphology by SEM (Fig. 5.1a).

Table 5.1: Specific Surface Area of the as Calcined NiO Powders.

Sample	**NiO**	**1% Al**	**3% Al**	**5% Al**	**10% Al**
SSA (m^2/g)	1.0	3.8	4.3	6.6	15.4
Sample	**NiO**	**1% Ce**	**3% Ce**	**5% Ce**	**10% Ce**
SSA (m^2/g)	1.0	3.3	4.0	3.4	3.7

For sake of briefness, only the microstructures of the most representative samples are reported here. The chosen samples are the reference NiO, 1% Al, 10% Al, 3% Ce and 10% Ce. Each NiO powder was analysed (i) as calcined (Fig. 5.1a), (ii) mixed with YSZ and sintered (Fig. 5.1b), and (iii) after two redox cycles (Fig. 5.1c).

As for the as-calcined NiO powder (Fig. 1a), a distinction can be pointed out between Al- and Ce-doped samples. All doped powders are finer than the reference one; the powder fineness increases with the amount of Al-doping, while it is substantially constant for all Ce-doped powders, in agreement with the Nitrogen adsorption data.

The heat treatment of NiO/YSZ powders for 2 h at 1450°C leads to the formation of well developed sintering necks between particles in contact; a YSZ matrix can also be pointed out, which exhibits areas with varying densities, clearly depending on the degree of agglomeration of the pristine powder (Fig. 5.1b). The comparison of each sample in the as-sintered state (Fig. 5.1b) and after two redox cycles (Fig. 5.1c) allows to point out variations in the microstructure: an increase in porosity, grain coarsening and different distribution of NiO. Nickel oxide is finely and uniformly distributed within the YSZ

network in the as-sintered samples; conversely, after the two redox cycles, it appears coarser and characterized by irregular shape. This can be explained by considering that the first reduction of the small and uniformly distributed NiO particles occurs with volume reduction and porosity increase. In reducing environment at high temperature Ni can diffuse on YSZ surface and agglomerate. The re-oxidation and volumetric increase of such coarsen Ni particles can locally lead to intense stresses in the YSZ network [58].

It is interesting to observe the presence of some intergranular cracks between zirconia grains generated by Ni particles expansion upon oxidation. In some cases intragranular cracks were observed as well (sample 10% Ce-YSZ in Figure 5.1c).

Different portions of the same samples were analysed in order to determine whether any differences in the densification of the zirconia matrix has an influence in the coarsening of NiO grains and in crack formation. As an example, different portions of 1% Ce-YSZ sample after two redox cycles are reported in figure 5.2.

One can observe that in the zones were more necks are formed between zirconia particles and the matrix is denser (Fig. 5.2a), the number of cracks is higher. In such areas, the dimensions of the NiO particles are smaller, suggesting that the zirconia skeleton inhibits the Ni agglomeration. Nevertheless, when the particles are oxidised, their volumetric expansion cannot be accommodated by the porosity and introduces high stresses in the structure, with consequent cracks nucleation and propagation (Fig. 5.2a).

On the other side, where the zirconia matrix is looser (Fig. 5.2b), the coarsen NiO particles are bigger. In such zones, the Ni agglomeration is less inhibited by the zirconia matrix and cracks formation is less severe, this indicating that even the coarser particles can expand freely in the larger voids of the network.

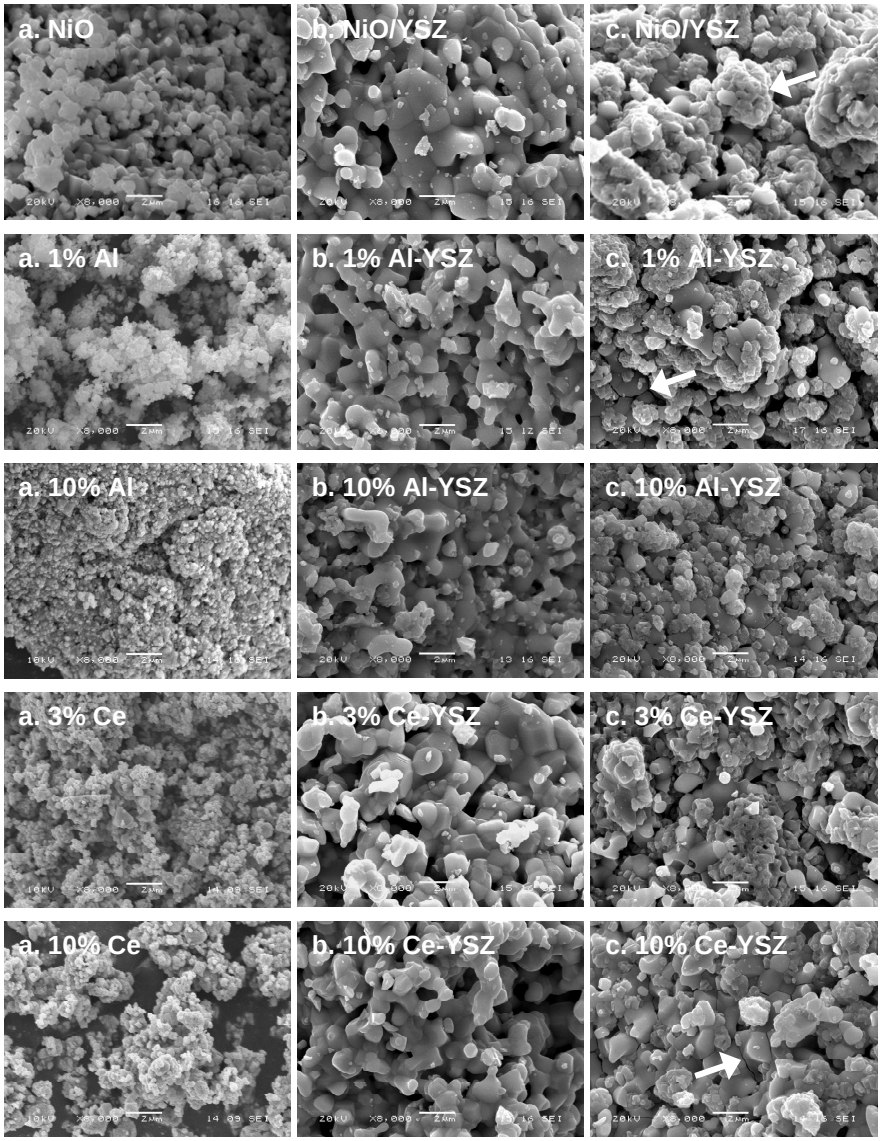

Fig. 5.1: SEM micrographs of selected NiO doped and undoped samples: as calcined NiO powder (column a), as sintered NiO/YSZ (column b), NiO/YSZ after two redox cycles (column c). The samples are, from the top to the bottom: the reference, 1% Al, 10% Al, 3% Ce and 10% Ce. Coarsening of NiO (reference sample in Figure 5.1c), intergranular cracks (sample 1% Al-YSZ in Figure 5.1c) and intragranular cracks (sample 10% Ce-YSZ in Figure 5.1c) are highlighted by arrows.

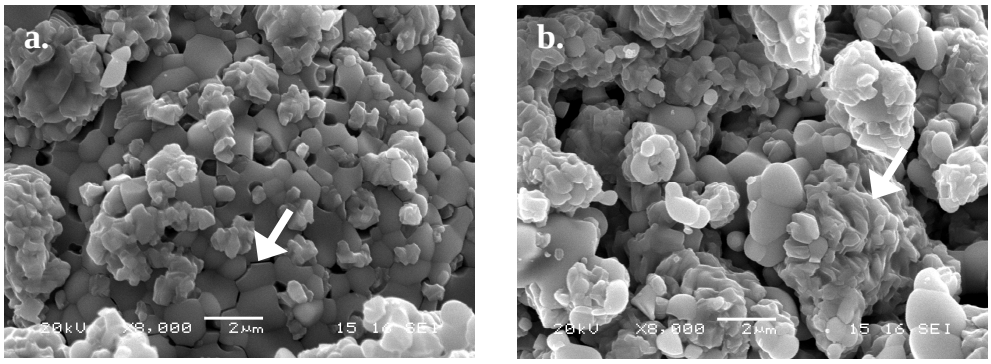

Fig. 5.2: SEM micrographs of two different portions of sample 1% Ce-YSZ, after two redox cycles. The arrows indicate: a. intergranular cracks, b. coarsening of NiO.

Thermogravimetric analysis

First Reduction. The normalised mass change and mass change rate as function of time upon the first reduction are shown in figures 5.3 and 5.4 for Al- and Ce-doped samples, respectively. The curve corresponding to undoped NiO/YSZ is reported for comparison. The mass change values are normalised with respect to the final weight of the completely reduced samples, by the following relation:

$$\alpha_{red} = \frac{m_t - m_f}{m_0 - m_f} \tag{5.1}$$

where m_0 and m_f are the initial and the final mass, respectively, and m_t is the mass at time t. After a reduction time of 180 min all the thermogravimetric curve are constant, indicating that the reduction process is complete.

Concerning the Al-doped samples (Fig. 5.3), it is evident that doped samples reach the final reduced state more quickly than the reference powder. After 10 min treatment, the reduced fractions for 1% and 10% Al-YSZ are 0.64 and 0.95, respectively (Fig. 5.3a). Such results suggest that the higher is the Al doping level, the faster is the reduction process.
The peaks of the reduction rates range from -1.4 % min^{-1} for the undoped sample to -1.6 % min^{-1} for the 10% Al-YSZ doped powder (Fig. 5.3b). Such data can be explained by observing that the specific surface areas of the samples (Table 5.1) are significantly increased by the addiction of the dopant (from 1 to 15 m^2/g in the as calcined state). The higher surface available for the reduction reaction can be the reason for the observed behaviour. It is important to say that the specific surface areas of the same powders mixed with YSZ and sintered were not measured, but from the SEM images (Fig. 5.1b) it is clear that they possess finer microstructure than NiO/YSZ reference.

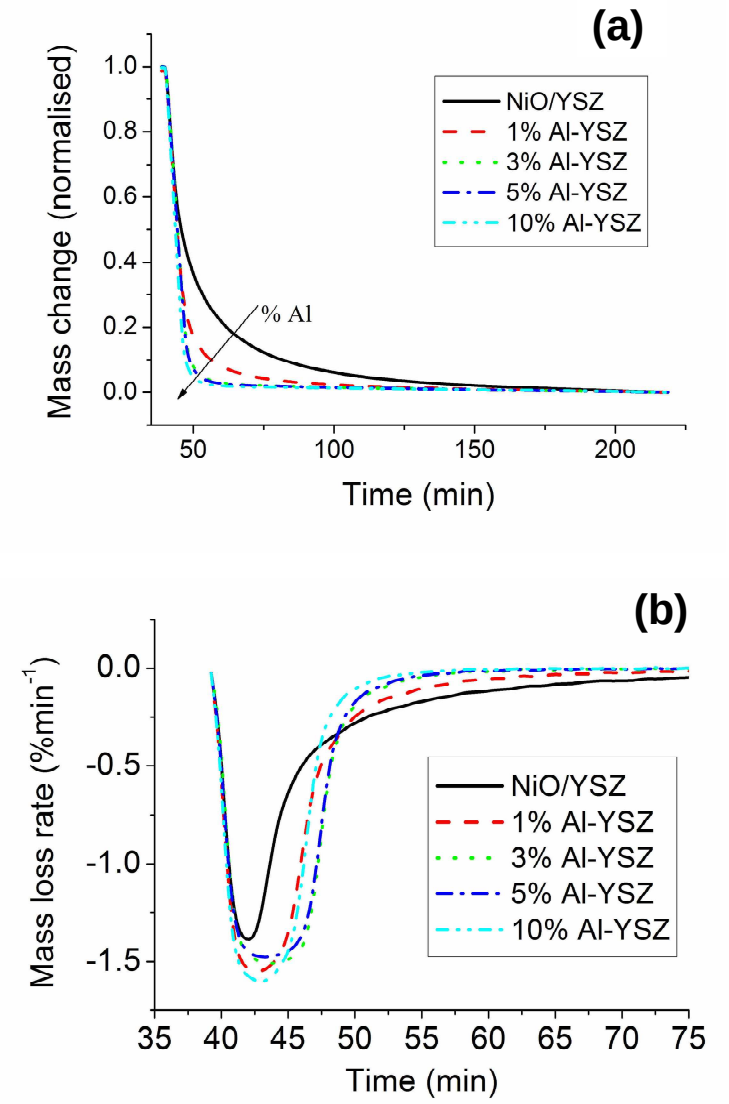

Figure 5.3: Normalised mass change (a) and mass loss rate (b) versus time upon first reduction for the Al-doped powders. The DTG graph (b) is relative to the time interval where the mass change is more significant.

The effect of the addiction of Ce on the first reduction cycle is less clear (Fig. 5.4). The curves corresponding to limited doping level samples are very close to the reference one, while a different behaviour can be appreciated for the 10% Ce-YSZ doped samples. Nevertheless, as it was the case for the Al-doped sintered samples, also in this case the higher is the doping level, the faster is the reduction process. After a reduction time of 10 min, the reduced fractions for 1 and 10% Ce-YSZ doped powders are equal to 0.63 and 0.76, respectively (Fig. 5.4a). Such values are always lower than data obtained for Al-doped samples.

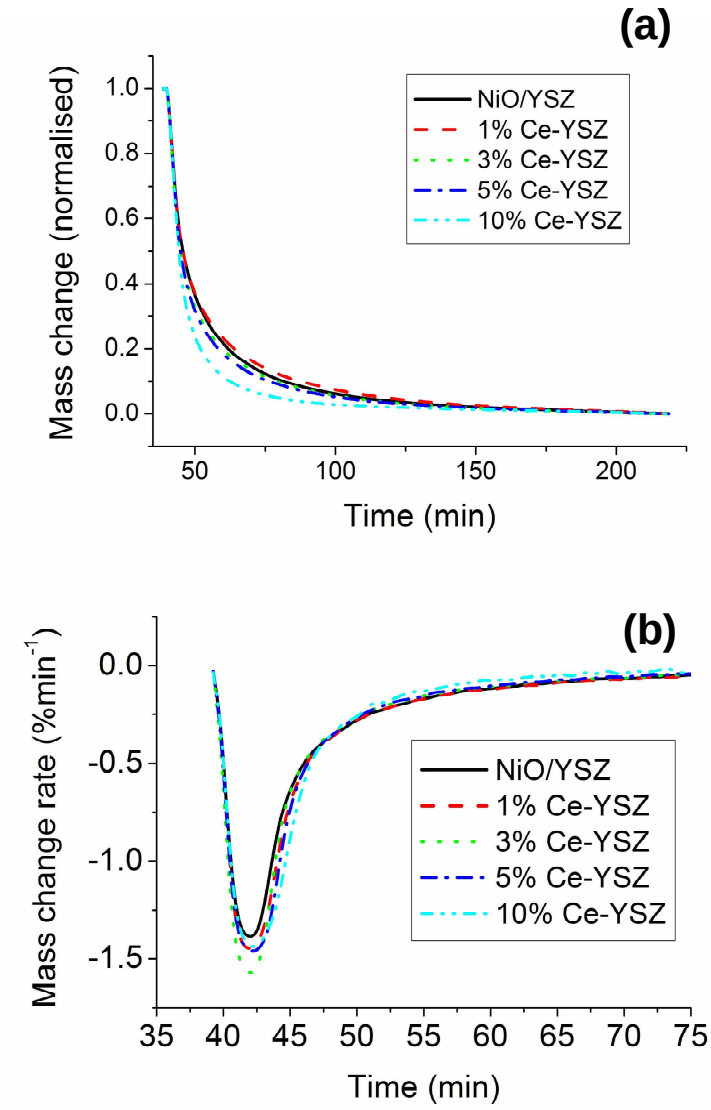

Fig. 5.4: Normalised mass change (a) and mass change rate (b) versus time upon first reduction for the Ce-doped powders. The DTG graph (b) is relative to the time interval where the mass change is more significant.

First Re-Oxidation. The normalised mass change and mass change rate versus time upon the first re-oxidation are shown in figures 5.5 and 5. 6, for the Al-doped samples and the Ce-doped samples, respectively.

The mass change values are normalised with respect to the final weight of the completely oxidized samples, by the following relation:

$$\alpha_{ox} = \frac{m_t - m_0}{m_f - m_0} \tag{5.2}$$

Only the data corresponding to first 60 min are reported since the oxidation process is very fast and is substantially complete in the first hour. The oxidation process is always faster than the reduction one. For the reference powder the maximum reduction rate is -1.4 % min^{-1}, while the maximum oxidation rate is 4.1 % min^{-1}.

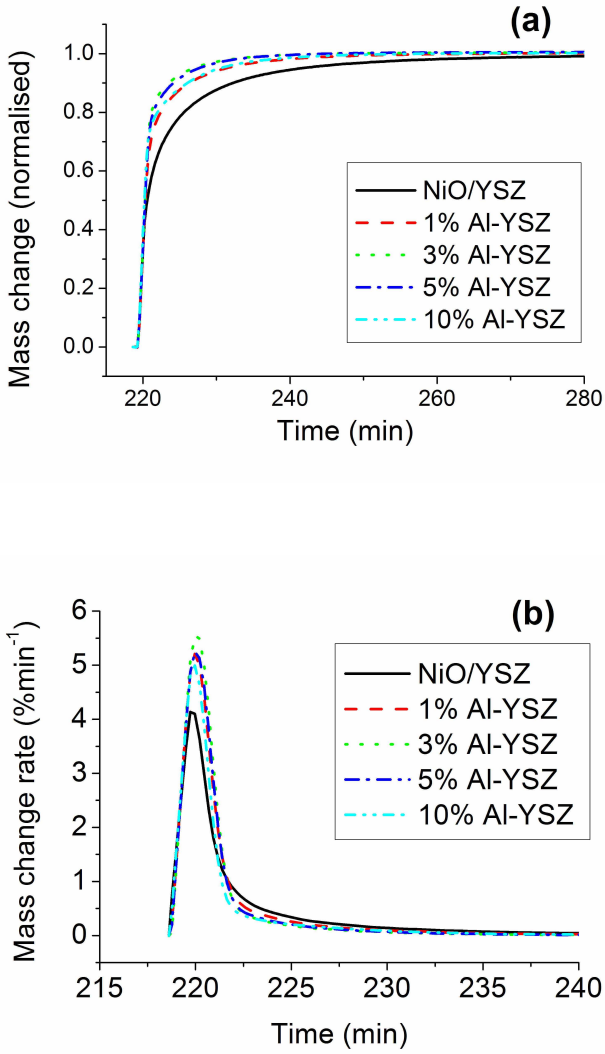

Fig. 5.5. Normalised mass change (a) and mass change rate (b) versus time upon first re-oxidation for the Al-doped powders. The DTG graph (b) reported is relative to the time interval where the mass change is more significant.

The oxidation rates are faster for both the Al- and the Ce-doped samples with respect to pure NiO/YSZ.

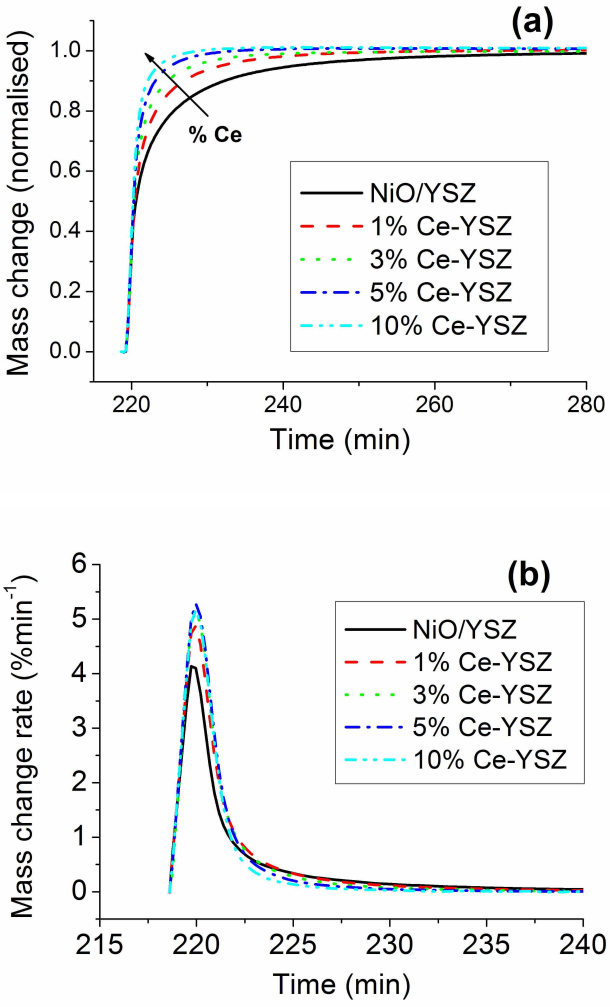

Fig. 5.6: Normalised mass change (a) and mass change rate (b) versus time upon first re-oxidation for the Ce-doped powders. The DTG graph reported (b) is relative to the time interval where the mass change is more significant.

The oxidation maximum rate is observed in the 3% Al-YSZ doped powder (5.5 % min^{-1}, Fig. 5.5b). After an oxidation time of 5 min, the oxidized fractions of the reference powder, 1% and 10% Al-YSZ doped samples are 0.77, 0.87 and 0.87, respectively (Fig. 5.5a).
For the 1% and 10% Ce-YSZ doped powders, the oxidized fractions are 0.85 and 0.97, respectively (Fig. 5.6a). In particular for the Ce-YSZ samples the higher the dopant concentration, the faster is the reaction.

Second Reduction and Re-Oxidation Cycle. A second redox cycle was performed on all samples in order to point out any difference with the first cycle. The related mass change and mass change rate diagrams are reported in appendix A. For sake of conciseness, only the results of 1%Al-YSZ and the NiO/YSZ reference are shown, the behaviour of such samples being common to all the investigated ones. The diagrams corresponding to the reduction and oxidations are shown in figures 5.7 and 5.8, respectively. It is evident that the second reduction process and the second re-oxidation process are always faster than the first one. Comparing the first and the second oxidation, the maximum oxidation rate for pure NiO changes from 4.1 to 4.7 % min^{-1}; for 1%Al-YSZ powders it changes from 5.2 to 5.6 % min^{-1}. The faster second reduction and re-oxidation cycle suggests that the first redox cycle is responsible for a modification of the microstructure related to a different pore distribution caused by Ni coarsening which allows an easier gas diffusion. The micrographs of the selected samples before and after the redox cycles (Fig. 5.1b and 5.1c) show in fact that a change in the NiO particle morphology took place.

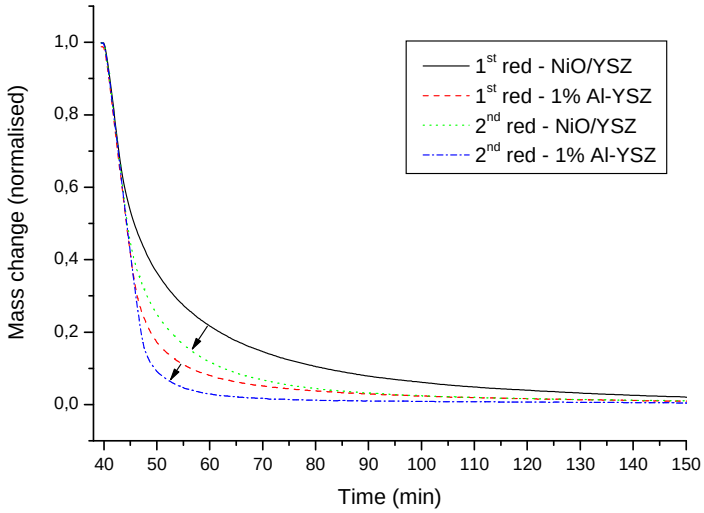

Fig. 5.7: Normalised mass loss versus time upon first and second reduction for NiO and 1% Al samples.

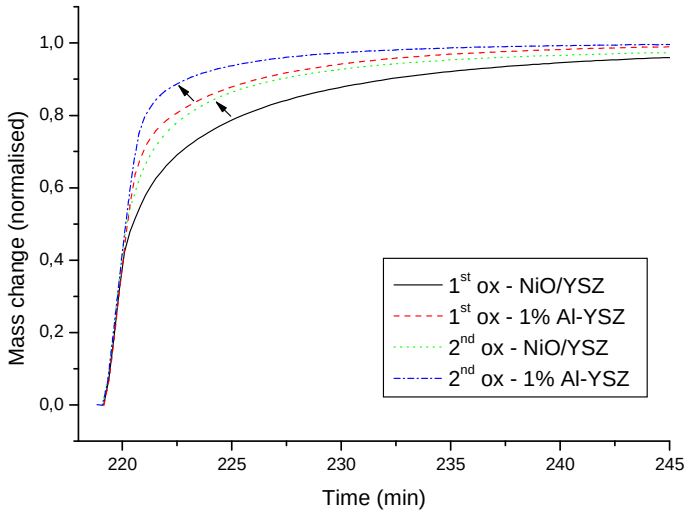

Fig. 5.8: Normalised mass change versus time upon first and second re-oxidation for NiO and 1% Al samples.

5.1.3 *CONCLUSIONS*

NiO/YSZ powders with different amount of Al- or Ce-doping elements were tested by thermogravimetric analysis to investigate how they modify the reduction and re-oxidation kinetics.

The specific surface area of the calcined NiO powder increases with the amount of Al, whereas it is almost independent when Ce is added.

It was found that both dopant elements increase the reduction and oxidation rates with respect to the reference powder. The reduction rate increases monotonically with Al amount; on the other hand only when high Ce load is used (10%) the first reduction rate is sensibly affected.

The second reduction and re-oxidation are faster than the first one. The presence of coarser NiO particles generated in the first cycle and a consequent porosity modification can explain the generalized reaction rate increase.

5.2 DEFORMATION OF UNCONSTRAINED HALF CELL WITH DOPED ANODE

In this paragraph redox behaviour of 1%Al-doped and 5%Ce-doped half cells was analyzed by monitoring in-situ the deformation associated to cyclic changes of the operative atmosphere. This characterization aimed to be a straightforward way to determine the redox stability of anodes with different composition and microstructure. Moreover, it has to be underlined that the observation of the unconstrained deformation of the cell during redox cycles gives additional and different information with respect to those obtained by electrochemical test.

5.2.1 *EXPERIMENTAL*

NiO powders doped with 1 mol% of $Al(NO_3)_3 \cdot 9H_2O$ or 5 mol% of $Ce(NO_3)_3 \cdot 6H_2O$ or just calcined were prepared as described in paragraph 5.1.1.

Different half cells were produced by using the obtained NiO powders for the anode, with NiO to YSZ ratio of 58 to 42 by weight. Anode and electrolyte were prepared by water-based sequential tape casting technique (par. 2.1). Unlike the typical electrolyte materials, for the half cells made with NiO calcined anode the electrolyte was produced with zirconia FYT13-002H (Unitec, UK). Green bi-layers were sintered at 1450 °C for 2 h. Curvature evolution upon redox cycling on the produced half cells was performed following the procedure described in the paragraph 2.7. The microstructure of the cells was analyzed by scanning electron microscope.

5.2.2 RESULTS AND DISCUSSION

Deformation during redox cycle

The curvature evolution upon a redox cycle is reported in figures 5.9 and 5.10. As a convention we chose to report positive curvature for half cells bent towards the electrolyte and negative for those bent towards the anode.

Figure 5.9 shows the deformation associated to the reduction of the samples. The process is very fast, the changes in the sample curvature being observable within the first 20 min. When the cell bends in the direction of the anode, one can suppose that the anode shrinks, while it expands when the cell bends toward the electrolyte. As observed before, NiO to Ni reduction is associated with a volume decrease. One may therefore expect that the anode shrinks and this in fact happens in the case of 1%Al-doped (anode doped with $Al(NO_3)_3 \cdot 9H_2O$) and NiO-calcined (reference) cells (negative curvature).

Conversely, it is very interesting to observe how 5%Ce-doped sample bends towards the electrolyte upon reduction; this somehow surprising behaviour can be explained considering that ceria is very sensible to the gas atmosphere. In a reducing environment Ce^{4+} can be reduced to Ce^{3+} and the reduction can be accompanied by volume increase [101]. Such volume increase produces an elongation of the anode and the cell assumes a positive curvature.

The curvature upon the re-oxidation is reported in Figure 5.10. The geometrical changes associated with re-oxidation occur within the first 40 min; all samples develop a positive final curvature.

The initial curvature at the beginning of the oxidation step corresponds to the curvature at the end of reduction step. Consequently, 1%Al-doped and NiO-calcined samples start from a negative curvature. Then, a positive curvature is observed, this indicating that samples bend toward the electrolyte; this behaviour is caused by the re-oxidation of Ni to NiO with a volume increase and consequent anode elongation. The curvature reaches a maximum,

which is very large for the 1%Al-doped samples (22.2 m^{-1}), and, then stabilizes to lower positive values.

An analogue inversion in the curvature rate during oxidation (cell bending at first towards the electrolyte and then towards the anode), was also previously observed by Malzbender et al. [102]. Faes et. al. [103] attributed such curvature inversion to creep phenomena occurring in the anode and to movement of the oxidation front. In addition, one can also consider that cracks formed during the process can contribute to relax internal stresses and reduce the observed curvature.

It is also worth noting that, analogously to what happens in the reduction process, the 5%Ce-doped sample in the first 2 min of oxidation shows an opposite behaviour, i.e. a negative curvature rate. The initial curvature decrease could be ascribed to the oxidation of the Ce^{3+} to Ce^{4+} with a volume decrease followed by a re-increase of the curvature due to the volumetric expansion of Ni re-oxidation.

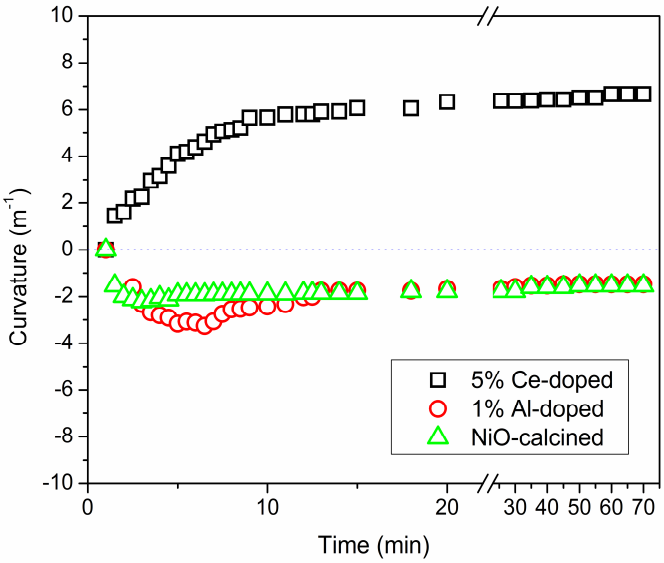

Fig. 5.9: Curvature evolution upon reduction.

The opposite behaviour of Ce^{3+} and Ni observed during oxidation and reduction allows to suppose that the optimization of CeO_2 concentration with respect to NiO could decrease the half cell deformation and increase redox tolerance.

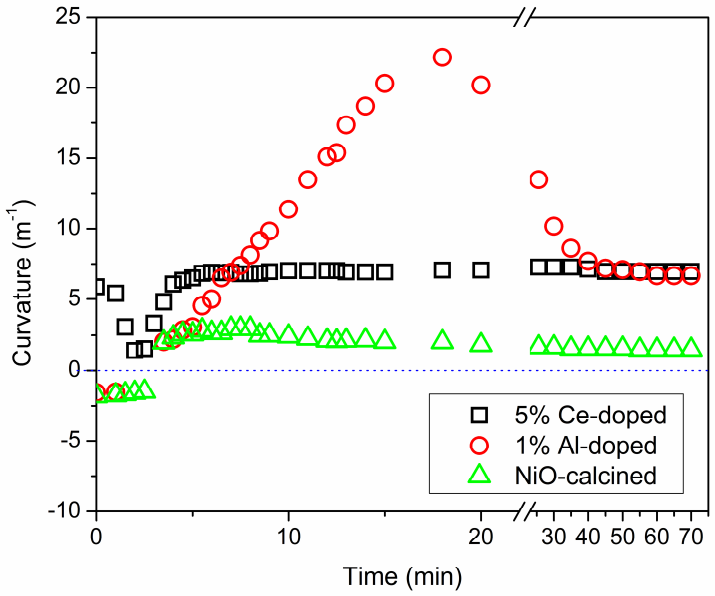

Fig. 5.10: Curvature evolution upon re-oxidation.

Microstructures analysis

Figures 5.11 and 5.12 report the anode microstructure and the electrolyte surface before the test, respectively. Nickel oxide particles are evenly distributed in the YSZ matrix. One can also observe (Fig. 5.11b) that 1%Al-doped anode shows a denser microstructure. The open porosity in the oxidised state, as measured by Archimedes method, is in fact 24%, 13% and 18% for NiO-calcined, 1%Al-doped and 5%Ce-doped samples, respectively.

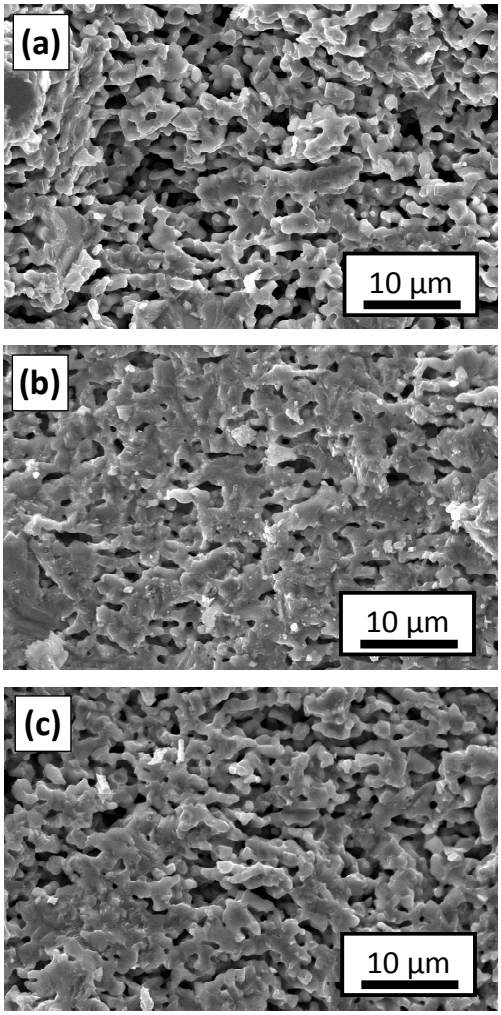

Fig. 5.11: Cross section of the as produced anode in NiO-calcined (a), 1%Al-doped (b) and 5%Ce-doped (c) sample.

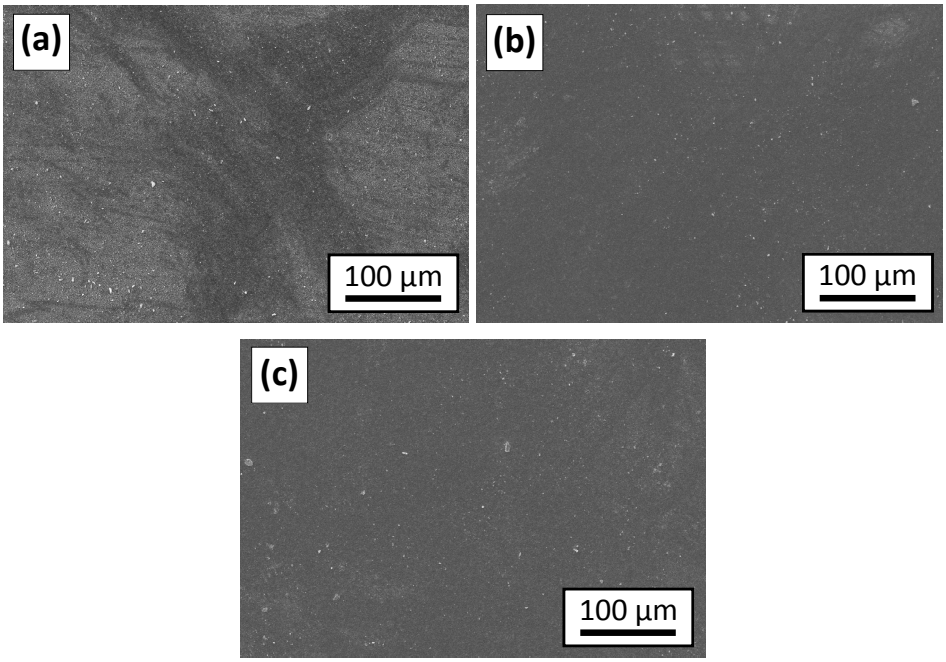

Fig. 5.12: As produced electrolyte surface in NiO-calcined (a), 1%Al-doped (b) and 5%Ce-doped (c) sample.

The electrolyte surface of NiO-calcined, 1%Al-doped and 5%Ce-doped samples after one redox cycle is shown in figure 5.13. Cracks are clearly visible in all samples. Density of cracks and severity of damages decrease moving from 1%Al-doped to 5%Ce-doped and to NiO-calcined sample. In the latter sample the cracks are evident only at high magnifications.

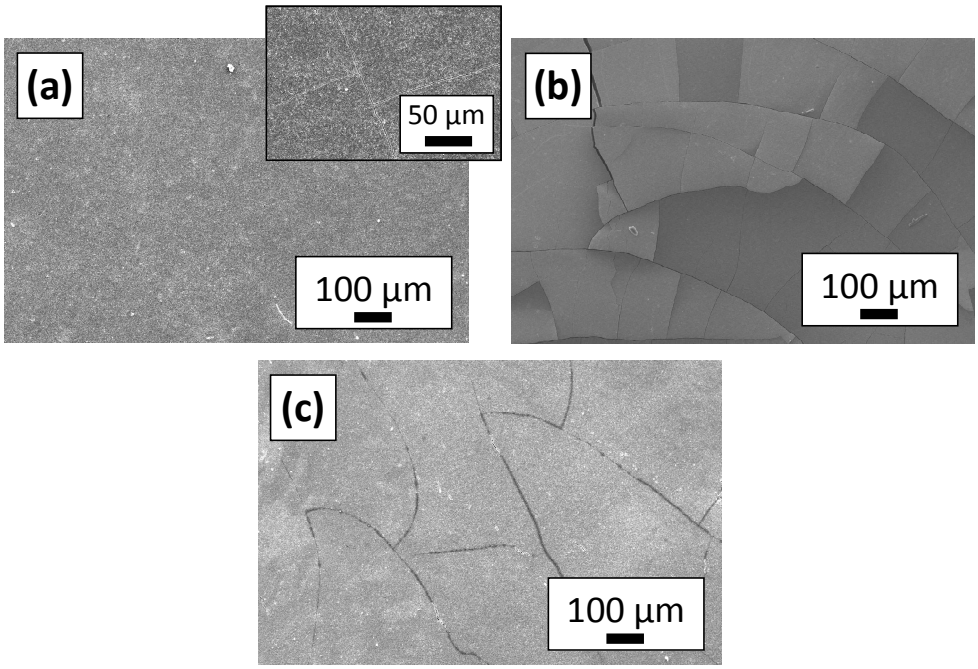

Fig. 5.13: Electrolyte surface after re-oxidation in NiO-calcined (a), 1%Al-doped (b) and 5%Ce-doped (c) sample.

A larger number of cracks are clearly visible in 1%Al-doped sample. One can remind that such sample exhibits the highest curvature during oxidation and the highest expansion of the support anode. This behaviour can be explained by considering that the anodic microstructure of 1%Al-doped sample is denser if compared to the others.

The coarsening of Ni particles in the reduced state and their volumetric expansion upon oxidation induce higher stresses that account for larger macroscopic expansion. The low porosity of the anodic support cannot accommodate the Ni re-oxidation. It was reported elsewhere that typical anode strain limit during re-oxidation is in the range 0.1 – 0.2% [103]. All samples considered here exceed clearly such limit, as demonstrated by the electrolyte failure.

The cross section of anode-electrolyte interface after re-oxidation is reported in figure 5.14. Redox cycle modifies the anodic microstructure and different distribution and coarsening of nickel oxide particles are evident by comparing figures 5.11 and 5.14. The higher density of 1%Al-doped sample is clear. Such higher density was expected since it was previously observed that alumina acts as sintering aid for Ni/YSZ anode [37, 38]. In the cross section of 1%Al-doped sample (Fig. 5.14b) it is also possible to observe cracks within the electrolyte and the anode. The higher porosity of NiO-calcined and 5%Ce-doped samples can explain the better behaviour with respect to the 1%Al-doped sample, though the presence of cracks within the electrolyte (Fig. 5.14c).

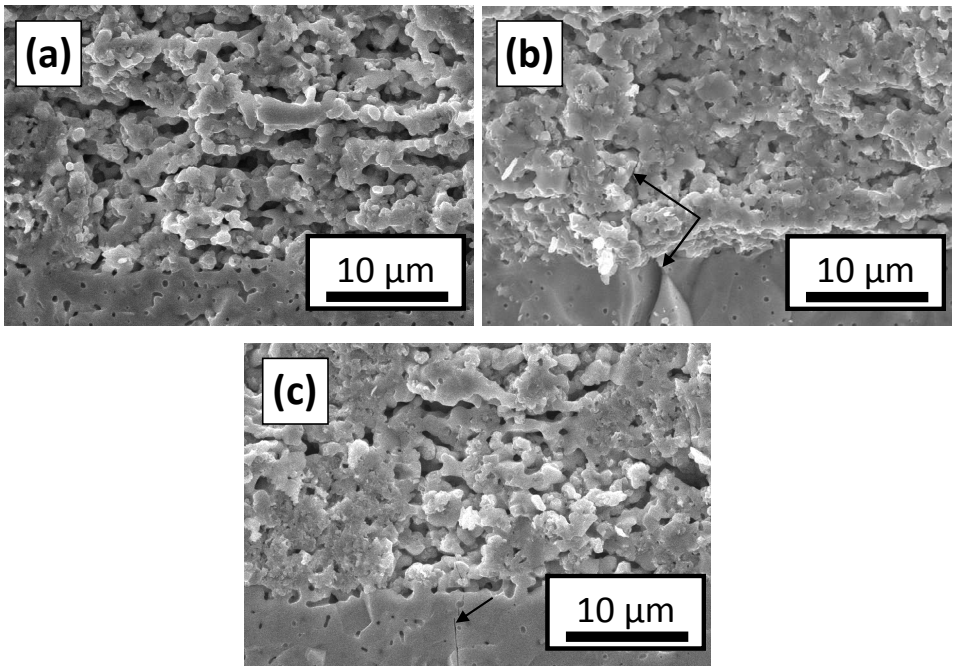

Fig. 5.14: Cross section of the anode interface after one re-oxidation: NiO-calcined (a), 1%Al-doped (b) and 5%Ce-doped (c) sample. Cracks are indicated by arrows.

The analysis of the microstructure confirms that the key point to improve redox tolerance of anode supported cells is to increase the anode porosity in order to tolerate Ni particle expansion during re-oxidation and limit the generation of stress.

Stress analysis

The maximum value of the measured curvature was used to estimate the stresses which are developed in the half-cell and the theoretical elongation of the anode upon oxidation. The strain difference between anode and electrolyte ($\Delta\varepsilon$) and the maximum tensile stress in the electrolyte (σ_1^{max}) depend on the curvature radius according to the following equations (rearranged from [104-107]):

$$\Delta\varepsilon = \left[\frac{m^4n^2 + 2mn\left(2m^2 + 3m + 2\right) + 1}{6\left(m+1\right)^2 mn}\right]\left(\frac{t_1 + t_2}{r}\right)\left(1 - \nu_1\right) \tag{5.3}$$

$$\sigma_1^{\max} = \left[\frac{m^2n\left(4m + 3\right) + 1}{6\left(m+1\right)^2 mn}\right]\left(\frac{t_1 + t_2}{r}\right)E_1 \tag{5.4}$$

where r is the curvature radius, E_1 and E_2 the elastic modulus of the electrolyte and anode, respectively, ν the Poisson ratio, $m = t_1/t_2$, the thickness ratio and n the modulus ratio, given by:

$$n = \left(\frac{E_1}{1-\nu_1}\right)\left(\frac{1-\nu_2}{E_2}\right) \tag{5.5}$$

If we consider a monolithic electrolyte layer, its dimensions would be constant regardless of the atmosphere (oxidizing or reducing): the term $\Delta\varepsilon$ in Eq. 5.3 is the elongation of the anode only. For the calculation we can assume a Poisson ratio of 0.3 and a Young's modulus of 200 GPa and 100 GPa for the electrolyte and the anode, respectively [102]. The thickness of each layer was measured by SEM. The maximum anode strain and electrolyte tensile stress are reported in Table 5.2.

Table 5.2: Maximum anode strain ε_{max} and electrolyte tensile stress σ_{max} (MPa) during the re-oxidation.

	NiO-calcined	1% Al-doped	5% Ce-doped
$\varepsilon_{max\ \%}$	0.26	0.97	0.37
σ_{max}	650	1949	760

The tensile strength of a typical 8YSZ electrolyte ranges between 150 and 250 MPa [108, 109]. As shown in Table 5.2 the maximum calculated tensile stress is significantly higher than the electrolyte tensile strength and this leads to the formation of cracks that can be observed in the electrolyte as shown in figure 5.13.

1%Al-doped sample is subjected to the maximum tensile stress and anode elongation, while both quantities are minimum in the NiO-calcined specimen. Also the crack density and width are maximum in the 1%Al-doped sample (Fig. 5.13b). Comparing the three samples, one can observe that the trend in electrolyte stress, anode elongation and crack density is opposite to the trend in the porosity, being it NiO-calcined > 5%Ce-doped > 1%Al-doped. In other words, a higher porosity minimizes the anode elongation, which in turn minimizes the stress in the electrolyte.

It is worth to say that although the performed elastic analysis furnishes an estimation of the stresses and can be employed to compare different samples, it is not obviously

rigorous. In fact, due to the relatively high temperature (800°C) of the process and to the exothermicity of the Ni →NiO reaction, the cell behaviour upon redox cycle may not be purely elastic [103].

A complete analysis of the stresses should rely on a more complex visco-elastic approach. In addition, curvature and elastic modulus, curvature rate, viscosity of the layers, oxidation front movement and real sample temperature should be known. Nevertheless, the high curvature level reached by 1%Al-doped samples is reflected in the multiple and severe cracking of the electrolyte, this confirming that the in situ observation of the curvature is a rapid and effective method to test multiple samples for redox tolerance.

5.2.3 *CONCLUSIONS*

Redox behaviour of anode supported half cells doped with Al_2O_3 and CeO_2 was investigated by monitoring in-situ the deformation caused by cyclic changes of the operative atmosphere.

During oxidation, 1%Al-doped samples present the highest curvature variations and maximum tensile stress, this resulting in higher density of cracks accounted for the limited porosity of the anode. Indeed, the denser is the anode, the higher are anode deformation upon NiO expansion during re-oxidation and internal stresses with consequent cell failure. Samples produced using pure NiO and 5%Ce-doped NiO powder show lower deformations due to their larger porosity, though this is not enough to avoid crack generation within the electrolyte. The higher density of 1%Al-doped sample in comparison with the other samples can be attributed to the sintering aid effect of alumina within Ni/YSZ anode.

When CeO_2 is present as dopant, the volumetric effect associated with Ni oxidation and successive reduction is counterbalanced by deformations correlated to CeO_2 – Ce_2O_3 transformation.

The obtained results lead to important understanding of the role of doping elements on the redox process; limitation of the anode expansion upon re-oxidation appears to be a first

approach for increasing redox tolerance of anode supported cells. This can be accomplished by considering the addition of a suitable amount of doping elements with an opposite volumetric behaviour to NiO (such as CeO_2) and/or by increasing the anode porosity to tolerate Ni particles re-expansions.

CONCLUSIONS

In the present work important results regarding the redox behaviour of anode supported planar SOFCs have been obtained which can be useful for the production of redox tolerant devices.

A strong relation has been pointed out between anode microstructure and redox behaviour. Careful and tailored modification of the anode microstructure was adopted as strategy in order to overcome such issue and decrease the stresses within the electrolyte and avoid consequent crack formation due to NiO expansion during re-oxidation. The influence of different modifications produced within the anodic microstructure was considered. For this reason different kinds of pore former were added to the anodic slurry.

PU foam, PEMA-co-MMA, PMMA and graphite flakes were selected as fugitive materials to increase anode porosity. It was observed that the amount and morphology of pore former play a key role on the final microstructure.

Anodes produced with addition of PU foam showed high fragility. Despite the open and interconnected porosity, they are not suitable for SOFCs pre-pilot and industrial production unless their mechanical strength is increased.

The comparison between anodes having different microstructure but the same amount of organic materials allowed to draw some interesting conclusions, comparing the role played by each pore former in relation to microstructure and the effect on redox behaviour. Actually, the standard anodes and the substrates obtained with the addition of PEMA-co-MMA beads as fugitive materials, both having an initial porosity of 14%, displayed similar behaviour upon redox cycling. The cells failed just upon one redox cycle, showing no improvement in support robustness. It was observed that changes associated to different pore morphology, while keeping the same porosity, are not sufficient to improve the redox tolerance unless also the porosity is increased. Moreover, the open porosity needs to be well distributed. Indeed, SEM observation showed that the introduction of PEMA-co-MMA

produced some large voids not evenly distributed into the anode. This result was confirmed when PMMA beads were introduced into anode slurry. The amount of pore former within the anodic slurry needs to be higher and must present mean size as finer as possible in order to obtain a well distributed porosity.

The addition of finer pore former such as graphite flakes within the anodic microstructure brought to an improvement towards redox tolerance. The cell tolerated six redox cycles before failure, even if already after the first cycle cracks formation is evidenced by the OCV drop. The benefit allowed by fine graphite addition is evident, due to more homogeneous distribution of fine porosity, though it is not enough to guarantee lifetime longer than six redox cycles.– From these observations, anodes with higher and finely distributed porosity can likely tolerate more redox cycles.

An alternative new interesting approach was considered during this research work, consisting in modifying the anode microstructure and YSZ backbone by addition of proper ceramic powders with high aspect ratio (*Alfa* powders). The use of *Alfa* powders in anode production allowed to increase the open porosity to 38% in the as sintered component, while the usual values are in the range of 25-30%. The porosity increase was not detrimental for the mechanical properties, keeping the average flexural strength in the order of 150 MPa.

Redox tolerant cells were therefore produced and tested. The cells did not show relevant cracks in the electrolyte up to 15 redox cycles. Thanks to the modifications realised within the anodic microstructure by this different powder, it was possible to create a structure with a higher and homogeneous porosity, which allowed Ni volume expansion upon re-oxidation with low stress generation.

OCV was quite constant during 15 redox cycles, while a consistent performance degradation upon redox cycles was observed, probably caused by changes into the anodic microstructure, such as growth and coarsening of the Ni particles, and occasional cracks into the anode network (observed by SEM analysis). Nevertheless, the OCV constant value over every cycle demonstrated that the electrolyte did not present significant cracks leading to cells failure, as it was confirmed by microstructural analysis. However, due to the

promising results obtained, such approach for high robust redox cells is under investigation for patent application, including materials and processing.

Even if sufficiently high for 15 redox cycles, the mechanical properties and stability of the anode was investigated with the aim to increase cell reliability. In order to achieve this goal, Al_2O_3 and CeO_2 were selected as dopants for their well documented properties as sintering aid and mixed electronic and ionic conductor respectively. NiO/YSZ powders with different amount of Al- or Ce-doping elements were tested in order to investigate how they modify the reduction and re-oxidation kinetics in comparison with the standard anodic powders.

Both dopant elements increase the reduction and oxidation rates with respect to the reference powder. The reduction rate increased monotonically with Al_2O_3 amount; on the other hand, only when high CeO_2 load is used (10%) the first reduction rate was sensibly affected. The second reduction and re-oxidation were faster than the first one for both dopants. The presence of coarser NiO particles generated in the first cycle and a consequent porosity modification can explain the generalized reaction rate increase.

Interesting information on redox behaviour of anode supported half cells doped with Al_2O_3 and CeO_2 were obtained by monitoring in-situ the deformation related to cyclic changes of the operative atmosphere. During oxidation, the highest curvature variations were observed for 1%Al-doped samples, resulting in a higher density of cracks that can be attributed to the limited porosity of the anode. Indeed, an increase in anode density leads to larger anode deformation upon NiO expansion during re-oxidation; this is responsible for high internal stresses and consequent cell failure. Samples produced using pure NiO and 5%Ce-doped NiO powder showed lower deformations due to their larger porosity, though this is not enough to avoid crack production within the electrolyte. It is interesting to observe that for the Ce-doped samples, the volumetric effect associated with Ni oxidation and successive reduction is counterbalanced by deformation correlated to $CeO_2 – Ce_2O_3$ transformation.

The obtained results lead to important understanding of the role of doping elements on the redox process; limitation of the anode expansion upon re-oxidation appears to be a first approach for increasing redox tolerance of anode supported cells.

A general aim to produce redox tolerant cells regards the reduction of supporting anode deformations. The results presented here suggest that this can be accomplished in two ways: (i) tailoring of the concentration of doping elements with an opposite volumetric behaviour to NiO (such as CeO_2) and (ii) increase of the anode porosity to tolerate Ni particles re-expansions. In any case the modification realized within anode microstructure must take in account the mechanical strength and performance.

APPENDIX

A. Normalized mass change and mass change rate diagrams for second reduction and re-oxidation for Al and Ce-doped powders.

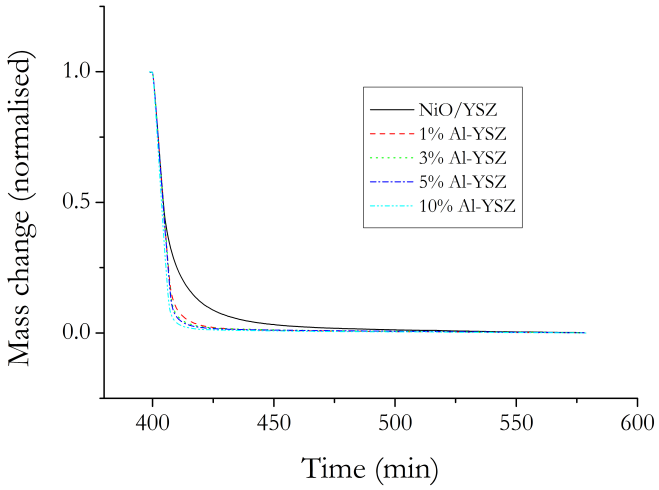

Figure A.1. Normalised mass change versus time upon second reduction for the Al-doped powders.

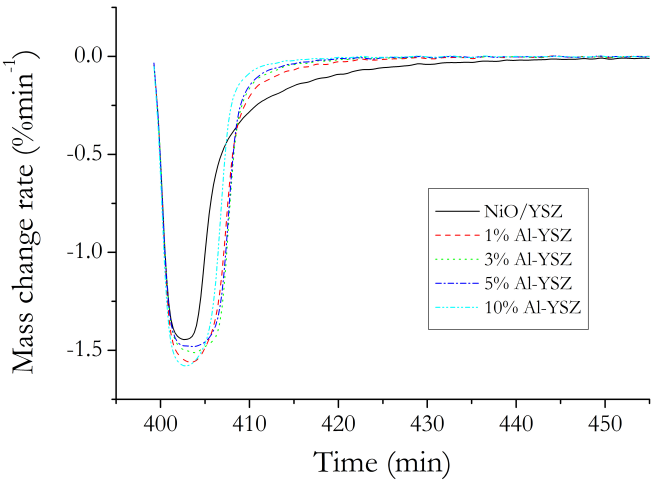

Figure A.2. Normalised mass change rate versus time upon second reduction for the Al-doped powders. The DTG graph is relative to the time interval where the mass change is more significant.

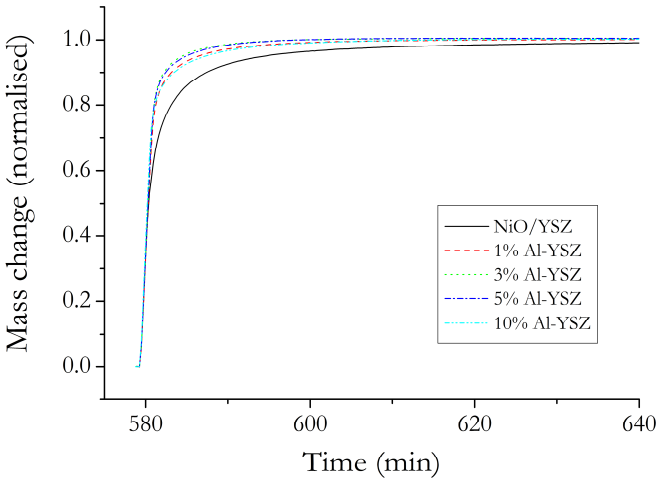

Figure A.3. Normalised mass change versus time upon second re-oxidation for the Al-doped powders.

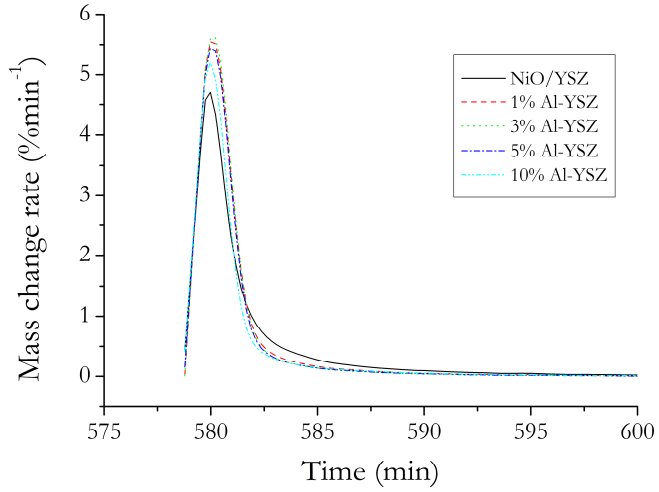

Figure A.4. Normalised mass change rate versus time upon second re-oxidation for the Al-doped powders. The DTG graph is relative to the time interval where the mass change is more significant.

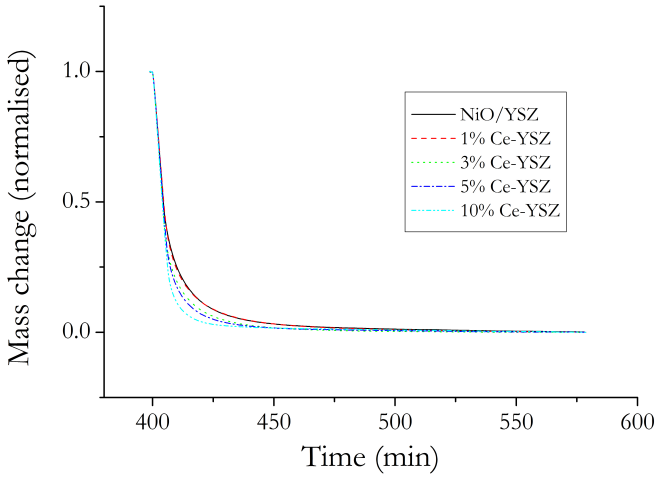

Figure A.5. Normalised mass change versus time upon second reduction for the Ce-doped powders.

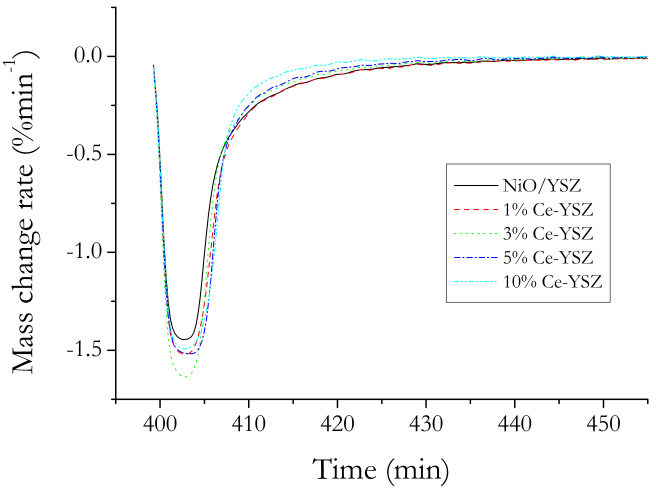

Figure A.6. Normalised mass change rate versus time upon second reduction for the Ce-doped powders. The DTG graph is relative to the time interval where the mass change is more significant.

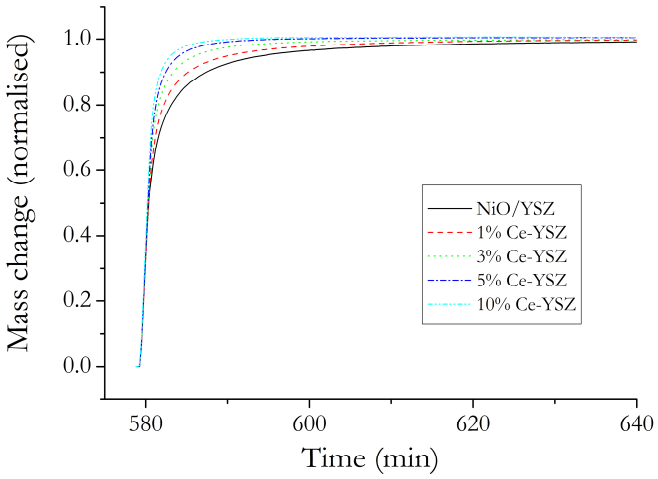

Figure A.7. Normalised mass change versus time upon second re-oxidant for the Ce-doped powders.

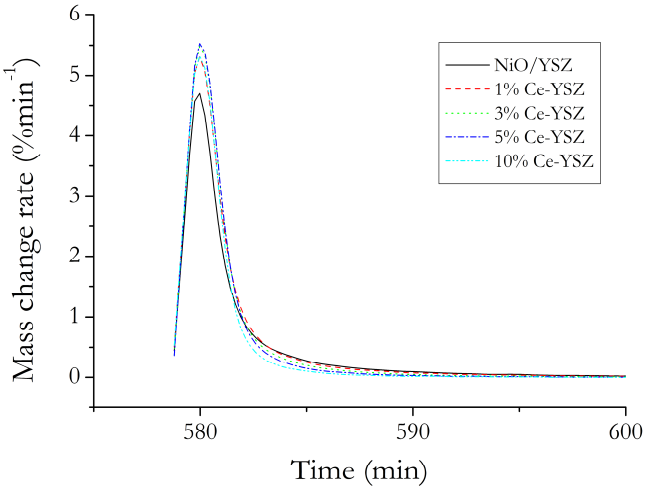

Figure A.8.. Normalised mass change rate versus time upon second re oxidation for the Ce-doped powders. The DTG graph is relative to the time interval where the mass change is more significant.

REFERENCES

1. **J. Larminie, A. Dicks**, Fuel Cell Systems Explained, second edition, *John Wiley & Sons Ltd.*, Chichester, UK (2003).
2. **S. Srinivasan,** Fuel Cells From Fundamentals to Applications, *Springer Science+Business Media*, New York, USA (2006)**.**
3. **A. B. Stambouli, E. Traversa** Solid oxide fuel cells (SOFCs): a review of an environmentally clean and efficient source of energy, *Renewable and Sustainable Energy Reviews* 6 (2002) 433–455.
4. **EG&G Technical Services, Inc.,** Fuel Cell Handbook (Seventh Edition), *U.S. Department of Energy*, Morgantown, West Virginia, USA (2004).
5. **K. Kuang, K. Easler** (Eds.), Fuel Cell Electronics Packaging, *Springer*, New York, USA (2007).
6. **B. C. H. Steele, A. Heinzel,** Materials for fuel-cell technologies, *Nature* 414 (2001) 345-352.
7. **R. O'Hayre, S. Cha, W. Colella, F. B. Prinz,** Fuel Cell Fundamentals, *John Wiley & Sons*, New York, USA (2006).
8. **R. Steinberger-Wilckens**, An introduction to Fuel Cells - Status and applications of fuel cell technology - SOFC types and designs - Competing technologies & the market place, Institute of Energy Research, IEF-PBZ Forschungszentrum Jülich, Large-SOFC Summer School, Chania (2008).
9. http://www1.eere.energy.gov/hydrogenandfuelcells/fuelcells/fc_types.html.
10. **S. C. Singhal, K. Kendal**, High Temperature Solid Oxide Fuel Cells: Fundamentals, Design and Applications, *Elsevier Ltd*, Oxford, UK (2003).
11. **M.C. Williams, J.P. Strakey, S. C. Singhal**, U.S. distributed generation fuel cell program, *Journal of Power Sources* 131 (2004) 79–85.
12. http://www.energy.siemens.com/hq/en/power-generation/fuel-cells/principle-behind-technology.htm.

13. **S.C. Singhal**, Science and Technology of Solid Oxide Fuel Cells, *MRS Bulletin* 25 (2000) 16-21.
14. **S. B. Lee, T. H. Lim, R. H. Song, D. R. Shin, S. K. Dong** Development of a 700 W anode-supported micro-tubular SOFC stack for APU applications, *International Journal of Hydrogen Energy* 33 (2008) 2330 – 2336.
15. **M. Cologna**, Advances in the Production of Planar and Micro-Tubular Solid Oxide Fuel Cells, *PhD thesis*, Università degli Studi di Trento, Trento (2009).
16. **Y. Funahashi, T. Shimamori, T. Suzuki, Y. Fujishiro, M. Awano**, New Fabrication Technique for Series-Connected Stack With Micro Tubular SOFCs, *Fuel Cells* 9 (2009) 711-716.
17. **N. M. Sammes, Y. Du, R. Bove,** Design and fabrication of a 100W anode supported micro-tubular SOFC stack, *Journal of Power Sources* 145 (2005) 428–434.
18. **J. H. Joo, G. M. Choi,** Thick-film electrolyte (thickness <20_m)-supported solid oxide fuel cells, *Journal of Power Sources* 180 (2008) 195–198.
19. **D. Prakash, T. Delahaye, O. Joubert, M. T. Caldes, Y. Piffard**, Intermediate temperature solid oxide fuel cell based on $BaIn_{0.3}Ti_{0.7}O_{2.85}$ electrolyte, *Journal of Power Sources* 167 (2007) 111–117.
20. **Y. B. Matus, L. C. De Jonghe, C. P. Jacobson, S. J. Visco,** Metal-supported solid oxide fuel cell membranes for rapid thermal cycling, *Solid State Ionics* 176 (2005) 443–449.
21. **H. Tu, U. Stimming**, Advances, aging mechanisms and lifetime in solid-oxide fuel cells, *Journal of Power Sources* 127 (2004) 284–293.
22. **A. V. Virkar**, A model for solid oxide fuel cell (SOFC) stack degradation, *Journal of Power Sources* 172 (2007) 713–724.
23. **K. C. Wincewicz, J. S. Cooper,** Taxonomies of SOFC material and manufacturing alternatives, *Journal of Power Sources* 140 (2005) 280–296.
24. **M. Backhaus-Ricoult**, SOFC - A playground for solid state chemistry, *Solid State Sciences* 10 (2008) 670-688.

25. **S. P. Jiang**, Development of lanthanum strontium manganite perovskite cathode materials of solid oxide fuel cells: a review, *Journal of Materials Science* 43 (2008) 6799–6833.
26. **S.C. Singhal**, Ceramic fuel cells for stationary and mobile applications, *The American Ceramic Society Bulletin* (2003) 9601-9610.
27. **V. A. C. Haanappel, J. Mertens, D. Rutenbeck, C. Tropartz, W. Herzhof, D. Sebold, F. Tietz**, Optimisation of processing and microstructural parameters of LSM cathodes to improve the electrochemical performance of anode-supported SOFCs, *Journal of Power Sources* 141 (2005) 216–226.
28. **H. Uchida, S. Arisaka, M. Watanabe**, High performance electrodes for medium-temperature solid oxide fuel cells: Activation of La(Sr)CoO_3 cathode with highly dispersed Pt metal electrocatalysts, *Solid State Ionics* 135 (2000) 347–351.
29. **Y. Tao, J. Shao, W. G. Wang, J. Wang**, Optimisation and Evaluation of $La_{0.6}Sr_{0.4}CoO_{3-\delta}$ Cathode for Intermediate Temperature Solid Oxide Fuel Cells, *Fuel Cells* 9 5 (2009) 679–683.
30. **E. Ivers-Tiffée, A. Weber, D. Herbistritt**, Materials and technologies for SOFC-components, *Journal of The European Ceramic Society* 21 (2001) 1085-1811.
31. **O. Yamamoto**, Solid oxide fuel cells: fundamental aspects and prospects, *Electrochimica Acta* 45 (2000) 2423–2435.
32. **S. C. Singhal**, Advances in solid oxide fuel cell technology, *Solid State Ionics* 135 (2000) 305 –313.
33. **J. P. P. Huijsmans**, Ceramics in solid oxide fuel cells, *Current Opinion in Solid State & Materials Science* 5 (2001) 317–323.
34. **J. W. Fergus,** Materials Challenges for Solid-Oxide Fuel Cells, *Hydrogen Economy Overview*, JOM, December, (2007).
35. **S. M. Haile**, Fuel cell materials and components, *Acta Materialia* 51 (2003) 5981–6000.

36. **S. Tekeli**, Influence of alumina addition on grain growth and room temperature mechanical properties of 8YSCZ/Al_2O_3 composites, *Composites Science and Technology* 65 (2005) 967-972.
37. **S. Tekeli**, The solid solubility limit of Al_2O_3 and its effect on densification and microstructural evolution in cubic-zirconia used as an electrolyte for solid oxide fuel cell, *Materials and Design* 28 (2007) 713–716.
38. **A.A.E. Hassan, N.H. Menzler, G. Blass, M.E. Ali, H.P. Buchkremer, D. Stöver**, Influence of alumina dopant on the properties of yttria-stabilized zirconia for SOFC applications, *Journal of Materials Science* 37 (2002) 3467-3475.
39. **R. Knibbe, J. Drennan, A. Dicks, J. Love**, Effect of alumina additions on the anode electrolyte interface in solid oxide fuel cells, *Journal of Power Sources* 179 (2008) 511-519.
40. **A. Atkinson, S. Barnett, R. J. Gorte, J. T. S. Irvine, A. J. McEvoy, M. B. Mogensen, S. Singhal, J. M. Vohs**, Advanced Anodes for High Temperature Fuel Cells, *Nature Materials* 3 (2004) 17-27.
41. **W.Z. Zhu, S.C. Deevi**, A review on the status of anode materials for solid oxide fuel cells, *Materials Science and Engineering*, A 362 (2003) 228-239.
42. **D. Simwonis, F. Tietz, D. Stöver**, Nickel coarsening in annealed Ni/8YSZ anode substrate for solid oxide fuel cells, *Solid State Ionics* 132 (2000) 241-251.
43. **A. Wood, M. Pastula, D. Waldbillig, D.G. Ivey**, Initial Testing of Solutions to Redox Problems with Anode-Supported SOFC, *Journal of The electrochemical Society* 153 (2006) A1929-A1934.
44. **H. Yokokawa, H. Tu, B. Iwanschitz, A. Mai**, Fundamental mechanisms limiting solid oxide fuel cell durability, *Journal of Power Sources* 182 (2008) 400–412.
45. **S. K. Pratihar, R.N. Basu, S. Mazumder, H.S. Maiti,** in: S.C. Singhal, M. Dokiya (Eds.), Proceedings of the Sixth International Symposium on Solid Oxide Fuel Cells (SOFC-VI) Honolulu Hawaii (17–22 October 1999) 513.

46. **A. V. Virkar, J.Chen, C. W. Tanner, J.W. Kim**, The role of electrode microstructure on activation and concentration polarizations in solid oxide fuel cells, Solid state ionic 131 (2000) 189-198.
47. **Y. LI, Z. LUO, C. YU, D. LUO, Z. XU, K CEN**, The impact of NiO on microstructure and electrical property of solid oxide fuel cell anode, *Journal of Zhejiang University SCIENCE* B 6 (2005) 1124-1129.
48. **D. Sarantaridis, A. Atkinson**, Redox Cycling of Ni-Based Solid Oxide Fuel Cell Anodes: A Review, *Fuel Cells* **7** (2007) 246-258.
49. **J. W. Fergus**, Oxide anode materials for solid oxide fuel cells, *Solid State Ionics* 177 (2006) 1529-1541.
50. **J. Karczewski, B. Riegel, M. Gazda, P. Jasinski, B. Kusz**, Electrical and structural properties of Nb-doped SrTiO3 ceramics, *Journal of. Electroceramics* (2009) DOI 10.1007/s10832-009-9578-7.
51. **S. Tao, J. T. S. Irvine**, Discovery and Characterization of Novel Oxide Anodes For Solid Oxide Fuel Cells, *The Chemical Record* 4 (2004) 83-95.
52. **J. J. Bentzen, J. V. T. Høgh, R. Barfod, A. Hagen,** Chromium Poisoning of LSM/YSZ and LSCF/CGO Composite Cathodes, *Fuel Cells* 9 (2009) 823–832.
53. **X. Chen, P.Y. Hou, C.P. Jacobson, S.J. Visco, L.C. De Jonghe**, Protective coating on stainless steel interconnect for SOFCs: oxidation kinetics and electrical properties, *Solid State Ionics* 176 (2005) 425-433.
54. **D. Montinaro,** Synthesis and Processing of Oxides Powders for Solid Oxide Fuel Cells (SOFC) Production, *PhD thesis*, Università degli Studi di Trento, Trento (2007).
55. **P. Batfalsky, V.A.C. Haanappel, J. Malzbender, N.H. Menzler,V. Shemet, I.C. Vinke, R.W. Steinbrech,** Chemical interaction between glass–ceramic sealants and interconnect steels in SOFC stacks, *Journal of Power Sources* 155 (2006) 128–137.
56. **V. A. C. Haanappel, V. Shemet, I. C. Vinke, S. M. Gross, TH. Koppitz, N. H. Menzler, M. Zahid, W. J. Quadakkers**, Evaluation of the suitability of various glass sealant—alloy combinations under SOFC stack conditions, *Journal of Materials Science* 40 (2005) 1583 – 1592.

57. **F. Smeacetto, M. Salvo, M. Ferraris, V. Casalegno, P. Asinari, A. Chrysanthou**, Characterization and performance of glass–ceramic sealant to join metallic interconnects to YSZ and anode-supported-electrolyte in planar SOFCs, *Journal of the European Ceramic Society* 28 (2008) 2521–2527.
58. **T. Klemensø, C. Chung, P. H. Larsen, and M. Mogensen,** The Mechanism Behind Redox Instability of Anodes in High-Temperature SOFCs, , *Journal of The Electrochemical Society* 152 (2005) A2186-A2192.
59. **D. Waldbillig, A. Wood, D. G. Ivey**, Electrochemical and microstructural characterization of the redox tolerance of solid oxide fuel cell anodes, *Journal of Power Sources* 145 (2005) 206-215.
60. **Y. Zhang, B. Liu, B. Tu, Y. Dong, M. Cheng**, Redox cycling of Ni-YSZ anode investigated by TPR technique, *Solid State Ionics* 176 (2005) 2193-2199.
61. **J. Kong, K. Sun, D. Zhou, N. Zhang, J. Qiao**, Electrochemical and microstructural characterization of cyclic redox behaviour of SOFC anodes, *Rare Metals* 25 (2006) 300-304.
62. **T. Klemensø and M. Mogensen**, Ni–YSZ Solid Oxide Fuel Cell anode behaviour upon redox cycling based on electrical characterization, , *Journal of The American Ceramic Society* 90 (2007) 3582–3588.
63. **D. Sarantaridis, R. A. Rudkin, A. Atkinson**, Oxidation failure modes of anode-supported solid oxide fuel cells, *Journal of Power Sources* 180 (2008) 704–710.
64. **S. Tao, J. T. S. Irvine**, Synthesis and Characterization of $(La_{0.75}Sr_{0.25})Cr_{0.5}Mn_{0.5}O_{3-\delta}$, a Redox-Stable, Efficient Perovskite Anode for SOFCs *Journal of The Electrochemical Society* 151 (2004) A252-A259.
65. **S. P. Jiang, S. H. Chan,** A review of anode materials development in solid oxide fuel cells, *Journal of Materials Science* 39 (2004) 4405 – 4439.
66. **D. Waldbillig, A. Wood, D. G. Ivey**, Enhancing the Redox Tolerance of Anode-Supported SOFC by Microstructural Modification, *Journal of The Electrochemical Society* 154 (2007) B133-B138.

67. **K. S. Lee, S. Lee, J. H. Yu, D. W. Seo, S. K. Woo**, Improvement of the stability of NiO-YSZ anode material for solid oxide fuel cell, *Journal of Solid State Electrochem*istry 11, (2007) 1295-1301.
68. **S. Tao, J. T.S. Irvine,** A redox-stable efficient anode for solid-oxide fuel cells, *Nature Materials* 2 (2003) 320-323.
69. **E. V. Tsipis, V. V. kharton,** Electrode materials and reaction mechanisms in solid oxide fuel cells: a brief review II. Electrochemical behaviour vs. materials science aspects, *Journal of Solid State Electrchemistry* 12 (2008) 1367-1391.
70. **Q. X. Fu, F. Tietz**, Ceramic-based anode materials for improved Redox cycling of Solid Oxide Fuel Cells, *Fuel Cells* 8 (2008) 283-293.
71. **C. Sun, U. Stimming**, Review Recent anode advances in solid oxide fuel cells, *Journal of Power Sources* 171 (2007) 247–260.
72. **F. Tietz, Q. Fu, V. A. C. Haanappel, A. Mai, N. H. Menzler, S. Uhlenbruck**, Materials Development for Advanced Planar Solid Oxide Fuel Cells, *International Journal of Applied Ceramic Technology* 4 (2007). 436–445.
73. **J. Malzbender, E. Wessel, R. W. Steinbrech,** Reduction and re-oxidation of anodes for solid oxide fuel cells, *Solid State Ionics* 176 (2005) 2201 – 2203.
74. **J. J. Haslam, A. Pham, B. W. Chung, J. F. DiCarlo, and R. S. Glass,** Effects of the Use of Pore Formers on Performance of an Anode Supported Solid Oxide Fuel Cell, *Journal of The American Ceramic Society* 88 (2005) 513–518.
75. **S. F.Corbin, J. Lee, X. Qiao,** Influence of Green Formulation and Pyrolyzable Particulates on the Porous Microstructure and Sintering Characteristics of Tape Cast Ceramics, *Journal of The American Ceramic Society* 84 (2001) 41-47.
76. **Y. Guzman**, Certain principles of formation of porous ceramic structures. Properties and applications (a review), *Glass and Ceramics* 60 Nos 9-10 (2003) 280-283.
77. **S. F. Corbin, X. Qiao**, Development of Solid Oxide Fuel Cell Anodes Using Metal Coated Pore Forming Agents, *Journal of The American Ceramic Society* 86 (2003) 401-406.

78. **M. Boaro, J. M. Vohs, R. J. Gorte**, Syntesis of Highly Porous Yttria-Stabilized Zirconia by Tape Casting Methods, *Journal of The American Ceramic Society* 86 (2003) 395-400.
79. **J. Morales, J. C.Vázquez, J. P. Martínez, D. López, J. T. S. Irvine, P. Núñez**, Microstructural optimisation of materials for SOFC applications using PMMA microspheres, *Journal of Materials Chemistry* 16 (2006) 540-542.
80. **R. M. C. Clemmer, S.F. Corbin**, Influence of porous composite microstructure on the processing and properties of solid oxide fuel cell anodes, *Solid State Ionics* 166 (2004) 251-259.
81. **A. Rainer, F. Basoli, S. Licoccia, and E. Traversa**, Foaming of Filled Polyurethanes for Fabrication of Porous Anode Supports for Intermediate Temperature- Solid Oxide Fuel Cells, *Journal of The American Ceramic Society* 89 (2006) 1795-1800.
82. **M. Radovic, E. Lara-Curzio**, Mechanical properties of tape cast nickel-based anode materials for solid oxide fuel cells before and after reduction in hydrogen, *Acta Materialia* 52 (2004) 5747–5756.
83. **M. Radovic and E. Lara-Curzio,** Elastic Properties of Nickel-Based Anodes for Solid Oxide Fuel Cells as a Function of the Fraction of Reduced NiO, *Journal of The American Ceramic Society* 87 (2004) 2242–2246.
84. **N. M. Tikekar, T. J. Armstrong and A. V. Virkar**, Reduction and Reoxidation Kinetic of Nickel-Based SOFC Anodes, *Journal of The Electrochemical Society* 153 (2006) A654-A663.
85. **D. Fouquet, A. C. Müller, A. Weber, E. Ivers- Tiffèe**, Kinetics of Oxidation and Reduction of Ni/YSZ Cermets, *Ionics*, 8 (2003) 103-108.
86. **M. Pihlatie, T. Ramos, A. Kaiser**, Testing and improving the redox stability of Ni-based solid oxide fuel cells, *Journal of Power Sources* 193 (2009) 322-330.
87. **S. Modena, S. Ceschini, A. Tomasi, D. Montinaro, V.M. Sglavo**, Reduction and Reoxidation Processes of NiO/YSZ Composite for Solid Oxide Fuel Cell Anodes, *Journal of Fuel Cell Science and Technology* 3 (2006) 487-491.

88. **D. Waldbillig, A. Wood, D. G. Ivey**, Thermal analysis of the cyclic reduction and oxidation behaviour of SOFC anodes, *Solid State Ionics* 176 (2005) 847-859.
89. **J. Qiao, K. Sun, N. Zhang, B. Sun, J. Kong, D. Zhou**, Ni/YSZ and Ni–CeO_2/YSZ anodes prepared by impregnation for solid oxide fuel cells, *Journal of Power Sources* 169 (2007) 253-258.
90. **M. Cologna, A.R. Contino, D. Montinaro, V.M. Sglavo**. Effect of Al and Ce doping on the deformation upon sintering in sequential tape cast layers for solid oxide fuel cells, *Journal of Power Sources* 193 (2009) 80–85.
91. **P. H. Larsen, C. Chung, M. Mogensen**, Redox-stable anode, WO Patent 2006079558.
92. **R. E. Mistler and E. R. Twiname**, Tape Casting – Theory and Practice, *The American Ceramic Society*, Westerville, OH, USA (2000).
93. **D. Hotza, P. Greil**, Review: aqueous tape casting of ceramic powders, *Materials Science and Engineering A*, 202 (1995) 206-217.
94. **B. Bitterlich, C. Lutz, A. Roosen**, Rheological characterization of water-based slurries for the tape casting process, *Ceramic International* 28 (2002) 675-683.
95. **James S. Reed**, "Principles of ceramics processing, second edition, (1995), *John Wiley & Sons*, NY USA (1995) 566-569.
96. **C.H. Hamann, A. Hamnet, W. Vielstich**, Elecrochemistry, second edition, *Wiley-VCH Verlag GmbH & Co*. Weinheim, Germany (2007).
97. **F. S. Baumann**, Oxygen reduction kinetics on mixed conducting SOFC model cathodes, *PhD thesis*, Max Planck Institut für Festkörperforschung, Stuttgart (2006).
98. **M. Cologna, M. Bertoldi, V. M. Sglavo**, Sintering and Deformation of Solid Oxide Fuel Cells Produced by Sequential Tape Casting, International *Journal of Applied Ceramic Technology* (2009) DOI:10.1111/j.1744-7402.2009.02390.x.
99. **D. C. Cranmer, D.W. Richerson,** Mechanical Testing Methodology for Ceramic Design and Reliability, *Marcel Dekker Inc* New York, USA (1998).
100. **ASTM C1499-08,** Standard Test Method for Monotonic Equibiaxial Flexural Strength of Advanced Ceramics at Ambient Temperature.

101. **O. A. Marina, C. Bagger, S. Primdahl, M. Mogensen**, A solid oxide fuel cell with a gadolinia-doped ceria anode: preparation and performance, *Solid State Ionics* 123 (1999) 199–208.

102. **J. Malzbender**, **E. Wessel, R.W. Steinbrech, L. Singheiser**, Reduction and re-oxidation of anodes for solid oxide fuel cells (SOFC), *Ceramic Engineering and Science Proceedings* 25 (2004) 387-392**.**

103. **A. Faes, A. Nakajo, A. Hessler-Wyser, D. Dubois, A. Brisse, S. Modena, J. Van Herle**, RedOx study of anode-supported solid oxide fuel cell, *Journal of Sources* 193 (2009) 55–64.

104. **P. Z. Cai, D. J. Green, G. L. Messing**, Constrained Densification of Alumina/Zirconia Hybrid Laminates, II: Viscoelastic Stress Computation, *Journal of The American Ceramic Society* 80 (1997) 1940–1948.

105. **V. V. Skorokhod**, Electrical Conductivity, Modulus of Elasticity and Viscosity Coefficient of Porous Bodies, *Powder Metallurgy* 12 (1963) 188–200.

106. **G. W. Scherer**, Sintering inhomogeneous glasses: Application to optical waveguides *Journal of Non-Crystalline Solids* 34 (1979) 239–256.

107. **S. Timoshenko**, Analysis of Bimetal Thermostats, *Journal of The Optical. Society of America* 11 (1925) 233–255.

108. **A. Atkinson, A. Selcuk**, Mechanical behaviour of ceramic oxygen ion-conducting membranes, *Solid State Ionics* 134 (2000) 59–66.

109. **J. Kondoh, H. Shiota, K. Kawachi, T. Nakatani**, Yttria concentration dependence of tensile strength in yttria-stabilized zirconia, *Journal of Alloys and Compounds* 365 (2004) 253–258.